CWP-163
December 1994

Depth Migration in Transversely Isotropic Media with Explicit Operators

Omar Uzcategui

— Doctoral Thesis —
Geophysics

Center for Wave Phenomena
Colorado School of Mines
Golden, Colorado 80401
303/273-3557

ABSTRACT

I present and analyze three approaches to calculating explicit two-dimensional (2D) depth-extrapolation filters for all propagation modes (P, SV, and SH) in transversely isotropic media with vertical and tilted axis of symmetry. These extrapolation filters are used to do 2D poststack depth migration, and also, just as for isotropic media, these 2D filters are used in the McClellan transformation to do poststack 3D depth migration. Furthermore, the same explicit filters can also be used to do depth-extrapolation of prestack data. The explicit filters are derived by generalizations of three different approaches: the modified Taylor series, least-squares, and minimax methods initially developed for isotropic media.

The examples here show that the least-squares and minimax methods produce filters with accurate extrapolation (measured in the ability to position steep reflectors) for a wider range of propagation angles than that obtained using the modified Taylor series method. However, for low propagation angles, the modified Taylor series method has smaller amplitude and phase errors than those produced by the least-squares and minimax methods. These results suggest that to get accurate amplitude estimation, modified Taylor series filters would be somewhat preferred in areas with low dips. In areas with larger dips, the least-squares and minimax methods would give a distinctly better delineation of the subsurface structures.

In all the implemented methods, the accuracy of the extrapolators depends on the elastic properties of the medium. Considering transversely isotropic media characterized by Thomsen's parameters ($V_{p0}, V_{s0}, \epsilon, \delta$, and γ), for the P mode, the accuracy of the operators increases with increasing values of δ, and decreases for increasing values of ϵ. In elliptically isotropic media ($\epsilon = \delta$), the accuracy of the extrapolators for the P mode is relatively insensitive to the degree of anisotropy. For the SV mode, the operators are basically determined by the parameter $\sigma \equiv (V_{p0}/V_{s0})^2(\epsilon - \delta)$, however, the accuracy in this propagation mode does not change much for typical values of σ found in sedimentary basins. Also, because there is no phase-velocity dependence on the phase angle θ from the axis of symmetry for elliptical media in the SV mode, filters for that mode have accuracy identical to that for isotropic media. Explicit filters for the SH mode can be obtained using the same computer programs used in the P mode, by making $V_{p0} = V_{s0}$, and $\epsilon = \delta = \gamma$. Therefore, the accuracy for the SH mode is identical to that obtained for the P mode for elliptical anisotropy.

Thus, the depth-extrapolation process as applied to depth migration in transversely isotropic media is determined mainly by certain Thomsen's parameters (ϵ and δ) for the P propagation mode, σ for the SV propagation mode, and γ for the SH mode. These result imply that for the P mode, we need only calculate tables of depth-extrapolation filters for a range of normalized frequencies ($f\Delta x/V_{p0}$) and for each pair of ϵ and δ values. It is sufficient to calculate these tables for only a representative constant value of the ratio V_{s0}/V_{p0}, e.g., $V_{s0}/V_{p0} = 0.5$. For the SV and SH mode, tables of depth-extrapolation

filters for only a range of normalized frequencies ($f\Delta x/V_{s0}$) and for each constant value of σ and γ, respectively, would be needed.

By first studying isotropic media, I show that the problem of inaccuracy at large dip is produced mainly by a singularity in the derivative of the imaginary-part of the downward-extrapolation operator. That singularity causes a relative slow convergence of the Fourier series in the imaginary-part filter. The same behavior arises in the downward-extrapolation operator for the P mode in transversely isotropic media, but this time the parameters ϵ and δ determine the derivative behavior, and therefore, the accuracy of the extrapolators. This theoretical analysis is confirmed by analyzing the accuracy of depth-extrapolation filters calculated using a least-squares method.

For the SV mode, I used the minimax method to calculate depth-extrapolation filters for some constant values of σ and found that, despite the wide variation in shapes of impulse responses with σ, the accuracy of the calculated extrapolators is similar for a wide range of σ, with maximum propagation angles of about 70 degrees in all cases. The least-squares method also has accuracy similar to that of the minimax method, but, unlike the minimax method it cannot handle triplications in the SV mode impulse response so well as the minimax method can. In contrast, due to the lack of accuracy for high propagation angles, modified Taylor series filters for the SV mode cannot reproduce these triplications at all.

On a field data set, I used modified Taylor series filters to obtain several depth migrated sections with different constants of anisotropy. The data set consisted mainly of low-dip reflectors and a main fault dipping at about 50 degrees. Using an anisotropic dip moveout (DMO) algorithm, estimates of the anisotropic parameter $\eta \equiv (\epsilon - \delta)/(1+2\delta)$ and a zero-offset section with variable velocity and variable parameter η were obtained by interpolating multiple constant-η, zero-offset panels. The vertical P-wave velocity field V_{p0} used in depth migration was obtained from the relation $V_{p0} = V_{NMO}(0)/\sqrt{1+2\delta}$, where $V_{NMO}(0)$ is the measured normal moveout velocity for horizontal reflectors.

To study the influence of using the anisotropic DMO and depth-migration algorithms, I calculated four different depth-migrated sections. The first section was calculated using isotropic filters over an isotropic DMO-plus-stack section. The second and third sections were calculated for a constant value of η over an anisotropic DMO-plus-stack section, but for different combinations of ϵ and δ. The last section was calculated using isotropic filters over the anisotropic DMO-plus-stack section. The results of the different depth-migrated sections show that because of the low estimated values of η, and for the range of dips (0-45 degrees) present in the area, to get a good imaging of the main fault it is sufficient to use the anisotropic DMO algorithm plus isotropic depth migration. The influence of anisotropy in the DMO process and correct location in depth of the reflectors in depth migration is appreciable. For these data, however, the influence of anisotropy is negligible in the lateral displacement produced by the depth-migration process itself.

The depth-migration program used on the field data set was implemented with some level of parallelism using the message-passing system PVM (Parallel Virtual Machine). In particular, prototype versions of 2D and 3D depth migration (using McClellan trans-

formations) were implemented using PVM. Preliminary results show that, through the parallelism, the total elapsed-time of the migration process can be reduced by a factor of 12 in a network of 25 IBM RS/6000 models 520 and 530 workstation. For the field data set, for example, 2D poststack depth-migrated sections consisting of 500 CMPs, 750 samples in time, and 600 steps of depth-extrapolation, were obtained in an average elapsed time of 9 minutes, as opposed to 110 minutes running in only one IBM RS/6000 model 530 workstation.

TABLE OF CONTENTS

ACKNOWLEDGMENTS

I am grateful to INTEVEP, Venezuela, for its financial support, and to Chevron Overseas Petroleum, Inc., for providing the field data for this project. Thanks also to Professors Ken Larner and Ilya Tsvankin for their helpful discussions and critical review. The author also wishes to thank Alejandro Murillo for his implementation in PVM of the migration programs, and Herman Jaramillo, John Anderson and Julie Liggett for helpful suggestions. This research was supported by the members of the Consortium Project on Seismic Inverse Methods for Complex Structures at the Center for Wave Phenomena, Colorado School of Mines. The research was also partially supported by the Department of Energy, Grant number DE-FG02-89ER14079 (this support does not constitute an endorsement by DOE of the views expressed in this paper).

Chapter 1

INTRODUCTION

Seismic exploration problems in complex areas are now being addressed using advanced seismic data processing techniques, for example, three-dimensional (3D) poststack and prestack depth migration. Traditionally, it has been considered that vertical and lateral velocity variations are the main problem in complex areas, but now explorationists are beginning to consider an additional problem, the presence of anisotropy in the subsurface layers. An ideal migration algorithm appropriate in complex areas must consider all these factors; it must handle vertical and lateral velocity variations, it must also handle 3D data, and it must allow the incorporation of anisotropy information that might be obtained from velocity analysis or well logging.

The assumption of elastic isotropy has been useful in seismic exploration for hydrocarbons; however, many sedimentary rocks are found from experiment to be anisotropic. Theoretical studies (Postma, 1955; Levin, 1979), velocity determinations in the laboratory (Thomsen, 1986), and field studies (Banik, 1984; White et al., 1983; Crampin et al., 1984; Ball, 1993) have shown that many sedimentary rocks are anisotropic. In particular, transversely isotropic (TI) media have been observed in several studies (Jones and Wang, 1981; Ball, 1993), and it is expected that media formed through rapid cyclical sedimentation patterns will be transversely isotropic or exhibit more complex anisotropy (Backus, 1962).

Clearly, since seismic imaging requires use of accurate migration velocity, anisotropy can play an important role in the positioning of geological boundaries on migrated images. Larner and Cohen (1993) and Alkhalifah and Larner (1994), have found that large position errors arise for steep reflectors when transverse isotropy is ignored in poststack migration. Also, isotropic migration algorithms applied to physical modeling data in TI media (Martin et al., 1992) produced mis-location of plane reflectors and a complete loss of steep structures.

Recognizing the importance of taking anisotropy into account, several authors have recently developed migration algorithms for anisotropic media. Uren et al. (1990) evaluated the performance of a two-dimensional (2D), frequency-wavenumber ($w - k$) depth migration algorithm in TI media. Sena and Toksöz (1993) developed a 2D Kirchhoff prestack depth migration algorithm using a Green's tensor representation for weakly TI media, and Alkhalifah (1995a) used a Gaussian beam algorithm for poststack migration in general 2D anisotropic media. Kitchenside (1993) developed both implicit and explicit schemes for frequency-space ($\omega - x$) downward continuation in 2D TI media. The explicit scheme involves the spatial inverse Fourier transform of the discrete downward-continuation operator for TI media in the $\omega - k$ domain; the resulting operator is then truncated and tapered to reduce the Gibbs phenomenon. However, as pointed out by

Nautiyal et al. (1993), either long operators or a strong tapering, with consequent loss of accuracy in the propagation region, are needed to get stable filters in this method.

Depth migration can be done using various algorithms; not a single migration algorithm can always be used with accuracy and computational cost advantages in all practical situations. Migration algorithms available today present different limitations in the handling of 3D and prestack seismic data, lateral velocity variations, dip angles, anisotropy, etc. Thus, implicit finite-difference migration (Claerbout, 1985) can handle lateral velocity variations but its extension to 3D seismic data is unpractical (Claerbout, 1985; Hale, 1991a). Migration via explicit methods for recursive depth extrapolation can handle arbitrary velocity variations (Holberg, 1988; Hale, 1992a) and can be easily extended to 3D seismic data by using McClellan transformations (Hale, 1991b); however, explicit methods have limited accuracy for steep reflectors. Gazdag's (1978) phase-shift method, has no dip-limitation problems, but this method is unable to handle lateral velocity variations efficiently (Hale, 1992a).

Other migration algorithms can address all the problems mentioned above, but their computational cost can be high. Reverse-time migration, for example, can be applied to all the situations that can be modeled (3D and prestack data, lateral velocity variations, any dip angle, anisotropy, etc.). Unfortunately, even in modern computers, the high computer cost and heavy demands on computer memory and input/output devices (Hale, 1992a) of reverse time migration can be prohibitive. Kirchhoff migration (Schneider, 1978) has been used recently in many practical situations because of its flexibility to adapt to almost any migration problem: 2D prestack and poststack (Ratcliff et al., 1992), and even 3D prestack depth migration (Cabrera et al., 1992). Hale (1992b) pointed out that the most difficult part in Kirchhoff migration algorithms is the accurate and efficient computation of traveltimes and amplitudes. Multi-valued traveltimes and amplitude functions (i.e., where more than one seismic wave can arrive at one surface location from the same subsurface point), and infinite amplitudes for ray caustics, tend to make Kirchhoff migration less robust in the presence of lateral velocity variations than are migration methods based on finite differences and explicit depth extrapolation (Hale, 1992b).

Gaussian beam migration (Costa et al., 1989; Hill, 1990) has recently arisen as a useful migration algorithm, with desirable features such as computational efficiency, robustness with respect to ray caustics, and straightforward extensions to prestack migration. Hale (1992b) analyzed the computer cost of Gaussian beam depth migration compared with the cost of depth migration via explicit depth extrapolation. He found that for typical stacked sections of 800 CMPs, 800 samples in time, and 800 steps of depth extrapolation, Gaussian beam migration is about 20 percent slower than explicit depth migration. Alkhalifah (1995a) obtained a Gaussian beam migration algorithm for poststack migration in general, 2D anisotropic media and found that this anisotropic algorithm was just 10 percent slower than its isotropic counterpart. On the other hand, the cost of explicit depth migration for anisotropic media is the same as the cost for isotropic media (Kitchenside, 1993); the convolution process is the same, and we have only to change the convolutional operators. Therefore, the computer cost of Alkhalifah's

(1995a) anisotropic Gaussian beam migration is about 30 percent higher than depth migration via explicit depth extrapolation.

Artley (1994) extended Gaussian beam migration to handle 3D data but his implementation was inefficient. I do not know of any reference that shows a practical implementation of Gaussian beam migration in 3D data. In addition, Gaussian beam migration may not lend itself to implemention on parallel or vector computers. These two possibilities (3D extension and parallel or vector implementations) are fully exploited in migration via explicit depth extrapolation (Hale, 1991b; Holberg, 1988). However, we must remember again, that current implementations of migration via explicit depth extrapolation have dip limitations and cannot handle turning waves; for complex structure with large dip, Kirchhoff and Gaussian beam migration would likely be preferred over migration via explicit depth extrapolation.

Thus, migration via explicit depth extrapolation (EDE) is attractive to apply in complex areas with lateral velocity variation and with reflectors that are not too steep because it has some efficiency and flexibility advantages over other migration processes. EDE is basically a convolutional process wherein each output is calculated independently, so the process can be easily implemented in parallel and vector computers. Moreover, EDE can also handle lateral and vertical velocity variations. As pointed out by Holberg (1988), just by changing the convolutional operators, heterogeneous media can be considered without increasing the computational cost and without loss of accuracy. Hale (1991b) also accomplished 3D depth migration by using McClellan transformations and the same 2D explicit operators that he used for 2D depth migration. Prestack migration can also be accomplished with EDE through combined use of explicit filters and ray tracing programs. EDE can be used to do downward continuation of receivers in common-midpoint and common-shot gathers (Kitchenside, 1992), and ray tracing programs or eikonal solvers can calculate efficiently the imaging condition for prestack migration.

Implementation of EDE in anisotropic media is the main subject of this thesis. Basically, I investigate the possibility of extending to TI media three approaches that have been used before to obtain EDE operators for isotropic media; the modified Taylor series (MTS) of Hale (1991a), the least-squares (LS) method of Holberg (1988), and the minimax method of Soubaras (1992). For TI media, EDE operators can be obtained by following the same steps as in the isotropic case, but with special considerations for the anisotropic nature of the phase velocity.

The MTS method used by Hale (1991a) for isotropic media can be adapted for transversely isotropic media with vertical axis of symmetry (VTI), but now taking into account that the horizontal wavenumber and the phase velocity are functions of the propagation angle. The basic idea is to find a filter in frequency-midpoint ($\omega - x$) space such that its spatial Fourier transform matches (in the propagation region) that of the downward-continuation operator for VTI media. To ensure attenuation of the evanescent energy, some degrees of freedom in the filter are used to force amplitude values to be less than unity in the evanescent region. It turns out that the MTS method produces filters that are always stable, so they can be applied for several thousand steps of downward continuation. Also, amplitude and phase errors of MTS filters are small for low propagation angles (i.e., less than 30 degrees). However, these filters lose accuracy quickly with increasing phase-propagation angle.

In an alternative approach, Holberg (1988) obtained explicit depth-extrapolation filters for isotropic media by minimizing the squared error of amplitude and phase of the filter in a given range of propagation angles with the vertical ($0 \leq |\theta| \leq \theta_{max}$). For VTI media I follow the same approach, but now take into account the theoretical expression for the downward-continuation operator for VTI media. Much as was done by Holberg, to get stability for angles greater than θ_{max} and in the evanescent region, I introduce a penalty function that grows for amplitude values of the filter greater than unity. I then use a conjugate-gradient algorithm to minimize the resulting function.

From the kinematic point of view, I find that the LS method generates filters with a wider range of accurate propagation angles than that of the MTS method, but the filters need to be designed carefully to avoid instability. Stable and accurate filters in the LS method are obtained using an iterative formulation wherein the LS problem is solved using several initial models for the filter coefficients until a sufficiently accurate and stable filter is found. This formulation increases the computational cost of the LS method. In relation to the MTS method, I also find that the amplitude and phase errors for LS filters and for low propagation angles are greater than the errors for MTS filters. However, the errors produced by LS filters remain relatively constant for propagation angles less than the maximum design angle θ_{max}, and these errors do not grow so quickly with increasing propagation angle as do the MTS errors.

Another approach to obtaining the explicit filters makes use of a minimax method. The minimax method has been applied before in the design of zero-phase bandpass filters (McClellan, et al. 1973) and in isotropic depth-migration applications (Soubaras, 1992). McClellan's 1973 computer code, originally designed to obtain bandpass filters, can be easily modified to allow the calculation of depth-extrapolation filters for TI media. The modification requires only (1) the match of the filter response with the theoretical downward-continuation operator for TI media, and (2) an inverse interpolation routine to find the phase-propagation angle for a given ratio of horizontal wavenumber to frequency (k/f). In the approach, the filters are calculated in such way that the maximum error in the propagation region between the ideal and the actual response of the filter is minimized. To obtain stability in the evanescent region, the amplitude response must be less than unity in that region. In the minimax method, I minimize the maximum error between the filter response and a decaying exponential function of wavenumber with amplitude values less than unity. Oppenheim and Schafer (1989) show that for the optimal solution to this type of problem, the resultant error function has maximum and minimum values of equal size, and the design problem becomes a problem in Chebyshev approximation over disjoint sets, solved using the Remez exchange algorithm (McClellan, et al. 1973). I find that the computational cost of the minimax method in obtaining the filters is far less than that of the LS method, although the accuracy of the resultant operators is comparable for the two methods.

In all these implemented methods, I find that the accuracy of the operators, measured in the ability to position dipping reflectors correctly, depends not only on which propagation mode is considered (P or SV), but also on the elastic properties of the medium. Here, I use Thomsen's (1986) parameters to characterize the TI media. In terms of the familiar elastic coefficients c_{ij} and density ρ, Thomsen's parameters are

$$\begin{aligned}
V_{p0} &\equiv \sqrt{c_{33}/\rho} \\
V_{s0} &\equiv \sqrt{c_{44}/\rho} \\
\delta &\equiv \frac{(c_{13}+c_{44})^2-(c_{33}-c_{44})^2}{2c_{33}(c_{33}-c_{44})} \\
\epsilon &\equiv \frac{c_{11}-c_{33}}{2c_{33}} \\
\gamma &\equiv \frac{c_{66}-c_{44}}{2c_{44}} \quad ,
\end{aligned} \tag{1.1}$$

where the subscript 3 refers to the symmetry-axis direction, and 1 to a normal to that direction. Thus, V_{p0} and V_{s0} are the P-wave velocity and S-wave velocity in the direction of the symmetry axis, respectively. The P- and SV-wave modes are described by the first four Thomsen parameters, while the SH-wave mode is described just by V_{s0} and γ.

I first examine which of the four Thomsen's parameters are needed to calculate explicit operators for the P and SV modes. Several tests on synthetic seismograms show that for the P propagation mode, we need only calculate explicit operators for each pair of ϵ and δ values. By comparing theoretical migration impulse responses for the SV mode, I show that, to a good approximation, we need only compute explicit operators for each σ value in the SV mode, where $\sigma \equiv (V_{p0}/V_{s0})^2(\epsilon-\delta)$ is a parameter introduced by Tsvankin and Thomsen (1994). For the SH mode, we only need compute operators for each γ value.

To study the accuracy problem in isotropic media, I calculate explicit filters for the real and imaginary parts of the downward extrapolation operator (DEO) (Uzcategui, 1994a), without amplitude constraints in the evanescent region. The idea is to use all the degrees of freedom in the filter to obtain accuracy. One result is that the imaginary-part filter produces most of the amplitude and phase error in the total filter. This behavior can be explained by using the convergence properties of Fourier series for the imaginary-part DEO. In TI media, I follow the same approach used in isotropic media, and study the properties of the imaginary-part DEO to explain the dependence of the accuracy of the filters on the values of ϵ and δ.

To address the 3D problem, I calculate 3D migration impulse responses in TI media with a vertical axis of symmetry using McClellan transformations. McClellan transformations is an efficient method to implement two-dimensional filters that have a particular form of symmetry, such as the circularly symmetric depth-extrapolation filters used in isotropic 3D depth migration (Hale, 1991b). In TI media with a vertical axis of symmetry, the symmetry of the 3D depth migration filter is not lost. The spatial wavenumbers in the inline and crossline directions (k_x and k_y, respectively) are symmetrically distributed about zero dip, i.e., $k_x(\theta) = k_x(-\theta)$, and the same relation holds for k_y. For TI media with a tilted axis of symmetry, this symmetry is lost, so a direct application of McClellan transformations is unfortunately not possible. The 3D impulse responses calculated with the McClellan transformations, agree with 3D theoretical impulse responses calculated using the group-velocity (Thomsen, 1986) and ray-angle equations for TI media.

By using modified Taylor series filters, I also obtain several depth-migration sections on a field data set from offshore Africa, for different values of Thomsen's parameters. The area consisted mainly of low-dipping reflectors and a main fault dipping about 45 degrees. Using an anisotropic dip-moveout (DMO) algorithm (Anderson and Tsvankin, 1994), I obtained estimates of the anisotropic parameter $\eta \equiv (\epsilon - \delta)/(1 + 2\delta)$ and generated a zero-offset section with variable velocity and variable parameter η by interpolating multiple constant-η zero-offset panels. Alkhalifah and Tsvankin (1994) showed that for seismic data processing in time, only the normal moveout velocity for horizontal reflectors $V_{NMO}(0)$ and η are needed to produce an accurate imaging. For depth migration, however, the correct positioning of the events in depth depends on V_{p0}, which is not readily estimated from surface seismic data.

Many different combinations of ϵ and δ can produce the same η value obtained from the anisotropic DMO analysis. For simplicity, and in order to study the influence of anisotropy on the DMO and depth-migration process, I calculate just four different depth-migrated sections. The first section was calculated using isotropic filters over an isotropic DMO-plus-stack section. The second and third sections were calculated for a constant value of η equal to the average value obtained in the DMO analysis (η=0.1) over an anisotropic DMO-plus-stack section, but for ϵ=0.1 and δ=0.0, and ϵ=0.0, δ=-0.083, respectively. The last section was calculated using isotropic filters over the anisotropic DMO-plus-stack section. The results show that because of the low estimated values of η, and for the range of dips (0-50 degrees) present in the area, to get a good imaging of the main fault it is sufficient to use the anisotropic DMO algorithm plus isotropic depth migration. The influence of anisotropy in the DMO process and correct location in depth of the reflectors in depth migration is appreciable, but the influence of anisotropy on lateral positions by depth migration is negligible.

MTS filters were chosen because reflector dips in the data set do not exceed about 45 degrees, and the values of the anisotropic constants obtained in the DMO processing are low (i.e., the average value of η is about 0.1). Therefore, these MTS filters can be used with confidence; they should produce better amplitude estimates than will the LS and minimax filters. Interval velocities derived from NMO velocity analysis were used to obtain the vertical velocity (V_{p0}) field for different choices of δ. Thomsen (1986) showed that vertical velocities in TI media differ from NMO velocities for horizontal reflectors (i.e., $V_{p0} = V_{NMO}/\sqrt{1+2\delta}$). Thus, for every different value of δ, the computed vertical velocity field V_{p0} changes, producing a relative displacement of the reflectors in depth with respect to the depths obtained in the isotropic depth migrated section. Because the η value was honored in both anisotropic depth migration calculations, the lateral position of the imaged reflectors was the same for migration with two different pair of ϵ and δ values.

The migration results on the real data agree with theoretical results obtained by Alkhalifah and Larner (1994) that show small lateral position errors for dip less than 50 degrees when transverse isotropy is ignored in poststack migration. On the other hand, on the field data set, the influence of anisotropy in the prestack processing (DMO) is crucial to get a good mapping of the fault plane. These results suggest that in many practical situations (i.e., relative low dips), anisotropy would influence mainly the prestack related seismic data processing; therefore, anisotropy corrections in the prestack phase would be fundamental to obtain a good imaging of dipping events, and a primary recommendation is that the methodology developed in this thesis be extended to prestack migration.

As an example of the possibility of implementing the EDE process in parallel and vector computers, prototype versions of 2D and 3D poststack depth migration were implemented using the message-passing system PVM (Parallel Virtual Machine). For poststack 3D depth migration, the computer time to calculate an impulse response on a data cube of 101x101 CMP locations in the inline and crossline directions, 101 samples in time, and for 101 steps of depth extrapolation, was reduced from about 165 minutes on a single IBM RS/6000 model 530 workstation to 25 minutes on a network of 25 similar machines (IBM/RS6000 models 530 and 520). For the field data set, 2D poststack depth-migrated sections consisting of 500 CMP locations, 750 samples in time, and 600 steps of depth-extrapolation, were obtained in average elapsed time of 9 minutes, as opposed to 110 minutes obtained running the same depth migration on only one of these IBM workstation. The total elapsed-time of the migration process was reduced by a factor of 12 for the 2D poststack process, but, for the 3D process, the reduction factor was only about 7. Although these results are preliminary and further analysis is needed to improve the 2D and 3D depth-migration implementations in PVM, the communication requirements in the 3D problem apparently increase the total cost.

Chapter 2

POSTSTACK MIGRATION IN TI MEDIA

2.1 Introduction

As in poststack migration for isotropic media, we assume that the exploding reflector model (Loewenthal, et. al., 1976) is also a convenient model for anisotropic media. The waves generated satisfy the scalar wave equation, but with a dispersion relation determined by the anisotropy with direction-dependent velocities. From the elastic wave equation for TI media, we obtain phase velocities and downward extrapolation operators (DEO) for the different propagation modes. These DEO are then used in one-way scalar migration equations, appropriate to motions for each of the propagation modes.

Much as is done in isotropic media, we assume that our zero-offset section has been processed to enhance only a single propagation mode (*P*, *SV*, or *SH*). Appropriate velocity analysis and moveout correction in anisotropic media (i.e, Alkalifah and Tsvankin, 1994) for each propagation mode must be applied in order that the stacking process enhance only the wanted propagation mode and attenuate the others. Converted waves, propagation modes not attenuated by the stacking process, multiple reflections, etc., will be considered as noise in the poststack section.

2.2 DEO in isotropic media

In a laterally invariant isotropic medium, 2D downward-extrapolation from depth z to depth $z + \Delta z$ can be done by using Gazdag's (1978) formula

$$P(\omega, k, z + \Delta z) = P(\omega, k, z) D(\omega, k), \tag{2.1}$$

where ω denotes angular frequency, k is the horizontal wavenumber, $P(\omega, k, z)$ is a plane-wave component of the seismic wavefield evaluated at depth z, and $D(\omega, k)$ is the 2D DEO in the frequency-wavenumber ($\omega - k$) domain, given by

$$D\left[\omega, k\right] = \exp\left\{ik_z \Delta z\right\} = \exp\left\{i \frac{\Delta z}{\Delta x}\left[\left(\frac{\omega \Delta x}{V_{ph}}\right)^2 - k_x^2\right]^{\frac{1}{2}}\right\}. \tag{2.2}$$

Here, k_z is the vertical wavenumber, Δz and Δx are the vertical and horizontal sampling intervals, V_{ph} is the phase velocity, and $k \equiv k_x(\theta)/\Delta x$ is the horizontal wavenumber. In depth extrapolation of CMP stacked data, we use the "exploding reflectors" concept and replace velocity V_{ph} with half-velocity $V_{ph}/2$ (Claerbout, 1985). For a general inhomogeneous medium with lateral velocity variation, downward-extrapolation can be carried out in the $(\omega - x)$ domain as a convolution in x. Taking the inverse spatial Fourier

c_{ijkl}	C_{IJ}
ij or kl	I or J
11	1
22	2
33	3
23 or 32	4
13 or 31	5
12 or 21	6

Table 2.1. Voigt recipe to change notation between the elastic tensor c_{ijkl} and the modulus matrix C_{IJ}

transform in equation (2.1) results in a change of the product in the $(\omega - k)$ domain into a convolution in the $(\omega - x)$ domain.

$$\tilde{P}(\omega, x, z + \Delta z) = \int \tilde{P}(\omega, x\prime, z)\tilde{D}(\omega, x - x\prime)dx\prime, \qquad (2.3)$$

where the tilde represents the inverse spatial Fourier transform, and the integral is evaluated over all space. $\tilde{D}(\omega, x)$ is also known as the spatial wavelet (Nautiyal et al., 1993). The spatial wavelet in equation (2.3) decays slowly for increasing magnitude of x; therefore, direct evaluation of this equation would be expensive. In practice, we approximate the spatial wavelet using a filter with a finite number of coefficients (see Chapter 3).

2.3 DEO in TI media

In order to obtain expressions for k_z in TI media, we start with the equations of motion. Wave propagation in TI media has been discussed broadly before (Thomsen, 1986; Kitchenside, 1991). Here, we follow an elementary approach to the derivation of the DEO in a TI medium. In the derivation of the DEO, we will assume a homogeneous TI medium. However, the actual extrapolation is performed in the $(\omega - x)$ domain, which allows lateral velocity variations [see equation (2.3)]. Therefore, we apply the DEO in a space-variant manner, i.e., each output point of the extrapolated data is computed using an operator based on one local value of the wavenumber $k(x, z, w) = w/c(x, z, w)$, the ratio of the currently treated frequency ω and the local propagation velocity.

The equations of motion in an elastic media, neglecting body forces, are (Aki and Richards, 1980)

$$\rho\ddot{u}_j = \frac{\partial}{\partial x_i}(c_{ijkl}\frac{\partial u_k}{\partial x_l}) \quad i, j, k, l = 1, 2, 3, \qquad (2.4)$$

where u_j is the j-th component of the displacement vector, $\ddot{u}_j$ is the j-th component of the acceleration, ρ is the density, and c_{ijkl} is the elastic modulus tensor. We seek plane harmonic solutions of the form

$$u_j = a_j \exp\left[i\omega(t - p_k x_k)\right] \qquad j = 1, 2, 3, \tag{2.5}$$

where a_j are the components of the polarization (i.e., particle-displacement) vector, and p_j are the components of the slowness vector. In homogeneous media, substitution of the displacements given by equation (2.5) in the equations of motion produces

$$\left[\frac{c_{ijkl}}{\rho} p_i p_l - \delta_{jk}\right] a_k = 0. \tag{2.6}$$

Making use of the Christoffel matrix $\Gamma_{jk} \equiv \frac{c_{ijkl}}{\rho} p_i p_l$, we can write equation (2.6) simply as

$$\left[\Gamma_{jk} - \delta_{jk}\right] a_k = 0. \tag{2.7}$$

The elastic tensor c_{ijkl} has the symmetry property

$$c_{ijkl} = c_{klij} = c_{lkji};$$

therefore, Γ_{jk} is symmetric and its eigenvalues are all real. Using these symmetry properties, the elastic tensor c_{ijkl} can be transformed with a change of indices into a symmetrical 6x6 matrix C_{IJ}, so that the 81 elastic coefficients in c_{ijkl} are reduced to 21 independent coefficients in the most general case of anisotropy. Following the Voigt recipe, the transformation from tensor to matrix notation can be made using Table 2.1. For a VTI medium, the elastic modulus matrix has five independent components, and is given by

$$C_{IJ} = \begin{bmatrix} C_{11} & (C_{11} - 2C_{66}) & C_{13} & & & \\ & C_{11} & C_{13} & & & \\ & & C_{33} & & & \\ & & & C_{44} & & \\ & & & & C_{44} & \\ & & & & & C_{66} \end{bmatrix},$$

where only the non-zero components above the diagonal are shown; the matrix is symmetrical.

Assuming that $\vec{a}$ is not identically zero in equation (2.7), the only nontrivial solutions to this equation are obtained from solving

$$\det\left[\Gamma_{jk} - \lambda\delta_{jk}\right] = 0. \tag{2.8}$$

Then, each of the three solutions to equation (2.6) is obtained by setting each of the three roots λ_i $(i = 1, 2, 3)$ of Γ_{jk} equal to unity. One eigenvalue corresponds to a quasi-compressional P wave, and the other two correspond to a quasi-shear wave, SV, and a pure shear wave SH (Daley and Hron, 1977). Using the elastic modulus matrix for a VTI medium in equation (2.8), and considering only propagation in the $(x - z)$ plane, we can take the y-component of the slowness vector p_2 as zero, and equation (2.8) will be given only in terms of the horizontal and vertical slownesses (p_1, p_3) in the $(x - z)$ plane

$$\det \begin{vmatrix} p_1^2C_{11} + p_3^2C_{44} - \lambda & 0 & p_1p_3(C_{13} + C_{44}) \\ 0 & p_1^2C_{66} + p_3^2C_{44} - \lambda & 0 \\ p_1p_3(C_{13} + C_{44}) & 0 & p_1^2C_{44} + p_3^2C_{33} - \lambda \end{vmatrix} = 0. \tag{2.9}$$

Solution of (2.9) yields

$$\begin{aligned} \lambda_1 &= \frac{1}{2}\{M + \sqrt{M^2 - L^2}\} \\ \lambda_2 &= \frac{1}{2}\{M - \sqrt{M^2 - L^2}\} \\ \lambda_3 &= p_1^2C_{66} + p_3^2C_{44}, \end{aligned} \tag{2.10}$$

where

$$\begin{aligned} M &= (C_{11} + C_{44})p_1^2 + (C_{33} + C_{44})p_3^2 \\ L &= (C_{11}p_1^2 + C_{44}p_3^2)(C_{44}p_1^2 + C_{33}p_3^2) - (C_{13} + C_{44})p_1^2p_3^2. \end{aligned}$$

$\lambda_1 = 1$ corresponds to a quasi-compressional P wave, $\lambda_2 = 1$ corresponds to a quasi-shear SV wave, and $\lambda_3 = 1$ corresponds to a shear SH wave. The phase velocities V_P, V_{SV}, and V_{SH}, can be obtained from each of equations (2.10) by using

$$p_1 = \frac{\sin\theta}{V_{ph}(\theta)}; \quad p_3 = \frac{\cos\theta}{V_{ph}(\theta)},$$

where $V_{ph}(\theta)$ is the phase velocity for the corresponding propagation mode, and θ is the angle between the propagation direction and the symmetry-axis direction. Instead of using the five elastic moduli C_{IJ} to describe wave propagation in TI media, Thomsen (1986) suggested a different notation involving only two elastic moduli (vertical P- and S-wave velocities) plus three dimensionless measures of anisotropy [ϵ, δ, and γ; see equation (1.1)]. As shown by Tsvankin (1994), Thomsen notation simplifies the description of wave propagation in TI media. In terms of Thomsen's parameters, the phase-velocity equations can be written as

$$V_{\mathrm{P}}^2(\theta) = V_{p0}^2\left[1 + \epsilon\sin^2(\theta) + D^*(\theta)\right] \tag{2.11}$$

$$V_{\mathrm{SV}}^2(\theta) = V_{s0}^2\left[1 + \frac{V_{p0}^2}{V_{s0}^2}\left(\epsilon\sin^2(\theta) - D^*(\theta)\right)\right] \tag{2.12}$$

$$V_{\mathrm{SH}}^2(\theta) = V_{s0}^2\left[1 + 2\gamma\sin^2(\theta)\right], \tag{2.13}$$

where $D^*(\theta)$ is given by

$$D^*(\theta) = \frac{1}{2}(1 - \frac{V_{s0}^2}{V_{p0}^2})\left\{\left[1 + \frac{4(2\delta - \epsilon)}{(1 - \frac{V_{s0}^2}{V_{p0}^2})}\sin^2(\theta)\cos^2(\theta) + \right.\right.$$

$$\left.\left. + \frac{4(1 - V_{s0}^2/V_{p0}^2 + \epsilon)\epsilon}{(1 - \frac{V_{s0}^2}{V_{p0}^2})^2}\sin^4(\theta)\right]^{1/2} - 1\right\}. \tag{2.14}$$

For an arbitrary orientation of the axis of symmetry with respect to the $z-$axis, it can be shown (Kitchenside, 1991) that the solutions for $V_{ph}(\theta)$ are given by

$$V_{\mathrm{P}}^2(\theta) = V_{p0}^2\left[1 + \epsilon\sin^2(\theta - \phi) + D^*(\theta - \phi)\right] \tag{2.15}$$

$$V_{\mathrm{SV}}^2(\theta) = V_{s0}^2\left[1 + \frac{V_{p0}^2}{V_{s0}^2}\left(\epsilon\sin^2(\theta - \phi) - D^*(\theta - \phi)\right)\right], \tag{2.16}$$

where ϕ is the angle between the axis of symmetry and the $z-$axis. Now, having the equations for the phase velocity, the DEO for each propagation mode can be simply written, just as in equation (2.2), as

$$D\left[\omega, k_x\right] = \exp\left\{i\frac{\Delta z}{\Delta x}\left[\left(\frac{\omega\Delta x}{V_{ph}(\theta)}\right)^2 - k_x^2\right]^{\frac{1}{2}}\right\}. \tag{2.17}$$

2.4 Phase and group velocity in TI media

As we have seen, the velocity of a plane wave in an anisotropic medium, changes with direction. This angular velocity dispersion results in the energy of an arbitrary seismic ray generally deviating from the normal to the surface of constant phase, so that, in general, the ray path is not normal to the surface of constant phase. In Figure 2.1, Huygens' principle in anisotropic media is applied to propagate seismic waves from a single dipping exploding reflector. If the traveltime from source S to receiver R is t seconds, then the group or ray velocity (velocity at which energy travels radially outward from the point source) V_g is given by $\hat{SR}/t$ in that direction. In contrast, the velocity of a single plane-wave along the direction $\vec{k}$ (locally perpendicular to the wavefront) is the phase velocity, and is given by $\hat{TR}/t$.

For plane waves, the phase velocity is also given from the dispersion relation $V_{ph}(\theta) = \omega/k$. If a wave vector $\vec{k}$ (along the plane $y = 0$) is given by $\vec{k} = k(\sin\theta\hat{x_1} + \cos\theta\hat{x_3})$ where $\hat{x_i}$ is the unit vector in the $ith-$direction, then, we can write the associated phase-velocity

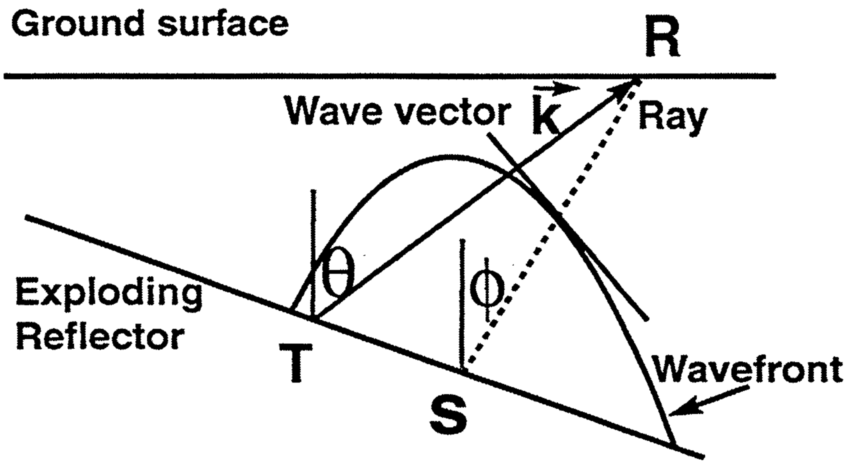

FIG. 2.1. Huygens' principle applied in anisotropic media to propagate waves from an exploding reflector.

vector as

$$\vec{V}_{ph}(\theta) = \frac{\omega}{k}(\sin\theta\hat{x_1} + \cos\theta\hat{x_3}). \tag{2.18}$$

The group velocity is given by (Berryman, 1979) $V_g(\phi) = \frac{\partial\omega}{\partial k}$, or in vector notation

$$\begin{aligned}\vec{V}_g(\phi) &= \frac{\partial\omega}{\partial k_1}\hat{x_1} + \frac{\partial w}{\partial k_3}\hat{x_3} \\ &= V_g(\sin\phi\hat{x_1} + \cos\phi\hat{x_3}),\end{aligned}$$

where the group angle ϕ is an implicit function of the phase angle θ given by (Berryman, 1979)

$$\begin{aligned}\tan\phi &= \frac{\partial\omega/\partial k_1}{\partial\omega/\partial k_3} \\ &= \left(\tan\theta + \frac{1}{V_{ph}}\frac{dV_{ph}}{d\theta}\right) / \left(1 - \frac{\tan\theta}{V_{ph}}\frac{dV_{ph}}{d\theta}\right).\end{aligned} \tag{2.19}$$

Berryman (1979) also obtained the relation between the group and phase velocity

$$V_g^2[(\phi(\theta))] = V_{ph}(\theta)^2 + \left(\frac{dV_{ph}}{d\theta}\right)^2. \tag{2.20}$$

As mentioned above, the group velocity is the velocity at which the energy travels in the

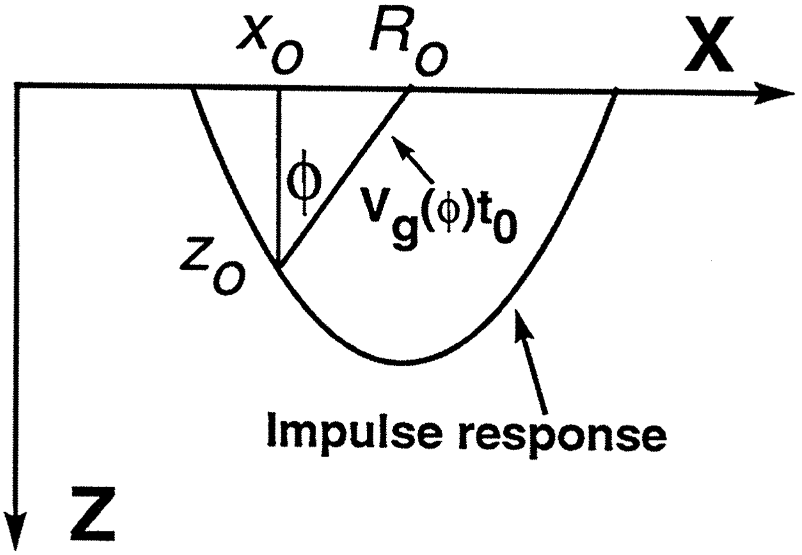

FIG. 2.2. Depth-migration impulse response in anisotropic media. x_0 and z_0 represent the spatial coordinates of any point on the migration impulse response.

subsurface; therefore, the group velocity is used directly in many geophysical applications, such as, for example, calculations of traveltime in ray-tracing programs, moveout corrections in anisotropic media, etc. However, other geophysical process (i.e., $\omega - k$ migration) work with individual plane-waves, so these process require the explicit use of the phase velocity.

2.5 Migration impulse response in TI media

After obtaining the equations for phase and group velocity, and for the group angle, one can readily evaluate theoretical migration impulse responses in TI media. These theoretical impulse responses will be used to evaluate the performance of different explicit migration algorithms.

The depth-migration impulse response is defined as the *locus* of points in the subsurface that have the same two-way zero-offset traveltime to a single receiver. From Figure 2.2 we see that the points x_0 and z_0 on the depth-migration impulse response curve are given by

$$\begin{aligned} x_0(\phi) &= R_0 - \frac{V_g(\phi)}{2} t_0 \sin\phi \\ z_0(\phi) &= \frac{V_g(\phi)}{2} t_0 \cos\phi \end{aligned} \tag{2.21}$$

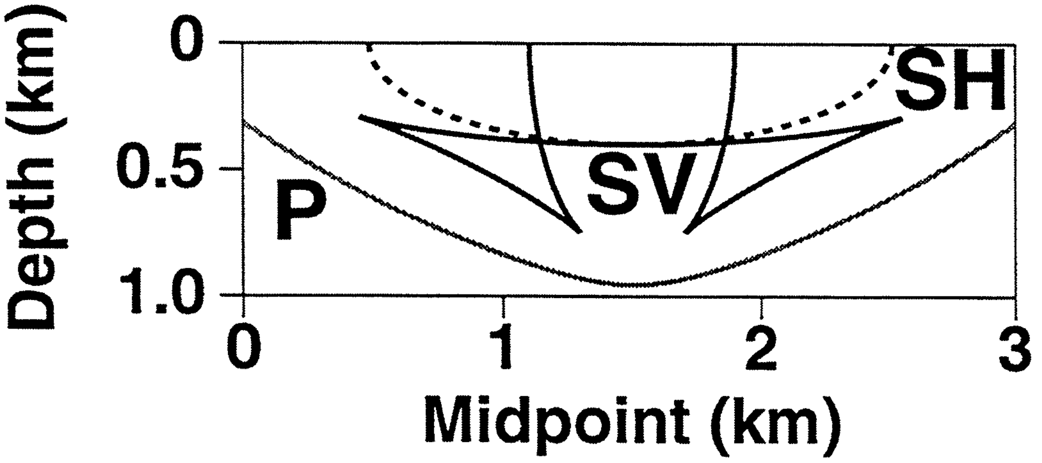

FIG. 2.3. Depth-migration impulse responses for the *P*, *SV*, and *SH* propagation modes in a homogeneous VTI medium (weathered gypsum).

where t_0 and R_0 are the time and x position of the impulse in the zero-offset section. In order to obtain the time-migration impulse response, we need only change the axis z to the axis of migrated time $\tau = 2z_0/V_g(\phi)$, so the time migration impulse response will be given by

$$\begin{aligned} x_0(\phi) &= R_0 - \frac{V_g(\phi)}{2} t_0 \sin\phi \\ \tau(\phi) &= t_0 \cos\phi. \end{aligned} \tag{2.22}$$

Figure 2.3 shows depth-migration impulse responses for the *P*, *SV*, and *SH* propagation modes in a homogeneous VTI medium, weathered gypsum (Thomsen, 1986). The impulse in the zero-offset section is located at a two-way time of 1.0 s, and Thomsen parameters for this medium are V_{p0} = 1.9 km/s, V_{s0} = 0.8 km/s, ϵ = 1.16, δ = -0.14, and $\gamma = 2.78$. Despite the fact that the medium is homogeneous, the *SV* response shows triplications due to the presence of extreme (maximum or minimum) values in the curve of group versus phase angle (Kitchenside, 1993). Recall that the phase angle is the slope of a tangent to the wavefront (impulse response in Figure 2.3) and the ray angle is defined by the direction from the origin (R_0 in Figure 2.2) to the wavefront. When we move along the *SV* impulse response from the point at which the phase angle is zero, the phase angle increases monotonically, whereas the ray angle increases, decreases, and then increases again. Also, as expected from equation (2.13), the impulse response in Figure 2.3 is elliptical for the *SH* mode. For comparison, for an isotropic medium, all the impulse responses would be circular.

Figure 2.4 shows time-migration impulse responses for the same medium as in Figure

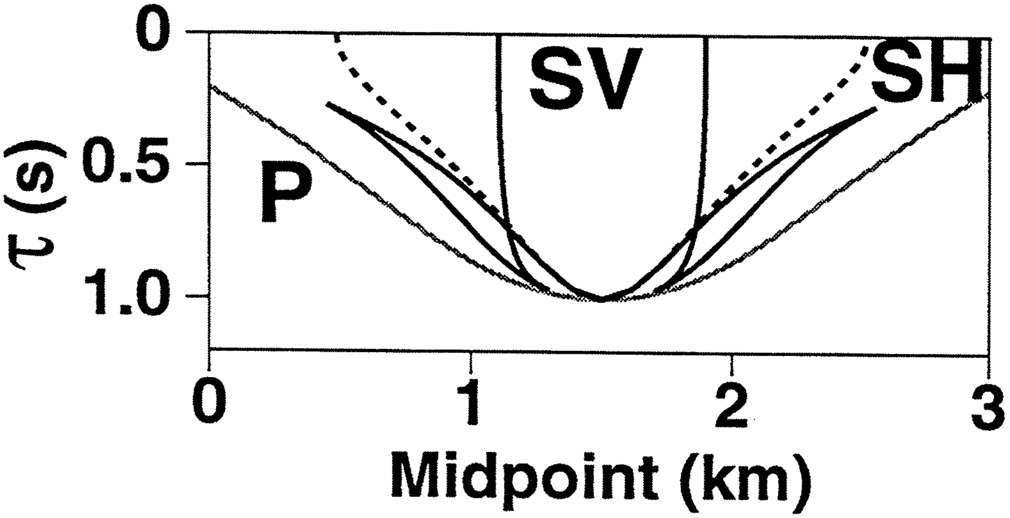

FIG. 2.4. Time-migration impulse responses for the same medium as in Figure 2.3

2.3. For vertical propagation ($\phi = 0$), the three impulse responses have the same migrated time value (that is, time migration does not alter the time of horizontal reflections). The migrated-time axis τ in Figure 2.4 is a stretched version of the depth axis z in Figure 2.3, with a variable stretching factor given by the inverse of the group velocity $1/V_g(\phi)$. From Figure 2.3, we see that for the P and SH modes, $V_g(\phi)$ is greater for horizontal than for vertical propagation (wavefronts travel larger distances along the horizontal than along the vertical direction). In the $(x-\tau)$ domain (Figure 2.4), vertical propagation corresponds to higher values of τ; therefore, the stretching factor $1/V_g(\phi)$ increases with migrated time τ, producing angle-dependent distortions with respect to the wavefronts in Figure 2.3. If the homogeneous medium in Figure 2.4 were isotropic, the time-migration impulse responses would be ellipses, just stretched versions of the circular depth-migration impulse responses, with stretch factors equal to the inverse of the isotropic velocity.

2.6 Phase-shift (Gazdag) migration in TI media

In Chapter 3 we will evaluate the performance of explicit depth-extrapolation filters by calculating migration impulse responses via explicit filtering in homogeneous media. Using equations (2.21) for the group velocity and ray angle, we can evaluate the exact kinematics of the impulse responses in TI media to compare with the kinematics obtained via explicit filtering; however, we do not have an analytic tool to evaluate the amplitude distribution along these impulse responses. In homogeneous media, downward extrapolation can be done exactly using the Gazdag's (1978) phase-shift operator; therefore, migration impulse responses in TI media obtained using Gazdag's method provide results against which we can compare the amplitude response of migration via explicit filtering.

In addition, it is also important to analyze how the amplitudes obtained by the Gazdag and explicit depth-extrapolation methods are related to the anisotropy in the medium. Knowing this relation, we can correct amplitudes obtained using these two methods for possible distortions due to anisotropy.

Phase-shift migration (Gazdag, 1978) in TI media can be done following a similar approach to that used in isotropic media, wherein downward extrapolation of the wavefield is obtained by multiplying the Fourier transform of the recorded seismic wavefield $P(\omega, k_x, z = 0)$ with $\exp\{ik_z\Delta z\}$, the DEO in isotropic media, where k_z is again the vertical wavenumber. As is done in isotropic media, if only vertical variations in velocity and in the anisotropic constants are allowed, downward extrapolation of the seismic wavefield in TI media is obtained by multiplying $P(\omega, k_x, z = 0)$ with $\exp\{ik_z\Delta z\}$, where k_z is now governed by the particular propagation mode in TI media. Due to the angular velocity dispersion in TI media, the phase propagation angle for each plane-wave component in the phase-shift method needs to be calculated from the relation $k/\omega = \sin\theta/V_{ph}(\theta)$. Following the notation of Claerbout (1985) for isotropic media, a Gazdag depth-migration scheme in TI media can be readily defined as

```
$P(\omega, k_x) = FT\,(p(t,x))$;
$for(z = \Delta z, 2\Delta z, \ldots, z_{max})\{$
    $for\ all\ k_x\{$
    $Image(k_x, z) = 0$;
        $for\ all\ \omega\{$
        $locate(k/\omega, \theta, z)$;
        $C = \exp\left(-i\Delta z \frac{\omega}{V_{ph}(\theta,z)}\sqrt{1 - \frac{V_{ph}^2(\theta,z)k_x^2}{\omega^2}}\right)$;
        $P(\omega, k_x) = P(\omega, k_x) * C$;
        $Image(k_x, z) = Image(k_x, z) + P(\omega, k_x)$;
        $\}$
    $\}$
$image(x, z) = FT\,(Image(k_x, z))$
$\}$,
```

where FT denotes Fourier transform, $p(t, x)$ is the recorded wavefield at the surface, $image(x, z)$ is the final depth-migrated section, and *locate* is an inverse interpolation function that calculates the phase propagation angle θ from a pre-computed table of ratios $k/\omega = \sin\theta/V_{ph}(\theta)$.

Figure 2.5 shows three depth-migration impulse responses for the P propagation mode in weathered gypsum, based on the Gazdag method. In the test, spatial sampling intervals $\Delta x = \Delta z = 10$ m, and the time sampling interval $\Delta t = 10$ ms. The trajectory of the theoretical impulse response for the middle impulse is shown in the figure as a thin dotted line. Due to the high value of ϵ for this material (ϵ=1.16), the migration impulse response is broader than the familiar migration impulse response for isotropic media. On the middle impulse response (dotted line), for example, the distance from the origin (midpoint=1.5 km; z=0 km) to the impulse response for horizontal propagation is about 1.0 km, whereas, the distance for vertical propagation is only 0.5 km. Note also that the Gazdag method has no dip limitations; however, amplitudes values decrease with increasing propagation angle. We discuss this angle-dependent amplitude behavior next.

2.7 Angular amplitude distribution in the Gazdag method

Kinematically, migration impulse responses in homogeneous media are equivalent to wavefronts radiating from a point source, and these impulse responses correspond to plots of $V_g(\phi)$ in polar coordinates [equation (2.21)]. If the medium were isotropic, the phase shift applied in the Gazdag method ($\omega - k$ domain) would automatically introduce the obliquity-factor amplitude term ($\cos\psi$) in the final migrated section ($x - z$ domain, Claerbout, 1985). This obliquity-factor amplitude term corresponds to the radiation pattern for P-waves produced by a point vertical force in a homogeneous isotropic medium. In TI media, the amplitude distribution is governed not only by the obliquity factor, but also by the anisotropic constants in the medium (Tsvankin, 1994).

Radiation patterns in anisotropic media have been derived before using different approaches. Tsvankin and Chesnokov (1990) presented an analytical solution derived in the stationary-phase approximation. Ben Menahem et al. (1991) and Gajewski (1993) obtained expressions for radiation patterns in anisotropic media using asymptotic ray-theory. All these solutions require numerical evaluation and do not provide easy analytic insight into the problem. Tsvankin (1994) presented a concise weak-anisotropy approximation for radiation patterns in TI media relating distortions of point-source radiation to Thomsen parameters. He found that the weak-anisotropy approximation is accurate (for small and moderate values of ϵ, δ, and γ) and provides a convenient tool for qualitative amplitude estimates for a wide range of transversely isotropic models. Here, we compare amplitudes on migration impulse responses obtained using Gazdag's method with the amplitudes obtained using Tsvankin's (1994) weak-anisotropy formula.

Figure 2.6 shows a depth-migration impulse response for the P mode in an isotropic medium using the Gazdag method. The same spatial and time sampling intervals used in Figure 2.5 will be used in all the following examples. As predicted, amplitude values decrease with increasing group angle. Figure 2.7 shows the maximum amplitude of the P-wave in each trace as a function of group angle for the impulse response of Figure 2.6. The solid curve was obtained by automatic picking of the maximum amplitude value of each trace in the depth migration impulse response of Figure 2.6 and normalizing by the vertical-incidence amplitude. The dotted curve in Figure 2.7 is the standard obliquity factor in isotropic media ($\cos\psi$). Note that the Gazdag migration amplitudes follow almost exactly the standard decay given by the obliquity factor, up to the maximum group angle shown, 75 degrees. For high propagation angles (close to 90 degrees), the amplitudes

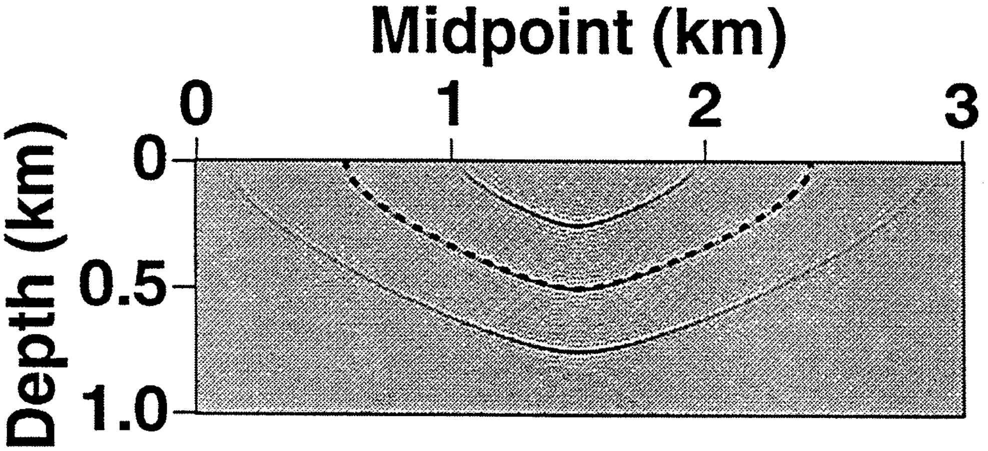

FIG. 2.5. Depth-migration impulse responses via the Gazdag method for the P propagation mode in the weathered gypsum.

in the Gazdag impulse response are weak because $\cos\psi \to 0$, and these amplitudes can be comparable to the numerical noise generated by the discrete implementation of the algorithm (Claerbout, 1985).

For TI media, Tsvankin (1994) obtained the P mode far-field radiation pattern for a point force and for weak transverse isotropy ($\epsilon \ll 1$, $\delta \ll 1$, and $\gamma \ll 1$) as

$$U_P(R,\theta) = \frac{F_u}{4\pi\rho V_{p0}^2 R}\frac{[1-2(\epsilon-\delta)\sin^2 2\theta + \delta\sin^2\theta]}{1+2\delta}, \tag{2.23}$$

where U_P is the absolute value of the P displacement, θ is the phase angle, $R \equiv \sqrt{z^2+r^2}$ (z is the receiver depth, r is the horizontal source-receiver offset), ρ is the density, and the source term F_u is the projection of the force on the displacement (polarization) vector. Tsvankin (1994) also pointed out that the polarization of the P-wave excited by a point force in a homogeneous anisotropic medium is usually close to the isotropic direction; therefore, the source directivity factor F_u has almost the same influence on the P-wave radiation pattern as it has in isotropic media. For isotropic media ($\epsilon = \delta = 0$) and for constant R, equation (2.23) reduces to the standard obliquity factor (e.g., $\cos\phi$) contained in the term F_u. To explain the behavior of the term F_u, Tsvankin (1994) also found expressions for the polarization angle as a function of the anisotropic constants in the weak-anisotropy approximation

$$\tan\phi = \tan\theta\left\{1 + B\left[2\delta + 4(\epsilon-\delta)\sin^2\theta\right]\right\}, \tag{2.24}$$

$$B = \frac{1}{2(1-V_{s0}^2/V_{s0}^2)},$$

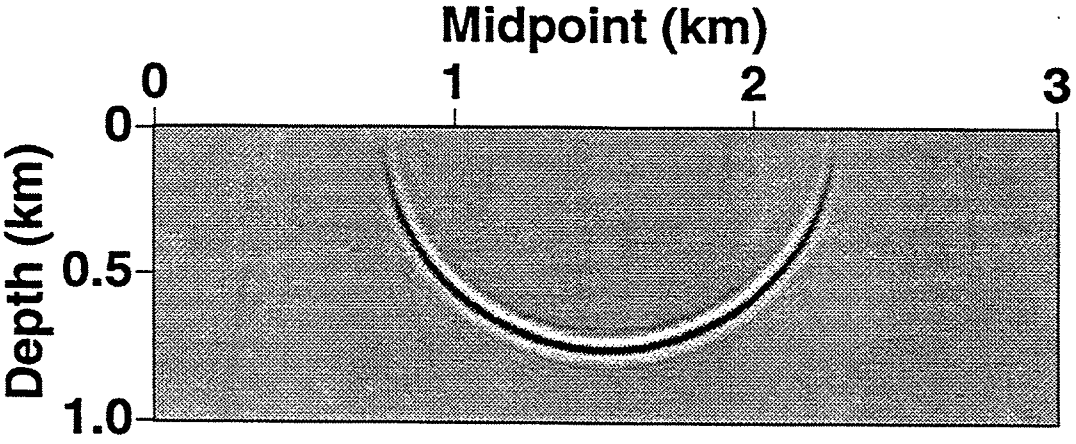

FIG. 2.6. Depth-migration impulse response via the Gazdag method for the P propagation mode in isotropic media.

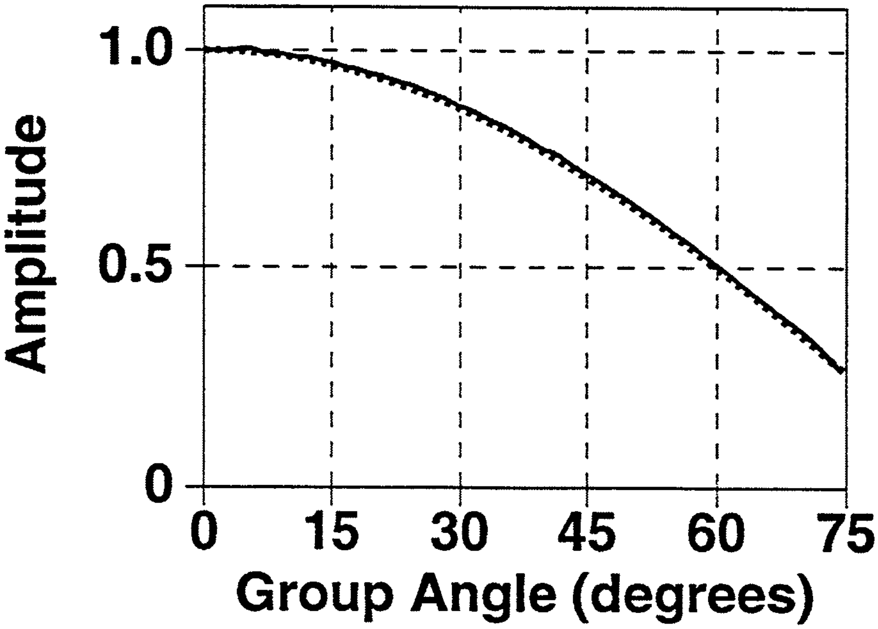

FIG. 2.7. Amplitude as a function of group angle for the migrated section of Figure 2.6. Solid line: maximum wavelet amplitude value in each trace. Dotted line: obliquity factor ($\cos\psi$) for isotropic media.

where ϕ is the polarization angle measured from the symmetry axis.

Figure 2.8 shows a depth-migration impulse response for the P mode in a TI medium with Thomsen parameters given by $V_{p0} = 2.0$ km/s, $V_{s0} = 1.0$ km/s, $\epsilon = 0.0$, and $\delta = 0.3$. The amplitude distribution for this medium differs considerably from that of Figures 2.5 and 2.6. In Figure 2.8, the amplitudes initially increase with propagation angle up to a maximum value, and then decrease to zero for horizontal propagation. Figure 2.9 shows this behavior quantitatively. The solid curve again shows values obtained from the maximum amplitudes picked on the traces in Figure 2.8; the dashed line represents the standard obliquity factor ($\cos\psi$) for isotropic media; and the dotted line represents the amplitudes predicted by equation (2.23), with F_u corresponding to the directivity factor for a point vertical force [$\cos\phi$, and ϕ given by equation (2.24)]. Within the numerical error, the amplitudes obtained by the Gazdag method in Figure 2.9 follow the anisotropic amplitudes predicted by equation (2.23); and both amplitudes differ substantially from the standard obliquity factor in isotropic media. To further compare Gazdag amplitudes with those of equation (2.23), we calculate a depth-migration impulse response for a medium which is the same as in Figure 2.8 except that now $\delta = -0.3$ (Figure 2.10). As pointed out by Tsvankin (1994), for low propagation angles (close to vertical propagation) equation (2.23) predicts focusing of the energy for $\delta < 0$, and defocusing for $\delta > 0$. Figure 2.11 shows again that the anisotropic Gazdag amplitudes follow pretty well the theoretical amplitudes based on the weak-anisotropy assumption; these amplitudes decay much faster than the standard obliquity factor.

For elliptical anisotropy ($\epsilon = \delta$), Tsvankin (1994) showed that the stationary-phase solution reduces to a simple function of the group angle ψ without application of the weak-anisotropy approximation

$$U_P(R,\psi) = \frac{F_u}{4\pi\rho V_{p0}^2 R}\frac{1}{\sqrt{(1+2\delta)(1+2\delta\cos^2\psi)}}. \tag{2.25}$$

In addition, Tsvankin(1994) also finds an expression for the polarization angle without using the weak-anisotropy approximation

$$\tan\phi = \tan\theta\sqrt{1+2B\delta}. \tag{2.26}$$

For the *SH*-mode, Tsvankin (1994) obtained a similar expression to that for the P elliptical mode

$$U_{SH}(R,\psi) = \frac{F_2}{4\pi\rho V_{s0}^2 R}\frac{1}{\sqrt{(1+2\gamma)(1+2\gamma\cos^2\psi)}}, \tag{2.27}$$

where F_2 is now the force component perpendicular to the incidence plane. The *SH*-wave radiation pattern is basically identical to the *P*-wave pattern for elliptical media (replace V_{s0} and γ by V_{s0} and δ respectively); however, for the *SH*-wave radiation pattern the source term F_2 is constant because the polarization direction does not change with the incidence angle.

The DEO for TI media in Gazdag's migration thus does not distinguish between ellip-

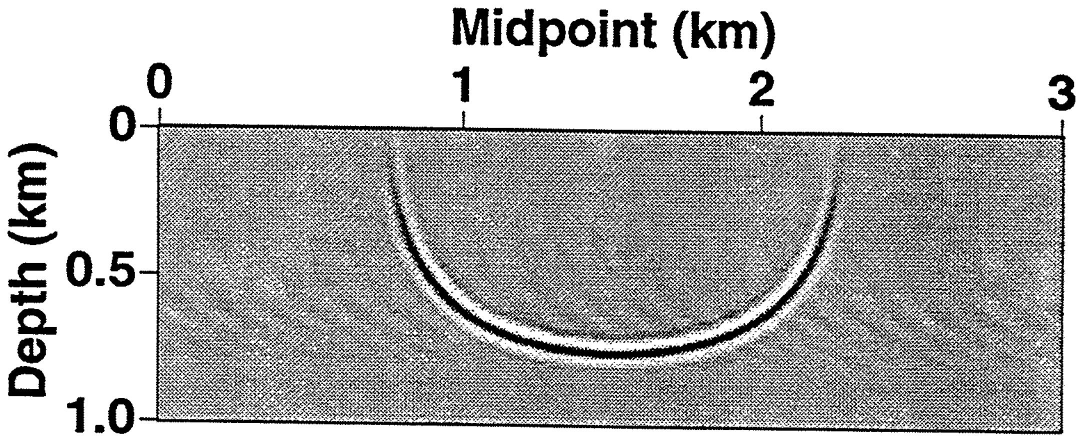

FIG. 2.8. Depth-migration impulse response for the P mode in a VTI medium with Thomsen's parameters V_{p0}= 2.0 km/s, V_{s0}= 1.0 km/s, $\epsilon = 0.0$, and δ= 0.3.

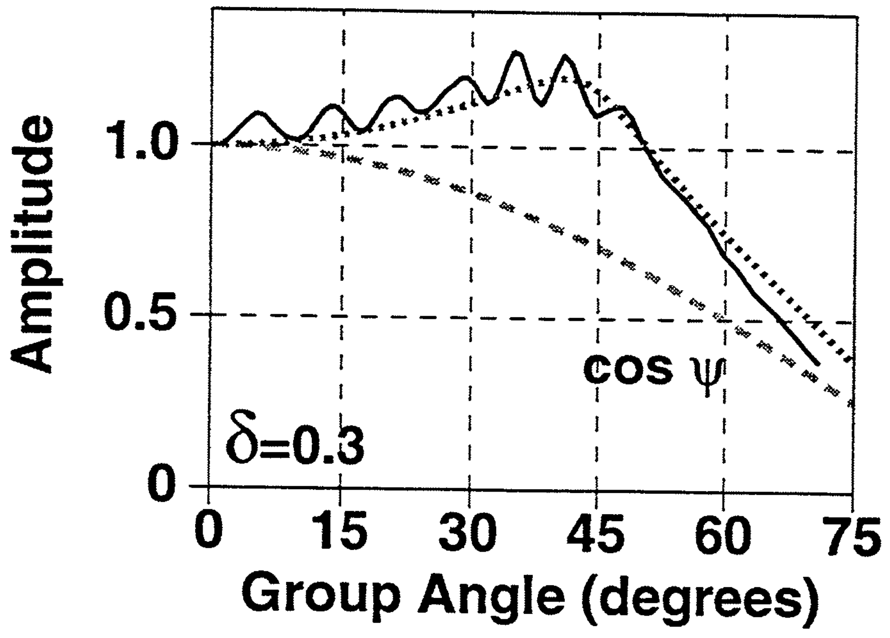

FIG. 2.9. Relative amplitude obtained from the depth-migrated section of Figure 2.8 (solid line). The standard obliquity factor ($\cos\psi$) for isotropic media is shown as the dashed line, the dotted line shows the amplitudes predicted by equation (2.23).

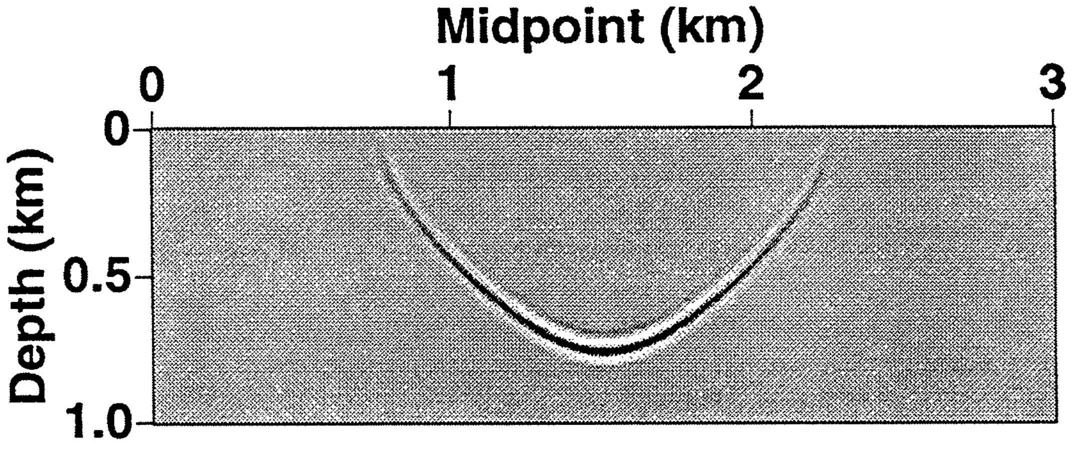

FIG. 2.10. Depth-migration impulse response for a VTI medium with the same Thomsen's parameters as in Figure 2.8, but with δ= -0.3. Note the different shape and, in particular, amplitude distribution in relation to Figure 2.8.

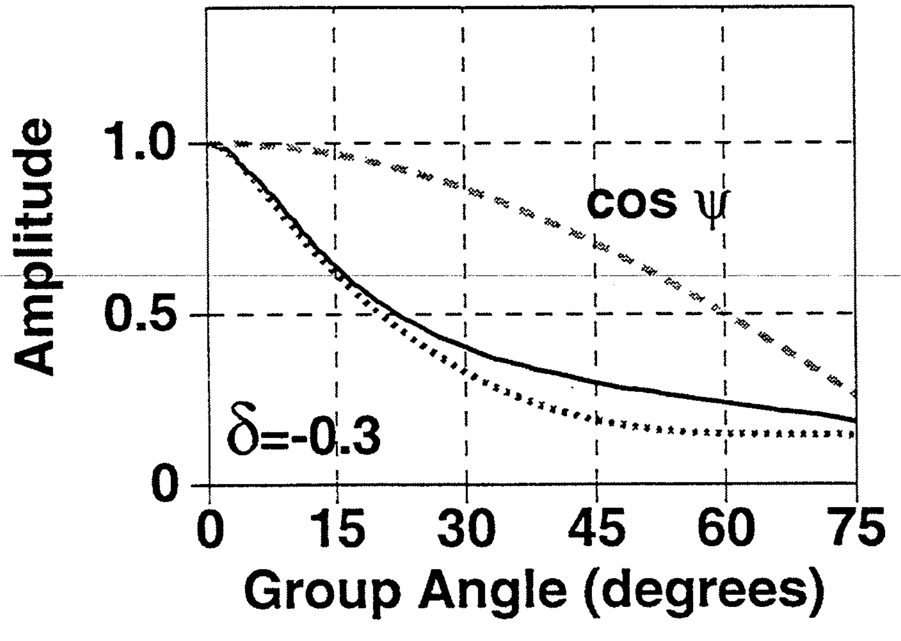

FIG. 2.11. Amplitude for the depth-migrated section of Figure 2.10 (solid line). The dotted line shows again the amplitudes predicted by equation (2.23).

tical P-waves and SH-waves. Recall that this operator is a function of the phase-velocity whose expression is the same [equations (2.11) and (2.13)] for elliptical P-wave and SH-wave modes; therefore, we expect that Gazdag's amplitudes obtained for SH-waves will be identical to those obtained for elliptical P-waves. Figure 2.12 shows impulse responses using the Gazdag method for the SH mode, for a VTI medium with V_{s0}= 2.0 km/s, and γ= 0.3. Figure 2.13 shows the theoretical amplitudes from equation (2.27) (dotted line) but instead of using F_2= constant, we use $F_2 = F_u$ where $F_u = \cos\phi$ corresponds to the directivity factor for elliptical P-waves, and with ϕ given by equation (2.26). Figure 2.13 shows that the theoretical amplitudes agree with the Gazdag-migration amplitudes from Figure 2.12.

An interesting result (shown in Appendix A) valid for elliptical P- and SH-waves is that the square-root term in equations (2.25) and (2.27) cancels exactly, along the wavefront, the $1/R$ term in those equations. That means that the only factor that controls the elliptical P-wave and SH-wave amplitudes along the wavefront is the force term F_u and F_2, respectively.

Figure 2.14 shows depth-migration impulse responses for the SH mode in the weathered gypsum. Note that because the large value of γ for this material (γ= 2.78), the horizontal semi-axis of the elliptical impulse response is almost three times larger than the vertical semi-axis. Even for this large value of γ, we see in Figure 2.14 an amplitude distribution similar to that in isotropic media, with amplitudes decaying with propagation angle. The results of Appendix A, and the Gazdag amplitudes of Figure 2.14, suggest that the amplitude distribution for the elliptical P and SH propagation mode will be weakly dependent of the anisotropy in the media.

For the SV mode, Tsvankin (1994) obtained in the weak-anisotropy approximation

$$U_{SV}(R,\theta) = \frac{F_u}{4\pi\rho V_{s0}^2 R}\frac{1+2\sigma\sin^2 2\theta + \sigma\sin^2\theta}{1+2\sigma}, \tag{2.28}$$

where $\sigma \equiv (V_{p0}/V_{s0})^2(\epsilon-\delta)$. In isotropic media, migration impulse responses produced by the Gazdag method are identical for the P and SV propagation modes (the DEO is the same for both modes). The only way that these two impulse responses can be the same and can also be produced by point forces is that they correspond to point forces directed in directions that make a 90 degree angle. Thus, if we try to relate migration impulse responses in isotropic media for the P and SV modes to radiation patterns produced by point forces, we must require that impulse responses for the P and SV modes correspond to radiation patterns produced by a vertical and horizontal point forces, respectively.

In TI media and for the SV mode, the term F_u is usually more disturbed by the anisotropy than is that for the P mode. Tsvankin (1994) also pointed out that because the P and SV polarization vectors corresponding to the same phase angle are orthogonal, we can use the P-wave formula and just add 90 degrees to calculate the SV polarization direction. Figure 2.15 shows the angular amplitude distribution for the SV mode, and for a σ value of 0.15. For this relative low value of σ, Gazdag amplitudes follow closely the amplitudes given by equation (2.28).

We have seen here that the weak-anisotropy approximation formulas of Tsvankin

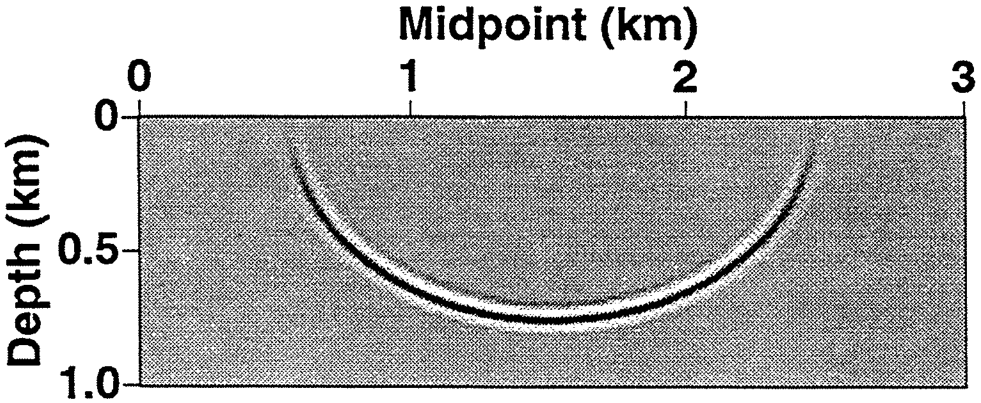

FIG. 2.12. Depth-migration impulse responses via the Gazdag method for the *SH* propagation mode, for a VTI medium with Thomsen parameters V_{s0}= 2.0 km/s, and γ= 0.3.

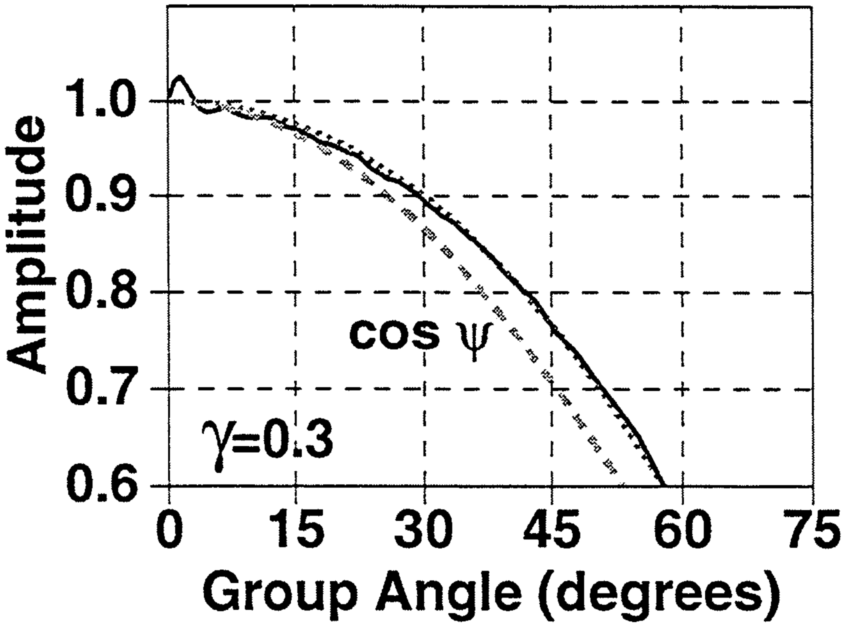

FIG. 2.13. Amplitude as a function of propagation angle for the depth-migrated section of Figure 2.12 (solid line). The dotted line shows the amplitudes predicted by equation (2.24).

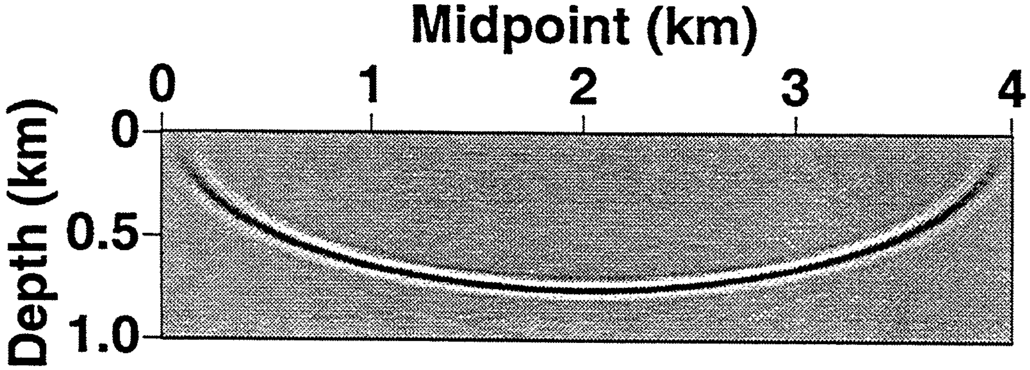

FIG. 2.14. Depth-migration impulse responses via the Gazdag method for the *SH* propagation mode in the weathered gypsum.

(1994) predicted well the observed amplitudes of migration impulse responses obtained by the Gazdag method applied to VTI media. In Chapter 3 we will compare amplitudes in impulse responses obtained by migration with explicit downward-extrapolation filters against those obtained by the Gazdag approach.

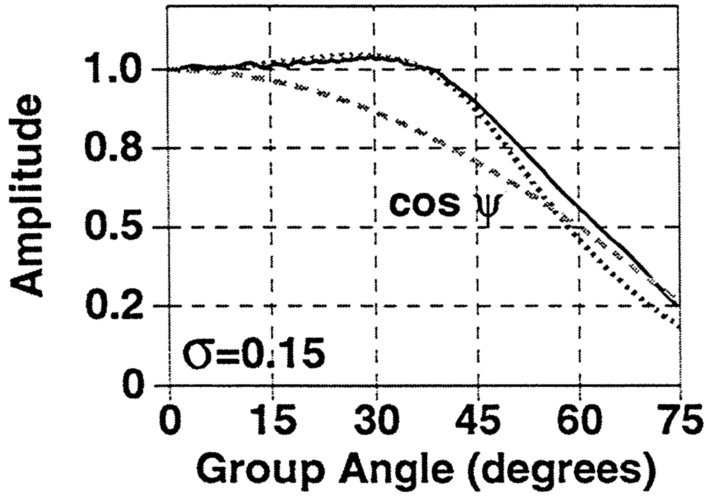

FIG. 2.15. Amplitude as a function of propagation angle for the *SV* mode and for a σ value of 0.15. Solid line: Gazdag amplitudes. Dotted line: amplitudes predicted by equation (2.28).

Chapter 3

EXPLICIT FILTERS IN TI MEDIA

3.1 Introduction

As discussed in Chapter 1, explicit filters (Holberg, 1988; Hale, 1991a) have proved to be a useful tool in the extrapolation of seismic wavefields for depth migration in isotropic media. Here, I extend their approaches to TI media. Explicit depth-extrapolation filters may be designed using any of several methods. Hale (1991a) used a modified Taylor series (MTS) expansion to obtain filters for isotropic media. Holberg (1988) obtained similar filters using a least-squares (LS) approach. Recently, Nautiyal et al. (1993) applied windowing methods (truncation of the ideal frequency response using a finite-duration, tapered window) in the design of isotropic depth-extrapolation filters. Soubaras (1992) used a minimax method to obtain isotropic depth-extrapolation filters for 2D and 3D depth migration.

Each of these methods gives filters with characteristics that limit their application in depth-extrapolation in specific ways. For example, the MTS method produces filters that are always stable, so they can be applied for several thousand steps of downward-continuation with no concern about amplitudes blowing up. However, these filters lose accuracy quickly with increasing phase-propagation angle. The LS method generates filters with a wider range of accurate propagation angles than that of the MTS method, but the filters need to be designed carefully to avoid instability. Here, I obtain stable and accurate filters in the LS method for TI media by using an iterative formulation wherein the LS problem is solved using several initial models for the filter coefficients until a sufficiently accurate and stable filter is found. As we will see later, this formulation increases the computational cost of the LS method. Designing depth-extrapolation filters by windowing is straightforward, but it also has a number of limitations. For example, the window method does not allow individual control over the errors in the propagation and evanescent regions (Oppenheim and Schafer, 1989). A prime goal in depth-extrapolation of seismic reflexion energy is to obtain small amplitude and phase errors in the propagation region ($\theta \leq 90$ degrees). The error in the evanescent region may be large. We need only ensure that filter amplitudes are less than unity to attenuate possible random noise components that can be recorded in this region.

An alternative approach to obtaining the explicit filters is to use a minimax method. In this approach, the filters are calculated in such way that the maximum error in the propagation region between the ideal and the actual response of the filter is minimized. The minimax method has been applied before in the design of zero-phase bandpass filters (McClellan, et al. 1973) and in isotropic depth-migration applications (Soubaras, 1992). As Soubaras (1992) showed for isotropic media, I will show here that the computational cost of the minimax method in obtaining the filters for TI media is far less than that of the LS method, although the accuracy of the resultant operators is similar for the two methods.

3.2 Filter design problem

The theoretical DEO for TI media was obtained from the equations of motion for elastic plane waves propagating in the vertical (x, z) plane (see Chapter 2). Here, we want to design a finite-length filter that matches the theoretical DEO in the propagation region; in the evanescent region, the filter must attenuate the energy to avoid the amplification of random noise components that are always recorded in this region. For a particular frequency ω in the propagation region, the spatial Fourier transform of the filter $W(k_x, \omega)$ must satisfy

$$W(k_x,\omega) \simeq D\left[k_x(\theta),\omega\right] = \exp\left\{ i\frac{\Delta z}{\Delta x}\left[\left(\frac{\omega\Delta x}{V_{ph}(\theta)}\right)^2 - k_x^2(\theta)\right]^{\frac{1}{2}}\right\}, \tag{3.1}$$

where $D\left[k_x(\theta),\omega\right]$ is again the exact DEO for the medium. $k_x(\theta)$ is related to the phase velocity by

$$\frac{k_x(\theta)}{\Delta x} = \frac{\omega\sin(\theta)}{V_{ph}(\theta)}. \tag{3.2}$$

The filter $W(k_x, \omega)$ can be written as (Hale, 1991a)

$$W(k_x,\omega) = \sum_{l=0}^{(N-1)/2} (2-\delta_{l0})h_l(\omega)cos(k_x l), \tag{3.3}$$

where δ_{l0} is the Kronecker delta function, $h_l(\omega)$ are complex coefficients of the filter, and N is the number of coefficients. Because $W(k_x, \omega)$ is symmetric in k_x, only $(N+1)/2$ different coefficients $h_l(\omega)$ are needed to determine the response of an N-length filter.

In all the methods implemented in this thesis to calculate explicit depth-extrapolation filters for TI media, the number of filter coefficients will be equal to 39 ($N = 39$). Hale (1991a) showed that for isotropic media explicit filters designed by the MTS method, with $N = 19$ coefficients, can propagate maximum dips of only 35 degrees with relatively good accuracy. He also found that only 15 degrees of propagation angle can be gained by doubling the number of filter coefficients from $N = 19$ to $N = 39$. In TI media, the number of degrees of propagation angle that can be gained by increasing the number of filter coefficients vary according with the anisotropy in the medium. The gain may be only a few degrees, about 5 degrees when N changes from 19 to 39 for a strongly anisotropic media [i.e., weathered gypsum, Uzcategui (1993)]. Thus, explicit filters with a low value of N (i.e., $N = 19$) can only accurately propagate low dips. On the other hand, longer filters (i.e., $N > 39$) will increase the cost of explicit depth-extrapolation, reducing the efficiency, one of the main advantages of this method. In addition, $N = 39$

was also chosen in order to compare the results obtained herein for TI media with the results obtained by Holberg (1988) and Hale (1991a) for isotropic media.

Calculating depth-extrapolation filters is basically equivalent to finding a convergent series expansion for the DEO in the propagation region. Different treatments can be used to attenuate the evanescent energy, and to improve the convergence of the Fourier series expansion.

3.2.1 Modified Taylor series (MTS) method

In the MTS method (Hale, 1991a), the filter coefficients $h_l(\omega)$ are obtained by matching the filter's Taylor expansion around $\theta = 0$ with that of the DEO in the propagation region. In particular, because the filter is symmetric and we want this filter to be exact for vertical propagation, we would like to match the first $(N+1)/2$ even derivatives at $\theta = 0$. However, to obtain attenuation in the evanescent region, we must try to match fewer than $(N+1)/2$ derivatives and let the remaining degrees of freedom in the filter be used to ensure that the amplitude of the filter is less than unity in that region $(|W(k_x,\omega)| \leq 1)$. Following Hale (1991a), I represent the filter coefficients as a sum of M weighted basis functions:

$$h_l(\omega) = \sum_{m=0}^{M-1} c_m(\omega) b_{ml}, \tag{3.4}$$

where the basis function b_{ml} is given by

$$b_{ml} = (2 - \delta_{m0}) \cos(\frac{2\pi ml}{N}). \tag{3.5}$$

The problem is now to determine the M complex weights $c_m(\omega)$. Again, to achieve stability, the number M of weights must be less than the number $(N+1)/2$ of filter coefficients, so only the first M derivatives of the Fourier transform of the filter are matched with those of the DEO for TI media. The remaining $(N+1)/2 - M$ degrees of freedom are used to ensure stability by forcing the Fourier transform of the extrapolation filters to zero at several wavenumbers in the evanescent region (see Hale, 1991a).

The Fourier transform of the extrapolation filter will be now

$$W(k_x,\omega) = \sum_{m=0}^{M-1} c_m(\omega) B_m[k_x(\theta)] \simeq D[k_x(\theta),\omega] \tag{3.6}$$

where $B_m[k_x(\theta)]$ is given by

$$B_m[k_x(\theta)] = (2 - \delta_{m0}) \sum_{l=0}^{(N-1)/2} (2 - \delta_{l0}) \cos(\frac{2\pi ml}{N}) \cos[k_x(\theta)l]. \tag{3.7}$$

The main difference between this Fourier transform of the basis function $B_m[k_x(\theta)]$ and that given by Hale (1991a) for isotropic media is that in this case (TI media) the horizontal wavenumber k_x also depends on θ through $V_{ph}(\theta)$ [see equation (3.2)]. In equation (3.6), M terms in the Taylor series expansion around $\theta = 0$ for the filter $W(k_x, \omega)$ are matched with those terms corresponding to the Taylor series expansion of the DEO $D(k_x(\theta, \omega)$. Whereas Hale's Taylor series expansions were in powers of k_x, the expansions here are in powers of θ

$$W[k_x(\theta), \omega)] \simeq \sum_{m=0}^{M-1} c_m(\omega) \left[B_m(0) + \frac{B_m^2(0)\theta^2}{2!} + \frac{B_m^4(0)\theta^4}{4!} + ... \frac{B_m^{2M}(0)\theta^{2M}}{(2M)!} \right]$$

$$D[k_x(\theta), \omega] \simeq D(0) + \frac{D^2(0)\theta^2}{2!} + \frac{D^4(0)\theta^4}{4!} + ... \frac{D^{2M}(0)\theta^{2M}}{(2M)!},$$

where $D^{(2l)}(0)$ and $B_m^{(2l)}(0)$ are the $2l^{th}$ derivatives of the downward-continuation operator and basis functions, respectively, evaluated at $\theta = 0$. The derivatives $D^{(2l)}(0)$ were obtained with the help of a computer program that performs symbolic differentiation. Even for low values of l, expressions for these derivatives are unmanageable, but they can be expressed as functions of $\Delta z/\Delta x$, $\omega \Delta x / V_{p0}$ for the P-wave mode, and $\omega \Delta x / V_{s0}$ for the SV-wave mode, and a table of numerical coefficients. Thus, for example, $D^2(0)$ is given by

$$D^2(0) = \exp\left(\frac{i\Delta z \omega \Delta x}{\Delta x V_{p0}}\right) \left\{ 1 + \frac{i\Delta z}{\Delta x} \left(\frac{-1}{V_{p0}} - \frac{\delta}{1 - V_{s0}^2/V_{p0}^2} + \epsilon \right) \frac{\omega \Delta x}{V_{p0}} \right\}.$$

For reasons given in Chapter 4, I calculate depth-extrapolation filters for each pair of ϵ and δ values, and for different ratios of $\omega\Delta x/V_{p0}$ or $\omega\Delta x/V_{s0}$ for the P and SV modes, respectively. V_{s0} can be set as a constant for the P-wave, and V_{p0} set as a constant for the SV-wave.

Matching of the Taylor expansions of the filter and downward-continuation operator above gives a linear system of equations for the coefficients $c_m(\omega)$

$$\sum_{m=0}^{M-1} c_m(\omega) B_m^{(2l)}(0) = D^{(2l)}(0) \quad l = 0, 1, ..M, \tag{3.8}$$

$$B_m^{(2l)}(0) = (2 - \delta_{m0}) \sum_{n=0}^{(N-1)/2} \cos(\frac{2\pi mn}{N}) \cos[nk_x(\theta)]^{(2l)}(0), \tag{3.9}$$

where $\cos[nk_x(\theta)]^{(2l)}(0)$ is the $2l^{th}$ derivative of $\cos[nk_x(\theta)]$ evaluated at $\theta = 0$. For isotropic media $\cos[nk_x(\theta)]^{(2l)}(0) = (-1)^{2l-1} \sum_{i=1}^{l} a_i [n\omega/V_{ph}(0)]^{2i}$, where the a_i are constant coefficients. For TI media, the cosine derivatives can still be expressed as powers of $n\omega/V_{ph}(0)$, but the coefficients a_i are now functions of the phase-velocity derivatives evaluated at $\theta = 0$.

The $D^{2l}(0)$ derivatives in equation (3.8) are complex quantities. Recall that the downward-continuation operator is a complex function in the propagation region. Therefore, to solve equation (3.8) we must solve two systems of equations, one for the real-part of $D^{2l}(0)$ and another for the imaginary-part. The system of equations [3.8] and [3.9] is solved for $c_m(\omega)$, and equation (3.4) is used to calculate the final filter coefficients $h_l(\omega)$.

In practice, equations (3.8) and (3.9) are solved for different values of M and different stable filters are found. Following Hale (1991a), we consider a stable filter to be one having an amplitude value less than 1.001 for all wavenumbers. From all the stable filters found, we choose the filter with the largest angle in the propagation region for which the phase error is less than $\pi/1000$. As described later, this phase-error criterion guarantees the application of the filter for at least 1000 steps of depth-extrapolation with an accumulated phase error of no more than one-half cycle (π radians) for dips up to that largest angle. I followed the above procedure for all of the MTS filters calculated in this thesis, so in this sense, the M value obtained for each calculated filter can be considered as an optimum value.

3.2.2 Least-squares method

For the least-squares method, the match of the Fourier transform of the filter with the downward-extrapolation operator is done over a range of discrete equal increments in phase angle ($\theta = 0, \ldots, \theta_{max}$) that correspond to a range of discrete wavenumbers ($k_x = 0, \ldots, k_{max}$). θ_{max} represents the maximum dip that can be extrapolated by a stable finite-length filter with a given maximum amplitude and phase errors in the propagation region. In isotropic media, the value of θ_{max} depends only on the filter-length and on the maximum amplitude and phase errors wanted for the propagation region (Holberg, 1988). For TI media, I show that θ_{max} also depends on the anisotropic constants in the medium. Unfortunately, I do not know of any analytical method to calculate θ_{max} for a given set of values for filter length, anisotropic constants, and maximum amplitude and phase errors in the propagation region. Here, I obtain θ_{max} values by an empirical method.

Instead of matching the Taylor series expansions for the filter and downward-extrapolation operator at $\theta = 0$, as it was done in the MTS method, the matching criterion in the LS method involves the use of the exact DEO and not its Taylor series expansion around vertical propagation ($\theta = 0$). In TI media, as we will see later, the DEO dependence on propagation angle is influenced by the anisotropy in the medium. Therefore, in the presence of anisotropy, the Taylor expansion around θ=0 may not be a good representation of the DEO, especially for high propagation angles.

Following Holberg (1988), we do the matching by minimizing the sum of the square errors in the amplitude and phase response of the filter,

$$J(\omega) = \sum_{k_x=0}^{k_x=k_{max}} (AE^2 + PE^2), \qquad (3.10)$$

subject to the constraints

$$|W(k_x, \omega)| < 1.0 \;\; for \;\; |k_x| > k_{max} = \frac{\omega sin(\theta_{max})}{V_{ph}(\theta_{max})}. \qquad (3.11)$$

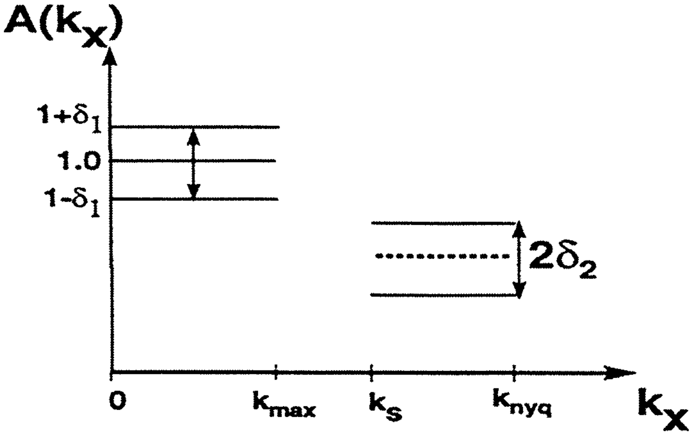

FIG. 3.1. Tolerance scheme in amplitude response for an ideal depth-extrapolation filter. δ_1 and δ_2 are the maximum allowed deviations in the propagation and evanescent regions, respectively.

Here, AE is the amplitude error of the filter, $AE \equiv 1.0 - |W(k_x, \omega)|$, and PE is the phase error of the filter, $PE \equiv k_z \Delta z - tan^{-1} \frac{Im(W(k_x,\omega))}{Re(W(k_x,\omega))}$, and again, the Fourier transform of the N-length filter $W(k_x, \omega)$ is given by equation (3.3).

Constraint (3.11) is incorporated into the least-squares problem (3.10) by adding to the objective function $J(\omega)$ a penalty function that is equal to the square of the amplitude error when the amplitude of the filter exceeds unity, so our final objective function is

$$J(\omega) = \sum_{k_x=0}^{k_x=k_{max}} (AE^2 + PE^2) + \sum_{k_x=k_{max}}^{k_x=k_{nyq}} p_f(k_x), \tag{3.12}$$

where k_{nyq} is the spatial Nyquist frequency. Although the amplitude and phase errors of the filter are given in different units (AE is non-dimensional and PE is in radians), the sizes of the two errors are similar, so no normalization was used in the minimization process. Typical amplitude and phase errors obtained are about 1/1000 and $\pi/1000$, respectively. The penalty function $p_f(k_x)$ is given by

$$p_f(k_x) = \begin{cases} AE^2, & \text{if } |W(k_x,\omega)| > 1.0, \\ 0, & \text{if } |W(k_x,\omega)| \leq 1.0. \end{cases} \tag{3.13}$$

I then use a conjugate gradient algorithm for the minimization of the non-linear least-squares problem.

3.2.3 Minimax method

Figure 3.1 shows tolerance levels used in approximating amplitudes of a depth-extrapolation operator by a finite-length filter using the minimax method. The match with the amplitude response of the operator is made in two regions, or bands, of wavenumbers. In the first band, or propagation region, unit amplitude is to be approximated with a maximum absolute error of δ_1 for horizontal wavenumbers $0 \leq k \leq k_{max}$. Here, $k_{max} = 2\omega \sin\theta_{max}/V_{ph}(\theta_{max})$ is again the maximum wavenumber in the propagation region, corresponding to a maximum design angle θ_{max}, and $V_{ph}(\theta)$ is the phase-velocity of the medium. To achieve stability in the second band, or evanescent region, either a constant value less than unity (as shown in Figure 3.1) or a decaying exponential function is to be approximated in the region $k_s \leq k \leq k_{nyq}$, with maximum absolute error of δ_2, where k_s corresponds to the stopband edge.

Oppenheim and Schafer (1989) pointed out that in the design of bandpass filters, the discontinuity between the bandpass and stopband region (jump from unity to zero amplitude) reduces the accuracy of the designed filters. For that reason, I use for wavenumbers greater than k_{max} and for the evanescent region, a decaying exponential function (described later) with an initial value equal to unity at $k = k_{max}$, and with amplitude values less than unity in the region $k_{max} \leq k \leq k_{nyq}$. Because the amplitude value of the DEO throughout the propagation region is unity, this exponential function guarantees continuity for the amplitude values of the filter, and also stability in the evanescent region. Nevertheless, Soubaras (1992) calculated explicit depth-extrapolation filters for isotropic media using a constant amplitude value of 0.7 in the evanescent region and for a maximum design angle of θ_{max}=65 degrees. The results obtained here (see section 3.5.2) for isotropic media show similar accuracy to those obtained by Soubaras (1992). I did not make a detailed study of which approach for the evanescent region (constant value less than unity or decaying exponential function) works better. However, if we are to use a constant value for the evanescent region, we must be sure of two things: First, to increase the accuracy of the filter (Oppenheim and Schafer, 1989), the constant value must be close to unity to reduce the size of the discontinuity between the propagation and the evanescent region. Second, the filter amplitude error in the evanescent region δ_2 plus the constant value must be less than unity to ensure attenuation.

In the region between k_{max} and k_s, the amplitude response of the filter is unconstrained, and no approximation error is defined. Parks and McClellan (1972) showed that with a fixed length of filter, and fixed values of k_{max}, k_s, by letting the ratio δ_2/δ_1 vary the design problem becomes a problem in Chebyshev approximation, a problem that was solved by Cheney (1966) (see Appendix B).

The initial filter design problem to solve by the minimax method is similar to the problem solved in the LS and MTS methods. We need to find a filter in frequency-midpoint (ω - x) space such that its spatial Fourier transform matches (in the propagation region) that of the DEO for TI media. In order to reproduce the DEO, two real filters are needed (one for the real part and another for the imaginary part of the operator). In the MTS and LS methods, these two real filters are calculated simultaneously. The real- and imaginary-part of the complex filter coefficients $h_l(\omega)$ in the MTS and LS methods correspond to real- and imaginary-part filters, respectively. McClellan's computer code, however, was initially designed to calculate real zero-phase bandpass filters and therefore does not allow the calculation of complex filters based on amplitude- and phase-error criteria, as is needed in the MTS and LS methods. Therefore, in the implementation of McClellan's code to calculate depth-extrapolation filters, I calculate separately the real- and imaginary-part filters for the DEO. The criterion used to calculate each one of these filters is basically an amplitude-error criterion (described below). If the amplitude error of each one of these calculated filters is small, the total amplitude error $1.0 - \sqrt{Re(W(k_x,\omega))^2 + Im(W(k_x,\omega))^2}$, and phase error $k_z \Delta z - \tan^{-1} \frac{Im(W(k_x,\omega))}{Re(W(k_x,\omega))}$ of the composite filter (real plus imaginary) will also be small.

Thus, the matching criterion in the minimax method is to equate the spatial Fourier transform of each one of these filters (real- and imaginary-part) to that of the DEO for a particular frequency ω. The matching is given by

$$\begin{aligned} &minimize\,\{max\ E(k)\ |Re\,[D(k,\omega) - W(k,\omega)]\,|\,\}\,, \\ &minimize\,\{max\ E(k)\ |Im\,[D(k,\omega) - W(k,\omega)]\,|\,\}\,, \end{aligned} \qquad (3.14)$$

where Re and Im are the real and imaginary part operators. The minimization is made for all the wavenumbers in the two bands $[0, k_{max}]$ and $[k_s, k_{nyq}]$, and $E(k)$ represents a weighting function that incorporates different approximation errors for the propagation and evanescent regions.

In general, in migration we are interested in doing downward continuation of the reflected seismic energy with high accuracy, and in attenuating the evanescent energy just enough to avoid the amplification of noise. Thus, we give more weight to the errors in the propagation region than to those in the evanescent region. A typical definition for $E(k)$ can be

$$E(k) = \begin{cases} L & 0 \le k \le k_{max}, \\ 1 & k_s \le k \le k_{nyq}, \end{cases}$$

where $L = \delta_2/\delta_1$ is a constant greater than one. This quantity is the ratio of the maximum allowed error in the evanescent region to the maximum allowed error in the propagation region.

In practice, a finite-length filter cannot achieve arbitrary small values for the errors δ_1 and δ_2. However, Parks and McClellan (1972) generated an algorithm that guarantees that for a given length of the filter and for prescribed bands $(0,k_{max})$ and (k_s, k_{nyq}), the maximum weighted error of the filter [equation(3.14)] would be minimum. The Parks and McClellan (1972) algorithm is iterative (see details in Appendix B), and the iterations will stop when a filter with maximum amplitude error equal or less than δ_1 and δ_2 [for the bands $(0,k_{max})$ and (k_s, k_{nyq}), respectively] is found.

3.3 Amplitude and phase errors in explicit depth-extrapolation

In the design of explicit depth-extrapolation filters, we try to reproduce the amplitude and phase response of the DEO; however, as we will see in this chapter, the approximation of the DEO by a finite-length filter introduces amplitude and phase errors that will distort the final depth-migrated section. In order to study the influence of the amplitude and phase errors introduced by the explicit filters, it is useful to consider the process of explicit downward continuation in the $\omega - k_x$ domain. In this domain, the equation for explicit downward continuation is given by

$$P(\omega, k_x, \Delta z) = W(\omega, k_x) P(\omega, k_x, 0). \tag{3.15}$$

The filter $W(\omega, k_x)$ will introduce an amplitude error δA and phase error δPE in every step of depth-extrapolation. With this notation, and recognizing that the current depth-extrapolation operator is $D(\omega, k_x) = \exp\{ik_z \Delta z\}$ with $k_z = \omega \cos\theta / V_{ph}(\theta)$, equation (3.15) can be written as

$$P(\omega, k_x, \Delta z) = (1 + \delta A) \exp\{i[k_z \Delta z - \delta PE]\} P(\omega, k_x, 0). \tag{3.16}$$

After N steps of depth-extrapolation, the downward continuated wavefield will be given by

$$P(\omega, k_x, z) = (1 + \delta A)^N \exp\{i[k_z z - N\delta PE]\} P(\omega, k_x, 0), \tag{3.17}$$

where $z = N\Delta z$. Equation (3.17) tell us that one single plane-wave component of the seismic wavefield $P(\omega, k_x, z)$, will be extrapolated with an amplitude error of $(1 + \delta A)^N$ and with a phase error of $-N\delta PE$. To obtain the final migrated section in the $(x - z)$ domain, we must perform a two-dimensional inverse Fourier transform and apply the imaging condition t=0 (Claerbout, 1985) to obtain

$$p(x, z) = \int\int \exp\{i[k_x x]\} P(\omega, k_x, z) d\omega dk_x. \tag{3.18}$$

In general, the amplitude and phase errors, δA and δPE, vary with frequency, and also, for a fixed frequency ω, δA and δPE vary with the dip of the reflector, given by $k_x = \omega \sin\theta / V_{ph}(\theta)$. To a rough approximation, if we take δA and δPE as average errors over all the dipping angles and independent of frequency, equations (3.17) and (3.18) will give us

$$\begin{aligned} \tilde{p}(x, z) &= (1 + \delta A)^N \exp\{-i[N\delta PE]\} \left[\int\int \exp\{i[k_x x]\} P(\omega, k_x, z) d\omega dk_x\right] \\ &= (1 + \delta A)^N \exp\{-i[N\delta PE]\} p(x, z), \end{aligned} \tag{3.19}$$

where $\tilde{p}(x, z)$ is the migrated section obtained by using the explicit depth-extrapolation filters, and $p(x, z)$ represents the exact migrated section. The final amplitude and phase errors in the migrated section obtained by explicit depth-extrapolation filters can thus be

Medium	V_{p0} km/s	V_{s0} km/s	ϵ	δ
Berea sandstone	4.206	2.664	0.002	0.020
Taylor sandstone	3.368	1.829	0.110	-0.035
Mesaverde clayshale	3.794	2.074	0.189	0.204
weathered gypsum	1.911	0.795	1.161	-0.140

Table 3.1. Vertical phase velocities (P-wave V_{p0} and S-wave V_{s0}) and Thomsen anisotropy parameters (ϵ and δ) for four TI media studied by Thomsen (1986).

roughly approximated by $(1 + \delta A)^N$ and $-N\delta PE$, respectively. This analysis has been simplistic in that I have assumed frequency-independent errors; however, as we will see in Section 3.5, the amplitude and phase errors of the filters implemented vary little with frequency. Thus, the most important errors to analyze in explicit depth extrapolation will be the filter amplitude and phase errors with reflector dip. I analyze these errors next.

3.4 Filter accuracy for a single frequency

3.4.1 MTS method

The accuracy of filters calculated using the MTS method would depend mainly on how well the Taylor series expansion of the DEO around θ=0 fits the DEO itself. In any mathematical problem where we try to approximate a function by using its Taylor series expansion, the error in the approximation (Abramowitz and Stegun, 1970) is controlled by the value of the $(n+1)th$ derivative of the function, where n is the number of terms used in the Taylor expansion. In TI media, the DEO and its derivatives with respect to θ are functions of the anisotropic constants. When the DEO is approximated by its Taylor series expansion and for a constant number of terms n, the error in the approximation will change accordingly with the values of the anisotropic constants. For TI media with values of $|\epsilon|, |\delta| << 1$, the Taylor expansion of the DEO is an accurate representation of the DEO itself, and only a few terms in the expansion are needed (Uzcategui, 1993). For strongly anisotropic media, one could expect that more terms, perhaps considerable more, would be needed to get an accurate representation of the DEO.

Figure 3.2 shows amplitude spectra of filters in the propagation region ($0° \leq \theta \leq 90°$) obtained using the Taylor series method, for several VTI media and for both propagation modes (P and SV). The vertical phase velocities and anisotropy parameters (Thomsen, 1986) for these media are given in Table 3.1. The amplitude scale displays only the region close to unity, to emphasize the stability in the propagation region. The number of terms in the expansion was $N = 39$, $\Delta z/\Delta x = 1$, and for all the cases shown, the ratio $f\Delta x/V_{ph}(0)$ (normalized frequency, in cycles) is constant and equal to 0.25. This ratio

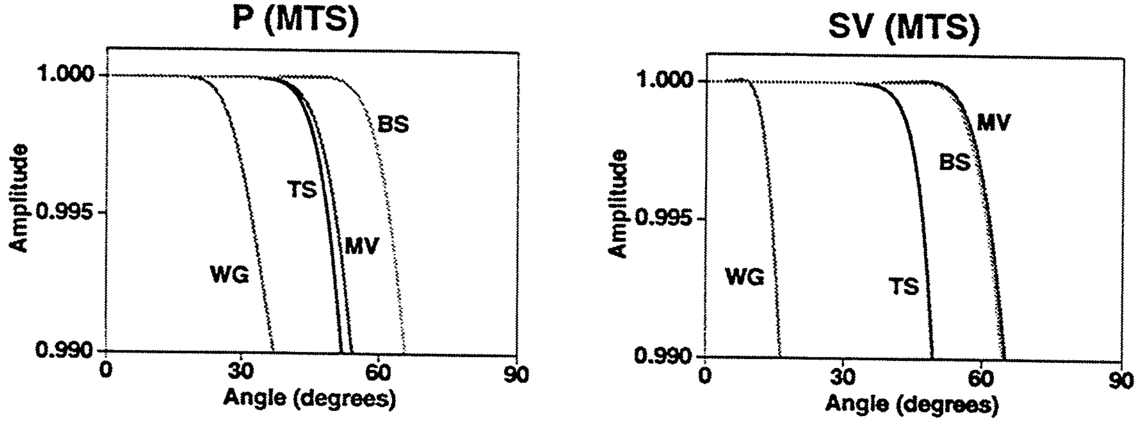

FIG. 3.2. Detailed amplitude response in the propagation region for P and SV waves, obtained using the modified Taylor series (MTS) method with N=39 coefficients. The normalized frequency is 0.25 cycles. BS= Berea sandstone, MV= Mesaverde clayshale, TS= Taylor sandstone, WG= weathered gypsum.

was kept constant because the downward-continuation operator is basically a function of $f\Delta x/V_{ph}(\theta)$. It is impossible to keep the ratio $f\Delta x/V_{ph}(\theta)$ equal for all the media and for all propagation angles θ because the phase-velocity dependence on θ changes differently in each medium. By fixing the ratio $f\Delta x/V_{ph}(0)$ we guarantee at least that the amplitude and phase of the DEO will be the same at vertical propagation (θ =0) for all these media.

All the filters calculated in Figure 3.2 show amplitude errors (1.0-$|W(k_x,\omega)|$) that are generally greater than zero. This means, that these filters produce amplitude attenuation for the larger dips. The weathered gypsum filter for the SV mode was the only one that showed an amplitude value greater than unity in the propagation region; however, the amplitude response of this filter did not exceed unity by more than 0.01 percent.

According to Thomsen (1986), a medium can be considered as weakly anisotropic if the values of the anisotropy parameters ϵ and δ are small with respect to unity. On this basis, the Berea sandstone can be considered as weakly anisotropic, the Taylor sandstone as moderately anisotropic, the weathered gypsum as highly anisotropic (not likely to be encountered), and the Mesaverde clayshale as an elliptically anisotropic material ($\epsilon \simeq \delta$). From Figure 3.2 and for the P propagation mode, we see that for the same length of the filter and ratio $f\Delta x/V_{ph}(0)$, the filters can propagate accurately (amplitude error less than 0.1 percent) to a maximum angle of some 45 degrees in the Taylor sandstone and Mesaverde clayshale, 55 degrees in the Berea sandstone, and only 25 degrees in the weathered gypsum. For the Berea sandstone, the maximum accurate propagation angle (55 degrees), is close to that found by Hale (1991a) for isotropic media. Note that for the P mode the error curves in Figure 3.2 for the Mesaverde clayshale and Taylor sandstone are similar. Although the values of ϵ and δ for Mesaverde clayshale are higher than those for

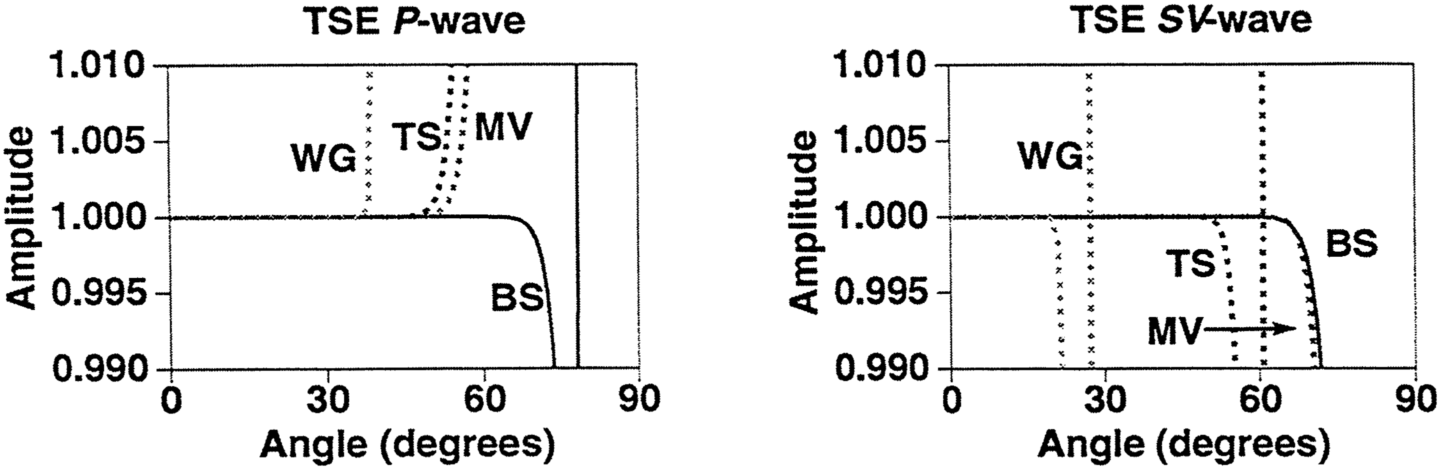

FIG. 3.3. Amplitude of Taylor series expansions (TSE) for the downward-continuation operators of the same VTI media as in Figure 3.2.

Taylor sandstone, the shape of the phase-velocity curve for $\epsilon \simeq \delta$ (Mesaverde clayshale) is more simple. As a result, the Mesaverde clayshale behaves as a moderately anisotropic material (similar to the Taylor sandstone) for the P propagation mode. Behavior similar to that for all of the amplitude curves in Figures 3.2 through 3.4 holds for phase errors as well (not shown here).

For the SV propagation mode (Figure 3.2), the filters can again propagate accurately to about 55 degrees in the Berea sandstone, and, interestingly, the filter for Mesaverde clayshale is more accurate for the SV propagation than for P propagation. The Mesaverde clayshale behaves as an isotropic material for the SV propagation mode (there is no phase-velocity dependence on θ for $\epsilon \simeq \delta$). For Taylor sandstone, accuracy is reduced somewhat to a maximum angle of 40 degrees, and, for the weathered gypsum, accurate results are confined to propagation angles less than only 15 degrees.

The results in Figure 3.2 indicate that for a given propagation mode, the accuracy of the calculated filters is influenced by the anisotropy in the media. In addition, for a fixed TI medium, filter accuracy depends on the propagation mode. The main factor that limits the accuracy of extrapolation filters calculated by the MTS method is the poorer fit of the DEO by its Taylor series expansion for increasing propagation angles. Figure 3.3 shows the amplitude error for just the Taylor series expansions of the theoretical DEO used to calculate the filters in Figure 3.2. These Taylor series expansions were used in the right-hand side of equation (3.8) to obtain the coefficients $h_l(\omega)$ in the filters of Figure 3.2. The Taylor series expansion in Figure 3.3 explain the accuracy behavior of the filters calculated in Figure 3.2. The more accurate filters in Figure 3.2 are those with smaller amplitude error in their Taylor expansions for high propagation angles. Note also that the maximum angles accurately propagated in Figure 3.3 are larger than those angles in Figure 3.2. The filters designed by the MTS method must not only match the

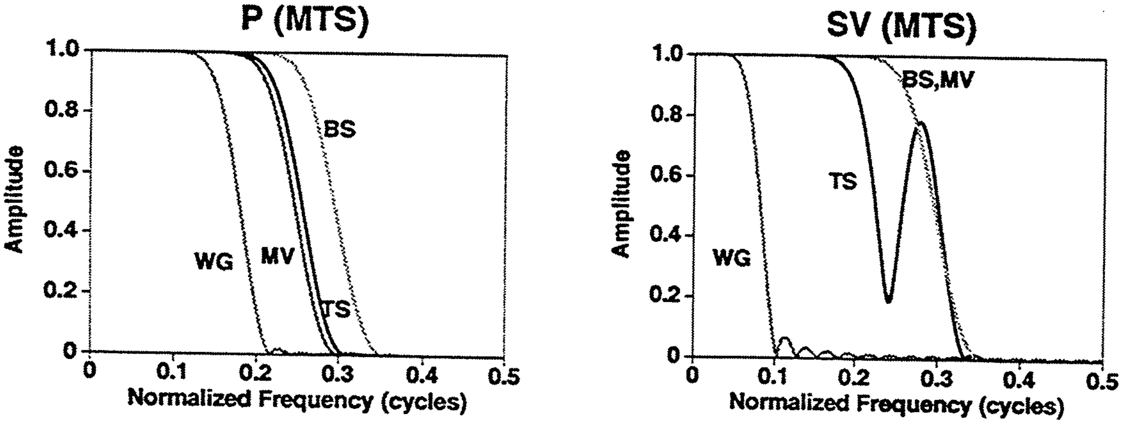

FIG. 3.4. Amplitude response for the same filters as in Figure 3.2 but now evaluated as a function of normalized frequency. Cutoff wavenumbers change for each filter according with the value of ϵ.

Taylor expansions but also attenuate the energy in the evanescent region. Therefore, some degrees of freedom have been used to obtain attenuation, so the designed filter cannot match exactly the Taylor series expansions.

Figure 3.4 shows amplitude spectra of the filters in Figure 3.2, now as a function of normalized frequency (in cycles) rather than dip; 0.5 cycles corresponds to Nyquist wavenumber ($\pi/\Delta x$). Also, the amplitude scale has been increased to show attenuation in the evanescent region. Even when the normalized frequency $f\Delta x/V_{ph}(0)$ is the same for all the filters in Figure 3.4, the limit between the propagation and evanescent region varies with the anisotropy in the medium. Spatial wavenumbers in the propagation region are given by [see equation (3.2)] $k_x(\theta) = \omega \sin\theta \Delta x/V_{ph}(\theta)$. In general, and at least for all the VTI media studied in this thesis, the spatial wavenumber is an increasing function of the propagation angle θ and reaches its maximum value in the propagation region at θ=90 degrees. Then, the cutoff wavenumber or maximum wavenumber in the propagation region is given by

$$k_c = \frac{\omega}{V_{ph}(\pi/2)}, \tag{3.20}$$

where k_c is the cutoff wavenumber. In terms of normalized frequency, the last equation can be written as

$$f_c = \frac{f\Delta x}{V_{ph}(\pi/2)}, \tag{3.21}$$

where f_c is the cutoff normalized frequency. All the filters in Figure 3.4 have a fixed value of normalized frequency at vertical propagation ($f_0 = f\Delta x/V_{ph}(0) = f\Delta x/V_{p0}$), so we can write f_c as

$$f_c = \frac{V_{p0}}{V_{ph}(\pi/2)} f_0. \tag{3.22}$$

If the medium is isotropic, $V_{ph}(0) = V_{ph}(\pi/2)$, so $f_c = f_0$. Thomsen (1986) shows that in the weak-anisotropy approximation $V_{ph}(\pi/2) = V_{p0}(1+\epsilon)$, so we can also write approximately the normalized cutoff frequency as

$$f_c = \frac{f_0}{1+\epsilon}. \tag{3.23}$$

Thus, for the four media studied, the maximum normalized frequencies f_c (in cycles) in the propagation region are about: 0.25 for the Berea sandstone, 0.22 for the Taylor sandstone, 0.21 for the Mesaverde clayshale, and only 0.12 for the weathered gypsum. The small amplitudes in Figure 3.4 for the different filters in their respective evanescent regions, show that the extrapolators are clearly stable in that region. Note also in Figure 3.4 that even when the filter for the SV mode in the Taylor sandstone presents a bump in the amplitude value in the evanescent region, the stability of this filter is guaranteed (amplitude values are still less than unity).

3.4.2 Least-squares method

In the least-squares method, the filter response is matched with the exact downward continuation operator and not with its Taylor series expansion, as done in the Taylor series method. We saw in Section 3.4.1 that the fit that the Taylor series expansion around θ =0 made with the theoretical DEO decreases for increasing propagation angles. Thus, we expect that the use of the exact DEO in the least-squares method will increase the accuracy of the calculated filters, especially for high propagation angles. However, any filter designed by using a least-squares method will have an oscillatory amplitude error known as the Gibbs phenomenon (Oppenheim and Schafer, 1989). As demonstrated by Holberg (1988), the magnitude of this oscillatory error is reduced by restricting the range of propagation angles for which the fit is done. This introduces the parameter θ_{max} [maximum design angle in equation (3.11)] in the calculation of the filter.

Although I cannot establish an analytical relationship between θ_{max} in the LS method and the optimum M value found in equations (3.8) and (3.9) in the MTS method, the two parameters have similar actions. θ_{max} and M determine the maximum dip that can be extrapolated by a stable finite-length filter with given maximum amplitude and phase errors in the propagation region by the LS and MTS methods, respectively. Whereas θ_{max} tell us directly what is the maximum angle propagated by a stable LS filter, the M value in the MTS method gives us only the order of the Taylor expansion in equation (3.8) used to calculate an optimum MTS filter. The amplitude error of this optimum MTS filter needs to be determined in order to find the maximum dip that can be extrapolated with accuracy.

For a given length of filter, there exists a maximum design angle (θ_{max}) in the least-squares method beyond which accuracy and stability are lost. This maximum allowed design angle increases somewhat as filter length increases. Here, I define an accurate and

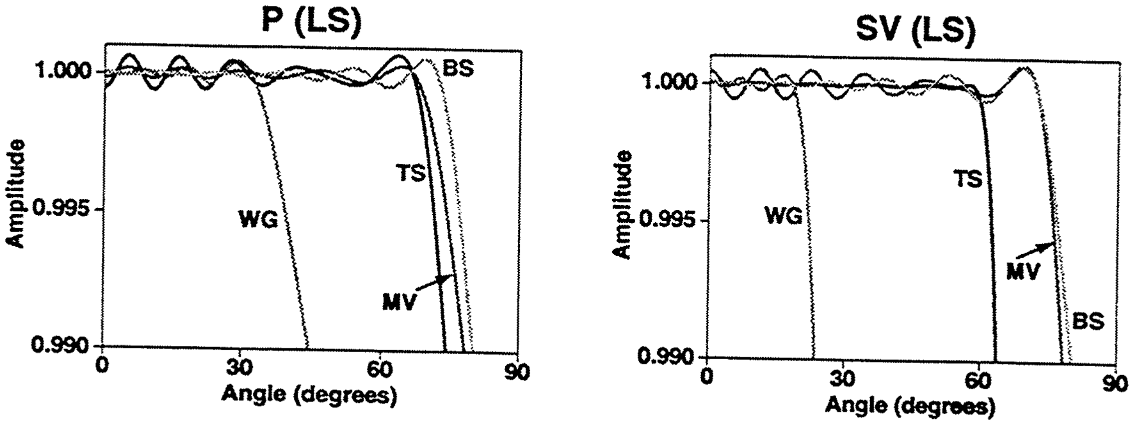

FIG. 3.5. Detailed amplitude response in the propagation region for P and SV propagation, obtained using the least-squares (LS) method with N=39 coefficients. The normalized frequency is 0.25 cycles.

stable filter as one having a maximum absolute amplitude error of no more than 0.001 in the region $\theta \leq \theta_{max}$, and amplitude values less than unity for $\theta_{max} < \theta \leq 90°$ and in the evanescent region. An N-coefficient filter cannot achieve both goals (accuracy and stability) for θ_{max} close to 90° because not enough degrees of freedom are available to satisfy both conditions. In our implementation of the LS method, the maximum design angles were obtained after several tests with different values of θ_{Test}, beginning with a high initial value of θ_{Test} and reducing this value until an accurate and stable filter was found.

Figure 3.5 shows amplitude spectra as a function of dip for the same VTI media shown in Figure 3.2 and for filters obtained using the least-squares method. The filter lengths are the same as those used to obtain the MTS results shown in Figures 3.2 and 3.4. Note the ripples in amplitude in the propagation region. Although some of these amplitude values are greater than unity, they do not exceed 1.001, which guarantees that application of these filters for about one-thousand steps of downward extrapolation would magnify amplitudes by no more than e = 2.71. [This is the same criterion as that used by Hale (1991a).] This amplitude error criterion (filter amplitudes less than 1.001) may be seen as arbitrary. It indicates only that the amplitude error for each step of depth extrapolation will be 0.1 percent. Different amplitude error criteria can be used in the design of the filters; however, because usually we have to do the process of depth extrapolation for several hundreds of steps, we must always try to use a small value (such as 0.1 percent) for this amplitude-error criterion. On the other hand, in seismic exploration oil, one-thousand steps of depth extrapolation can be seen as a typical maximum limit for depth migration. If we consider a typical small value for the sampling depth of Δz=7.5 m, one-thousand steps of depth extrapolation would correspond to 7500 m. Today, the great majority of oil targets exploited in the world are shallower than this depth.

From Figure 3.5 we see that the maximum accurate propagation angles obtained by the least-squares method are, for all media studied, greater than those obtained by the modified Taylor series method. The use of the exact DEO by the LS method allows a better fit of this operator for high propagation angles that made by the Taylor series expansion around θ=0 in the MTS method. The better fit made by the LS method allows an increase of the range of dips propagated with accuracy with respect to that of the MTS method. On the other hand, Figure 3.5 also shows that the maximum dips propagated with accuracy depends on the medium. For the four media studied, keeping N fixed at 39, the determined maximum design angles were as follows. *P* mode: 70 degrees for the Berea sandstone, 65 degrees for the Taylor sandstone and Mesaverde clayshale, and only 30 degrees for the weathered gypsum. *SV* mode: 70 degrees for the Berea sandstone and Mesaverde clayshale, 60 degrees for the Taylor sandstone, and only 20 degrees for the weathered gypsum. Changes in the filter accuracy with respect to the anisotropy in the medium will be discussed in Chapter 4.

3.4.3 Minimax method

As mentioned above, McClellan's computer code was originally designed to obtain bandpass filters, but the code can be easily changed for the design of other responses. In bandpass filters the response is just unity (bandpass region) or zero (stopband region). In depth extrapolation, the filters for the real and imaginary part of the downward-continuation operator are calculated independently. For isotropic media, the desired response of the real part of the filter for a given angular frequency ω is given by

$$Re(k) = \begin{cases} \cos\left(\Delta z\sqrt{(\omega/V_{ph})^2 - k^2}\right), & 0 \le k \le k_{max}, \\ \exp\left(-\Delta z\sqrt{(k^2 - k_{max}^2}\right), & k_s \le k \le k_{nyq}, \end{cases} \tag{3.24}$$

and for the imaginary part

$$Im(k) = \begin{cases} \sin\left(\Delta z\sqrt{(\omega/V_{ph})^2 - k^2}\right), & 0 \le k \le k_{max}, \\ 0, & k_s \le k \le k_{nyq}. \end{cases} \tag{3.25}$$

A basic algorithm to obtain the desired response of several filters designed to do depth extrapolation for a range of angular frequencies, for isotropic media, is given by

```
$for(\omega = 0, ...\omega_{max})\{$
    $k_c = 2\omega/V_{ph};$
    $k_{max} = 2\omega\sin\theta_{max}/V_{ph};$
    $for(k = 0, ...k_{nyq})\{$
        $if(k \le k_{max})D(k,\omega) = \exp\left(-i\Delta z\sqrt{k_c^2 - k^2}\right)$
```

```
            else $D(k,\omega) = \exp\left(-\Delta z\sqrt{k^2 - k_{max}^2}\right)$
        }
    }                                                   .
```

Here k_c is again the cutoff wavenumber, which bounds the propagation and evanescent regions, and ω_{max} is the maximum angular frequency to extrapolate.

For TI media, the phase-velocity V_{ph} changes with the ratio k/ω in such way that $k/\omega = 2\sin\theta/V_{ph}(\theta)$, so a basic algorithm for the desired response for TI media is

```
for($\omega = 0, ...\omega_{max}$){
    $k_{max} = 2\omega\sin(\theta_{max})/V_{ph}(\theta_{max})$;
    for($k = 0, ...k_{nyq}$){
        if($k \leq k_{max}$) then{
        locate($k/w, \theta$);
        $k_f = 2\omega/V_{ph}(\theta)$;
        $D(k,\omega) = \exp\left(-i\Delta z\sqrt{k_f^2 - k^2}\right)$}
        else $D(k,\omega) = \exp\left(-\Delta z\sqrt{k^2 - k_{max}^2}\right)$
    }
}                                                   .
```

Here, *locate* is the same inverse interpolation function used in the Gazdag migration program (section 2.6) that calculates the phase propagation angle θ from a pre-computed table of ratios k/ω.

As was done in the LS method, in the minimax method we match the filter response with the exact DEO in the propagation region. In the evanescent region, and as discussed in Section 3.2.3, we want the response of the filter to be a real decaying exponential function, so the ideal response of the imaginary filter for the evanescent region must be zero. In Figure 3.6, I show the filter response for the real and imaginary part of the downward-continuation operator calculated for an isotropic medium with a velocity $V_{ph} = 2000$ m/s and for frequency $f = 25$ Hz, $\Delta x = \Delta z = 10$ m. For these values, the normalized cutoff wavenumber is $k_c = 0.25$. The total length of the filters is again $N = 39$, and here I used $L = 50$.

From Figure 3.6 we see that in the propagation region the real-part and imaginary-part filters are successful in fitting the real and imaginary parts of equation (3.1) for isotropic media. Thus, the real- and imaginary-part filters behave as the cosine and sine, respectively, of the argument in equation (3.1). For θ=0, $k_x = \omega\sin\theta/V_{ph}(0) = 0$, and for the values of ω, Δz, and V_{ph} shown above, the argument in equation (1) is $\omega\Delta x/V_{ph}(0) = (2\pi25)10/1000 = \pi/2$, where we have replaced $V_{ph}(0)$ by half-velocity $V_{ph}(0)/2$, appropriate in depth extrapolation of CMP stacked data. So the real and

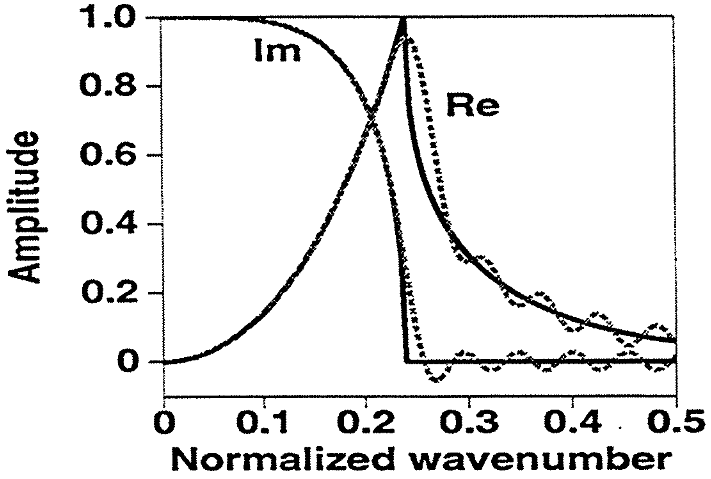

FIG. 3.6. Black solid lines: amplitude response for the real (Re) and imaginary (Im) part of the theoretical downward continuation operator calculated for an isotropic medium with V_{ph} = 2000 m/s, and for a frequency of 25 Hz. Gray dashed lines: amplitude response for calculated filters using the minimax method, with L=50 and N=39 coefficients.

imaginary part values will be 0 and 1, respectively. At the cutoff wavenumber, the argument in equation (1) is zero, so the real and imaginary parts will have values 1 and 0. Figure 3.6 also shows that with the use of a large weighting factor L, the approximation is much better for the propagation than for the evanescent region. As mentioned above, we have a trade-off between accuracy in the propagation region and stability in the evanescent region. Specifically, if too small a value of L is used, the filter would reproduce with good accuracy (more than necessary) the response of the downward continuation operator in the evanescent region, but the accuracy in the propagation region would be damaged. If a relatively large value of L is used, the accuracy in the propagation region will be better, but the amplitude in the evanescent region could be so large (greater than unity) that unstable filters would result.

Figure 3.7 compares the amplitude errors for two minimax filters with N=39 coefficients, but with two different values of L, L=50 and L=1. The amplitude error is shown as a function of the dip angle in the propagation region (left), and also as a function of the horizontal wavenumber (right) for both (propagation and evanescent) regions. In Figure 3.7, the error in the propagation region for $L = 50$ is smaller than the error for $L = 1$. The filter with L=50 shows amplitude errors less than 0.001 for propagation angles less than 60 degrees. As discussed before, this filter can be applied for at least one-thousand steps of depth-extrapolation without producing a considerable amplitude error. The quality of the fit in the evanescent region is the opposite: the filter with L=1 shows low amplitude errors in this region while the filter with L=50 shows maximum amplitude errors of about 0.04. Nevertheless, the amplitude of both filters (not shown

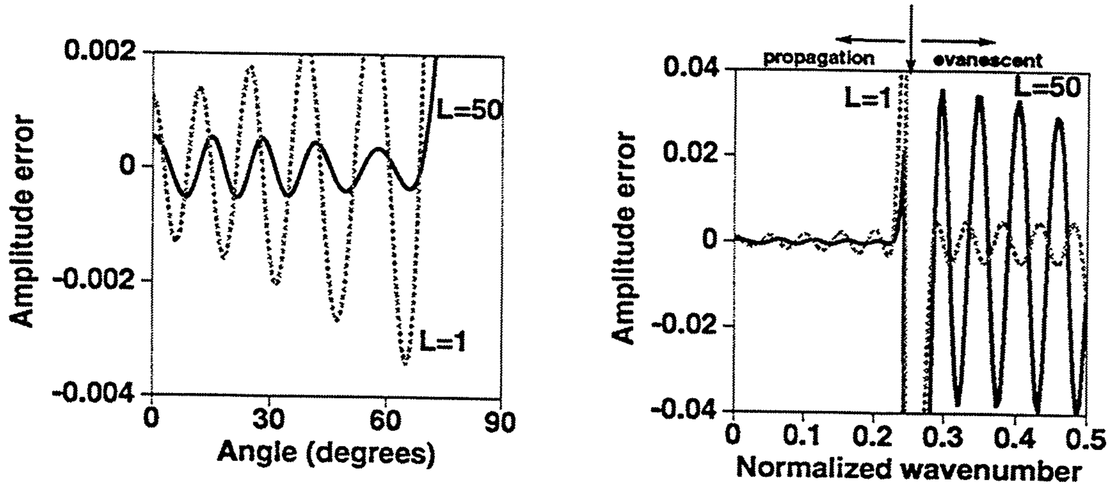

FIG. 3.7. Amplitude error of two minimax total filters (real plus imaginary part) with the same parameters as those used in Figure 3.6, but with two different values of L. Left: Error as a function of propagation angle in the propagation region. Right: Error as a function of wavenumber.

here) in the evanescent region is less than unity, so both filters are stable in this region. In practice, the L value is chosen so as to obtain the maximum accuracy in the propagation region, while preserving attenuation throughout the evanescent region. Other values of L were also tested but I found that the filter for L=50 showed stability and maximum accuracy.

The value L=50 obtained above may not be the best possible value that one might use. For all the values tested, however, L=50 was the one that allowed calculation of a stable filter with maximum accuracy. To obtain stability and maximum accuracy in the MTS and LS methods, aside from the length N of the filter, only one parameter in each method was changed; the order M of the Taylor expansion and θ_{max} in the MTS and LS methods. To reach the same goal (stability and maximum accuracy) in the minimax method, two parameters, θ_{max} and L, were needed, but in reality these two parameters are not independent. Given a fixed value for θ_{max}, only certain values of L can produce stable filters with reasonable amplitude and phase errors. On the other hand, for a fixed L, there will be a θ_{max} value beyond which no filter that is both accurate and stable can be found. Unfortunately, I was unable to find any analytical or empirical relation between L and θ_{max}, for a fixed value of N.

Figure 3.8 shows amplitude spectra as a function of dip for the same TI media shown in Figures 3.2 and 3.5, for filters obtained using the minimax method. All the filters were calculated using L=50. As in the LS spectra (Figure 3.5), the amplitude response for the minimax-derived filters have ripples, but again, they do not exceed 1.001. Note that, the maximum accurate propagation angles for all media studied are greater than those

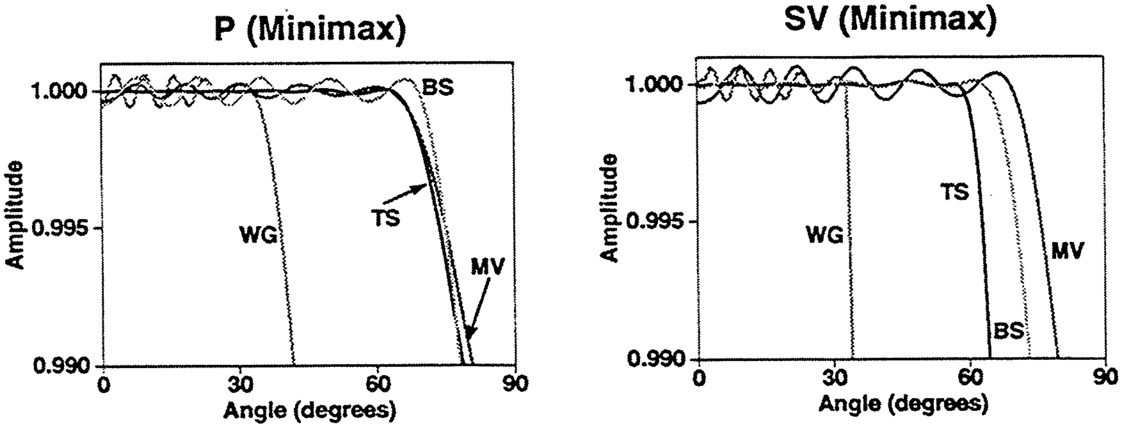

FIG. 3.8. Detailed amplitude response in the propagation region for P and SV propagation, obtained using the minimax method with 39 coefficients and L=50. The normalized frequencies are the same as those in Figure 3.5.

obtained by the MTS method, and similar to those obtained by the LS method. As was done for the LS method, the maximum design angles in Figure 3.8 were obtained after several tests with different θ_{max}.

3.5 Accuracy for a range of frequencies

In Section 3.4 we studied the accuracy of depth-extrapolation filters calculated for a single normalized frequency and we found that for all the methods implemented (MTS, LS, and minimax), the filters calculated showed limited accuracy, measured in the ability to propagate steep reflectors correctly. The results of Section 3.4 are useful because they show how the anisotropy limits the maximum dip that can be propagated for a single depth-extrapolation filter. In application to broad band seismic data, however, depth-extrapolation filters must be designed to propagate a wide range of normalized frequencies, so we also need to study how the accuracy of the filters change with normalized frequency.

3.5.1 MTS and LS methods

Figure 3.9 shows an amplitude-error contour for the Taylor sandstone using a 39-coefficient filter based on the modified Taylor series method. The contour, shown as a function of normalized frequency $\tilde{f} = f\Delta x/V_{ph}(0)$ and propagation angle, corresponds to an amplitude error of +1/1000; errors in the shaded region beneath exceed that 1/1000 threshold. Recall, the amplitude error is calculated as the difference $1.0- \mid W(\tilde{f},\theta) \mid$, so positive values in the error indicate amplitude values in the filter less than unity. An amplitude error of 1/1000 corresponds to a filter amplitude of 0.999;

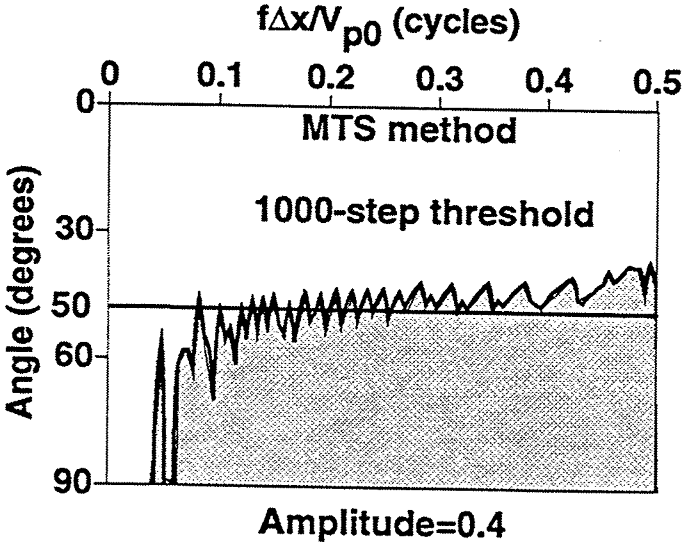

FIG. 3.9. Amplitude error for the P mode in Taylor sandstone. The 39-coefficient filter was computed by the modified Taylor series method. The contour level represents an error of 1/1000 for each step of depth extrapolation. Within the shaded zone, the accumulated amplitude error after 1000 steps is so large that results will be inaccurate for data in that zone.

after 1000 steps of downward extrapolation with this error, the amplitude of the initial waveform extrapolated will be $(0.999)^{1000} \simeq 0.4$ times the initial amplitude; this is about a 60-percent amplitude error. As mentioned earlier, 1000 steps of depth extrapolation with a small value of Δz may correspond to a depth of 7500 m, quite deep for many practical situations in oil exploration.

The 1/1000-error threshold in Figure 3.9 is more or less independent of frequency. The jagged nature of the amplitude-error contour [also seen in isotropic filters, Hale (1991a)] is produced by changes in the number of terms M, which must be an integer, needed to solve equations (3.8) and (3.9). For most of the normalized frequencies in Figure 3.9 the changes in M do not alter the maximum dip propagated by more than 5 degrees. In Section 3.4.1, we saw that the number of derivatives M matched in the propagation region for the MTS method is less than the number of filter coefficients N. M filter coefficients are used to match these derivatives and the rest of the $N-M$ coefficients are used to obtain attenuation in the evanescent region. In general, the optimum value of M increases with normalized frequency: the bandwidth of the propagation region increases with normalized frequency, so more derivative terms are needed to match a larger propagation region. At the same time, the bandwidth of the evanescent region decreases with normalized frequency, so fewer, i.e., $N-M$, filter coefficients are used to obtain stability in the evanescent region.

Figure 3.9 thus shows that, for most of the normalized frequencies, the filter for

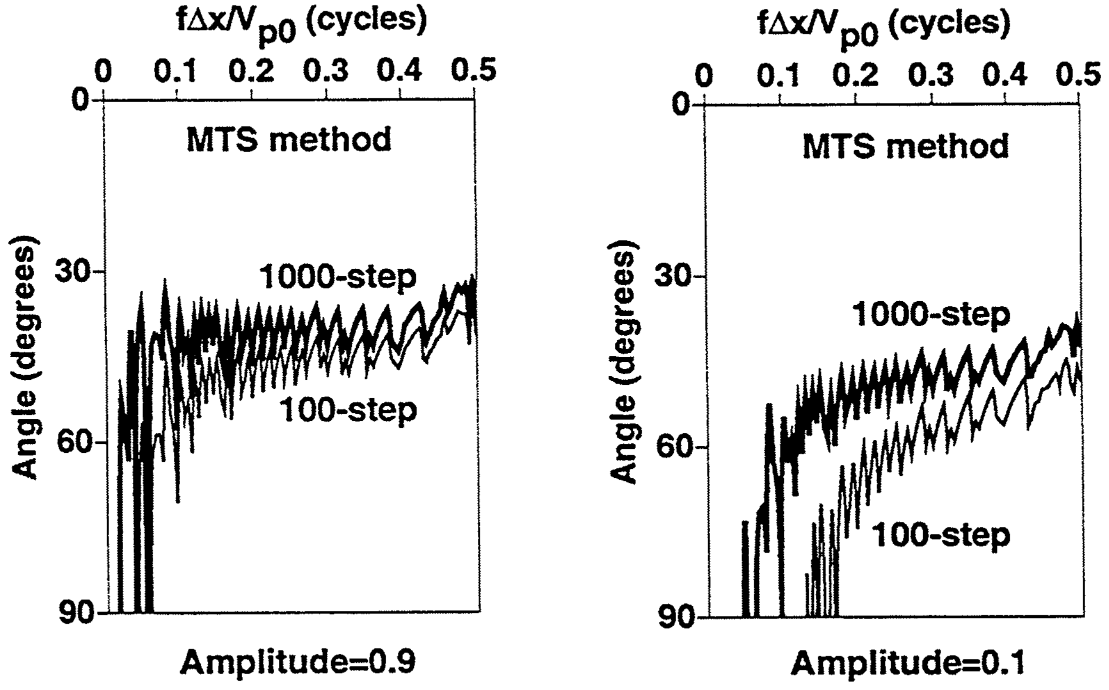

FIG. 3.10. Amplitude-error contours for the same filters as in Figure 3.9 but for accumulated attenuation factors of 0.9(left) and 0.1(right). The contour levels correspond to 1000- and 100-steps of depth-extrapolation.

Taylor sandstone will attenuate waves propagating at about 50 degrees by a factor of 0.4 after 1000 steps of downward extrapolation. Waves propagating at larger angles (the shaded zone) will be severely attenuated after 1000 steps. Therefore, the method of downward extrapolation is unacceptable for waves in the shaded region. For isotropic media, Hale's (1991a) amplitude-error contours show comparable, but slightly better, accuracy. Apparently, the anisotropy in the Taylor sandstone has not significantly reduced the accuracy of the filters calculated. Instead of the contour for 0.4 accumulated amplitude attenuation after 1000-steps of depth-extrapolation [as Hale (1991a) used for isotropic media], Figure 3.10 shows amplitude errors for the same filters as in Figure 3.9 but corresponding to attenuation factors of 0.9 (left) and 0.1 (right). The contours in each plot of Figure 3.10 are labeled with the number of extrapolation steps needed to accumulate these attenuation factors. Within the area under each contour, the filters will attenuate waves by factors of more than 0.9 (mild attenuation) and 0.1 (severe attenuation), in the left and right plots, respectively.

In Figure 3.10, for mild amplitude attenuation (factor of 0.9 corresponding to a 10 percent of amplitude error), and for almost all the normalized frequencies, the maximum dip propagated with this attenuation factor is about 45 degrees for 1000 steps of depth extrapolation. This maximum dip increases by only a few degrees when the number of extrapolation steps is reduced from 1000 to 100. That means that reflectors dipping at angles less than about 45 degrees can be propagated with about the same accuracy, independent of the number of extrapolation steps. Reflectors dipping at angles greater than about 45 degrees will be attenuated by a factor of 0.9 or more after just 100 steps of depth-extrapolation. On the other hand, for severe attenuation (factor of 0.1 corresponding to a 90-percent accumulated amplitude error), Figure 3.10 shows that the maximum dip propagated with this attenuation factor changes with normalized frequency. Also, maximum dip reduces by only 5 to 15 degrees when the number of extrapolation steps is increased from 100 to 1000. In addition, we see that reflectors dipping at 90 degrees will be attenuated by a factor of 0.1 or more for normalized frequencies greater than 0.1 cycles after just 100 steps of depth extrapolation.

In summary, Figure 3.10 shows that the MTS filters for the Taylor sandstone can propagate reflectors dipping less than about 45 degrees with good accuracy for any number of depth-extrapolation steps used in practical situations. The amplitude error for these filters is practically null for most normalized frequencies, for propagation angles less than an average angle of about 45 degrees. This amplitude error suddenly increases beyond this angle, and the filters become inaccurate, even for a small number of steps of depth extrapolation. In a qualitative way, Figure 3.10 also shows that reflections from reflectors dipping between 45 and about 60 degrees will be severely attenuated for almost all normalized frequencies. We can expect to see these reflectors in a depth-migrated section only if they are shallower than the equivalent of about 100 steps of depth extrapolation (100 Δz). On the other hand, reflections from reflectors dipping at more than 60 degrees will be so attenuated by these MTS filters that these reflectors will not be seen in the depth-migrated section even if they are quite shallow.

While the above amplitude errors indicate the attenuation of wavefields components extrapolated in depth, phase errors indicate the mispositioning of the reflectors in depth migration. Phase-error contours corresponding to the same filters in Figure 3.9. are shown in Figure 3.11. The contours corresponds to phase errors of $-\pi/1000$, $-\pi/100$, and $-\pi/10$ radians. The contours are labeled with the number of steps needed to accumulate a phase error of one-half cycle or π radians. As was the case for amplitude error in Figure 3.9, the phase-error contours in Figure 3.11 are more or less independent of frequency. Figure 3.11 also shows that these filters yield π radians of phase error after 1000 and 100 extrapolation steps for waves propagating at angles of about 50 and 60 degrees, respectively. Thus, only 10 degrees of dip propagation are gained when the number of extrapolation steps is reduced from 1000 to 100. In addition, Figure 3.11 shows that high propagation dips (greater than 60 degrees) will be extrapolated with a huge phase error. However, since Figure 3.9 shows that these high propagation dips will be attenuated, wavefield components that cannot be propagated with accuracy will be attenuated by the filters.

Figure 3.12 shows the corresponding amplitude- and phase-error contours, again for a 39-coefficient filter and the Taylor sandstone, but now using the least-squares method, with θ_{max}=65 degrees. After 1000 steps of downward extrapolation, seismic waves propagating at about 65 degrees will accumulate error that is comparable to errors for waves

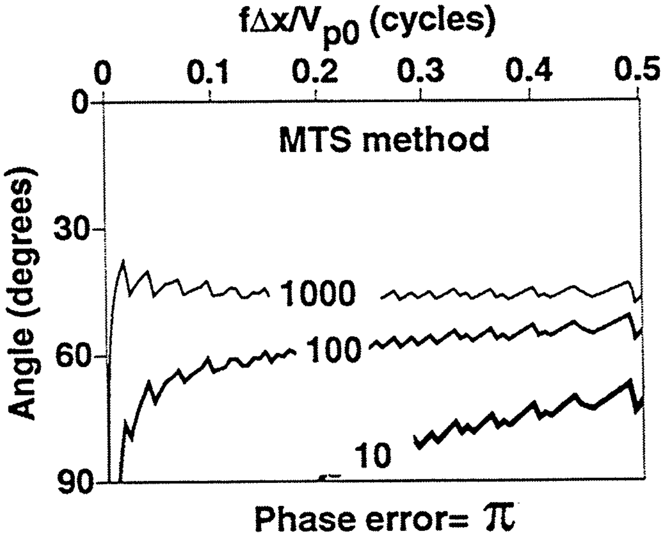

FIG. 3.11. Phase-error contours for the P mode in Taylor sandstone. The contour levels are $-\pi/1000$, $-\pi/100$, and $-\pi/10$ radians for each step of depth extrapolation. In the region beneath each labeled contour, the accumulated phase error after the corresponding steps of depth extrapolation is so large that migrated positions will be inaccurate for data in that zone.

propagating at only 50 degrees in Figure 3.9. Thus, for the same number of filter coefficients, more than 15 degrees of reflector dip has been gained through use of the least-squares approach. However, as discussed in Section 3.4.2, the amplitude error of filters designed by a least-squares method have an oscillatory character. The magnitude of these oscillations determines the filter stability and its amplitude error accumulated for every step of depth extrapolation. As opposed to MTS filters, which almost always introduce attenuation, amplitude errors for LS filters are both positive and negative; therefore, LS filters will produce both attenuation and amplification of the wavefield components extrapolated.

Figure 3.13 shows amplitude errors for the same filters as in Figure 3.12 but for an attenuation factor of 0.9 (left) and for an amplification factor of 1.1 (right). Within the shaded area in each plot, wavefield components will be attenuated by more than 0.9 after 100 steps of depth extrapolation. The upper area, with many small closed contours, shows wavefield components that will be either attenuated by a factor of 0.9, or amplified by a factor of 1.1, after 1000 extrapolation steps. The many closed contour shows the oscillatory character of LS filters. As opposed to the MTS filters, which propagate reflections from reflectors of dip less than 45 degrees with almost no amplitude error, LS filters introduce amplitude errors even for flat reflectors. However, the small contours in each plot represent an accumulated error of only ±10 percent after 1000 steps of depth extrapolation.

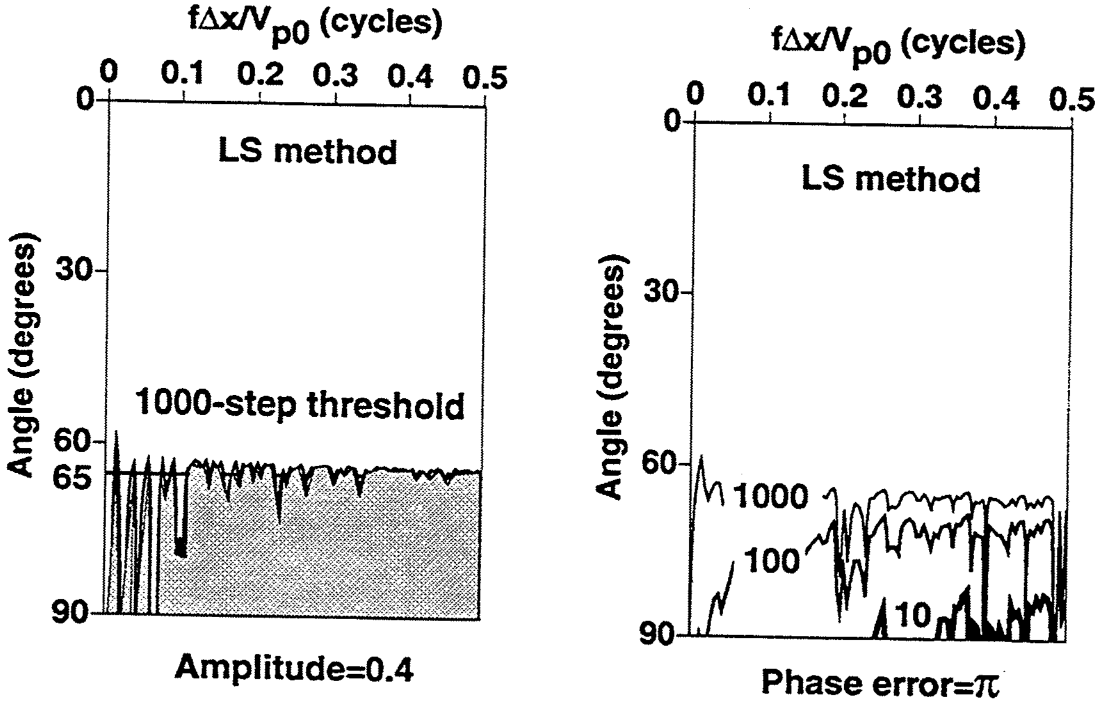

FIG. 3.12. Amplitude-error contours (left) and phase-error contours (right) for the P mode in Taylor sandstone (39-coefficient filter; least-squares method).

Thus, Figure 3.14 shows the corresponding plots for severe attenuation and amplification factors of 0.1 and 2.0, respectively. Only high propagation dips (more than 65 degrees) are attenuated by as much as a factor of 0.1. Likewise, Figure 3.14 shows that only a few wavefield components will experience an amplification factor, associated with oscillations of the response in the propagation band, of as much as 2.0. For 100 steps of extrapolation, no component will be amplified by as much as 2.0, so only the 1000-step contour is shown. It is interesting to note that many normalized frequencies have an amplification factor of 2.0 at about 60 degrees, just a few degrees before the maximum design angle θ_{max}=65 degrees used for all the filters.

Figure 3.15 compares amplitude errors in the weathered gypsum for the Taylor series and least-squares methods, again for a 0.4 attenuation factor, a 39-coefficient filter, and for the P mode. The value of θ_{max} used in the least-squares method was 30 degrees for this highly anisotropic medium. Note the small increase ($\simeq$ 5 degrees) in the range of angles for accurate propagation when the least-squares method is used. Figure 3.16 shows the corresponding errors for the SV propagation mode in the Taylor sandstone. θ_{max} in the least-squares method is 60 degrees. Comparing with Figure 3.9, we see an example here of the fact that for a given medium (Taylor sandstone), the range of angles for accurate propagation is better for the P than for the SV mode. Note in Figure 3.16 the irregular error (jump at about 0.18 cycles) in amplitude produced by the Taylor-series

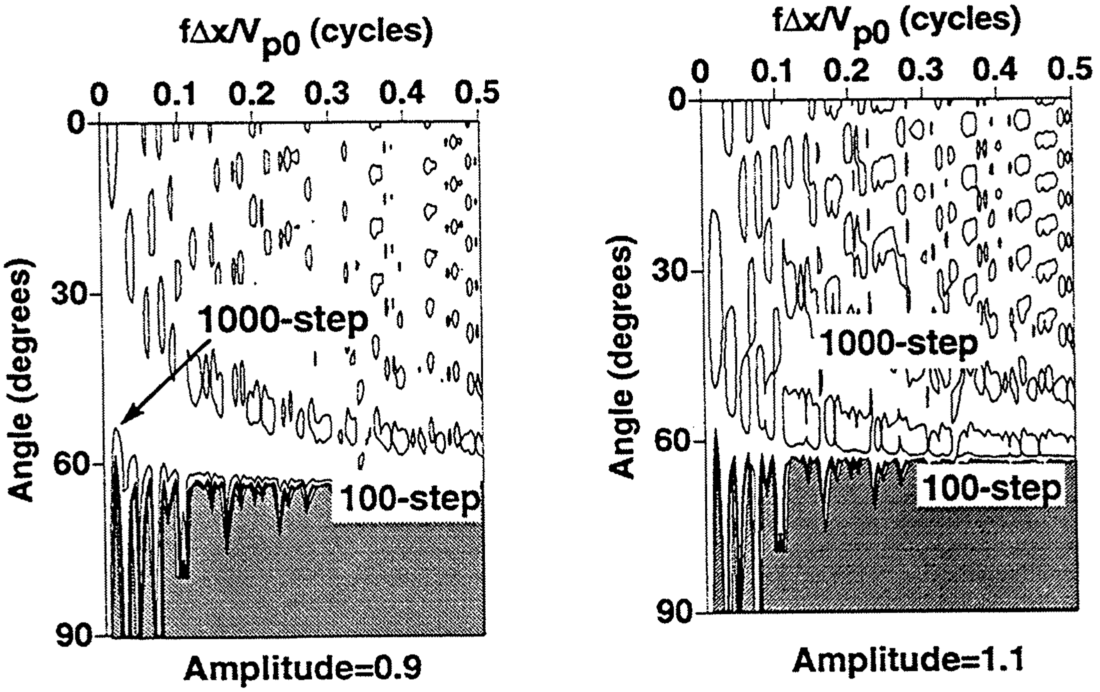

FIG. 3.13. Amplitude-error contours for the same filters as in Figure 3.12 but for accumulated amplitude errors of 0.9 (left) and 1.1 (right). The contour levels correspond to 1000- and 100-steps of depth-extrapolation.

filter. This jump was produced because an abrupt increase of the M value was needed to obtain a stable filter for that particular normalized frequency. I was unable to find an explanation for why this just happen for this particular frequency. For the least-squares filter, the error is uniform for angles less than the design angle (θ_{max} = 60 degrees). Again, as for the P mode, the least-squares designed filter is considerably superior to the MTS-designed filter.

In Figures 3.9 through 3.16, as noted above, the accuracy as measured by the contours shown, is relatively insensitive to frequency for most of the frequency range of interest. The same behavior holds for amplitude and phase errors for the Mesaverde clayshale and Berea sandstone (not shown here). For those media, the results shown in Figures 3.2, 3.5, and 3.7 for a single frequency, are representative of those over the range of frequencies of interest.

3.5.2 Minimax method

We have seen that the LS method produces depth-extrapolation filters with better accuracy than that obtained by the MTS method. Here, for a constant filter length, we compare the accuracy of the minimax method with that of the least-squares method, for isotropic and VTI media. Figure 3.17 shows the 1000-step threshold for an isotropic

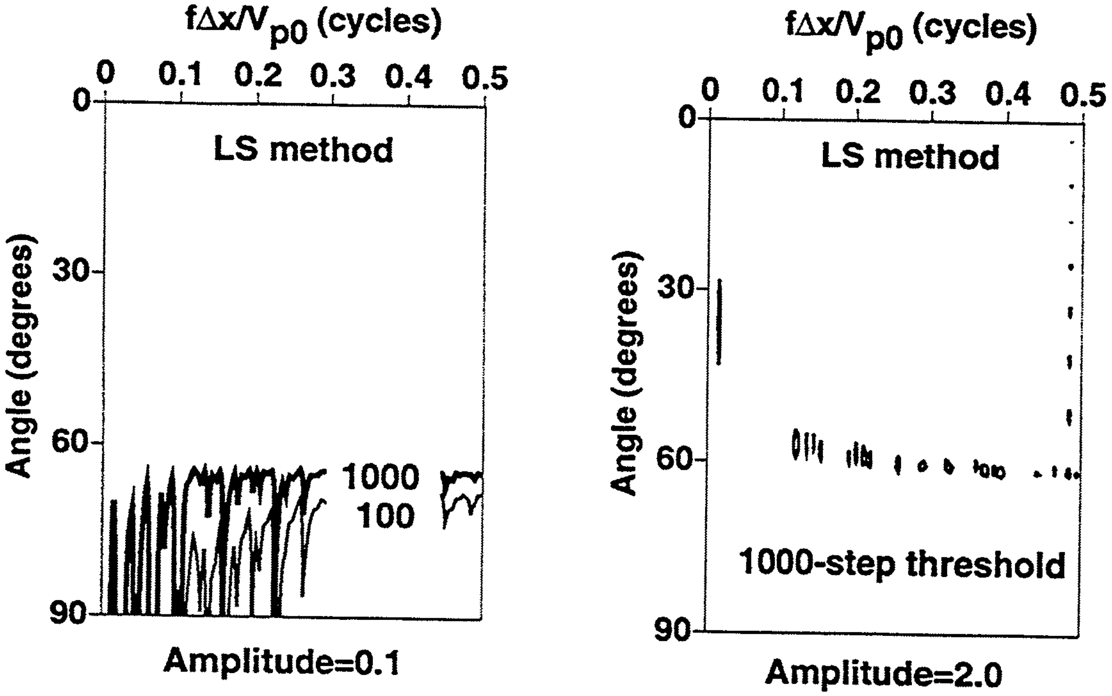

FIG. 3.14. Amplitude-error contours for the same filters as in Figure 3.12 but for accumulated amplitude errors of 0.1 (left) and 2.0 (right). The contour levels correspond to 1000- and 100-steps of depth-extrapolation.

medium using 39-coefficient filters based on the LS method (left) and on the minimax method (right). The maximum design angle in both methods is 65 degrees. In general, comparing previous results obtained by Holberg (1988) and Soubaras (1992) for isotropic media, and according to the results obtained in this thesis, θ_{max} in the LS and minimax methods are basically the same. As we will see in Chapter 4, this maximum design angle may be related to a discontinuity in the imaginary part of the DEO. Figure 3.17 can be compared with Hale's (1991a) Figure 5 which shows the same amplitude error but for filters calculated using the MTS method. Figure 3.17 shows an increase in accuracy of about 15 degrees relative to that obtained by Hale (1991a) using the MTS method. As seen in the figure, while the two filters have different accuracy at low frequency, considering the full range of frequencies both the LS and minimax filters attenuate waves propagating at about 65 degrees by a factor of 0.4 after 1000 steps of downward extrapolation.

While both filters (LS and minimax) have comparable accuracy, the computational costs are different; 105 different filters for each method were calculated in Figure 3.17. The CPU time to calculate the 105 operators on the IBM RS/6000 Model 530 workstation was 0.6 minutes for the minimax method, and 5.5 minutes for the LS method. The difference in the cost between both methods can be roughly explained if we consider that

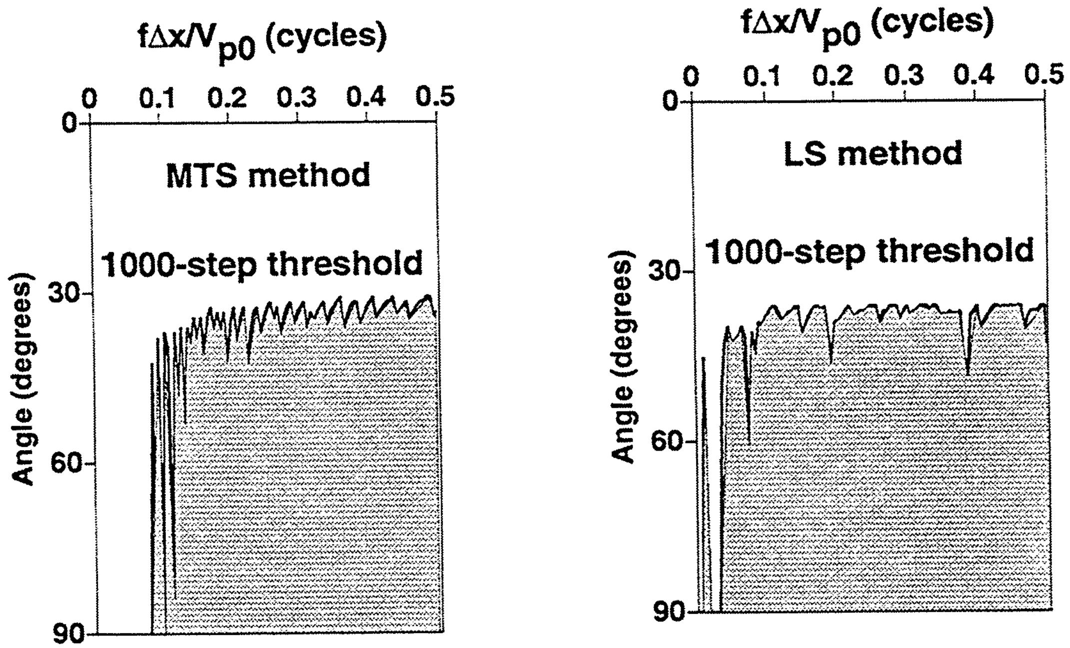

FIG. 3.15. Amplitude-error threshold for the P mode in the weathered gypsum, again for an attenuation factor of 0.4 and a 39-coefficient filter. Modified Taylor series method (left), and least-squares method (right).

for each normalized frequency, the LS method involved the minimization of equation (3.10) using a conjugate gradient algorithm. For a 39-coefficient filter, we saw in Section 3.2 that only $(39 + 1)/2 = 20$ coefficients are independent, but these coefficients are complex numbers, so equation (3.10) has to be minimized for 40 unknowns. Thus, for the LS method, the solution of equation (3.10) is equivalent to minimizing an objective function of 40 unknowns using a conjugate gradient algorithm. On the other hand, and as shown in Appendix B, the minimax method requires only an iterative evaluation of one analytic function N times and a Lagrange interpolation of an N^{th}-order trigonometric polynomial to obtain N interpolated values.

For the synthetic examples shown later in this thesis, only 105 filters were calculated for each isotropic or VTI medium. This is because the synthetic data here all involve 101 samples in time. For this number of samples in time, the number of frequency components after a fast Fourier transform in time has to be the closest power of 2, in this case, $2^7 = 128$. For a prime-factor fast Fourier transform, and for 101 samples in time, only 104 samples in frequency are required. Therefore, roughly, we try to calculate a depth extrapolation filter for each frequency component in the synthetic data. In real applications, with typical stack sections having 1000 or 1500 samples in time, many more filters are needed, and the difference between the cost of using the minimax and the least-

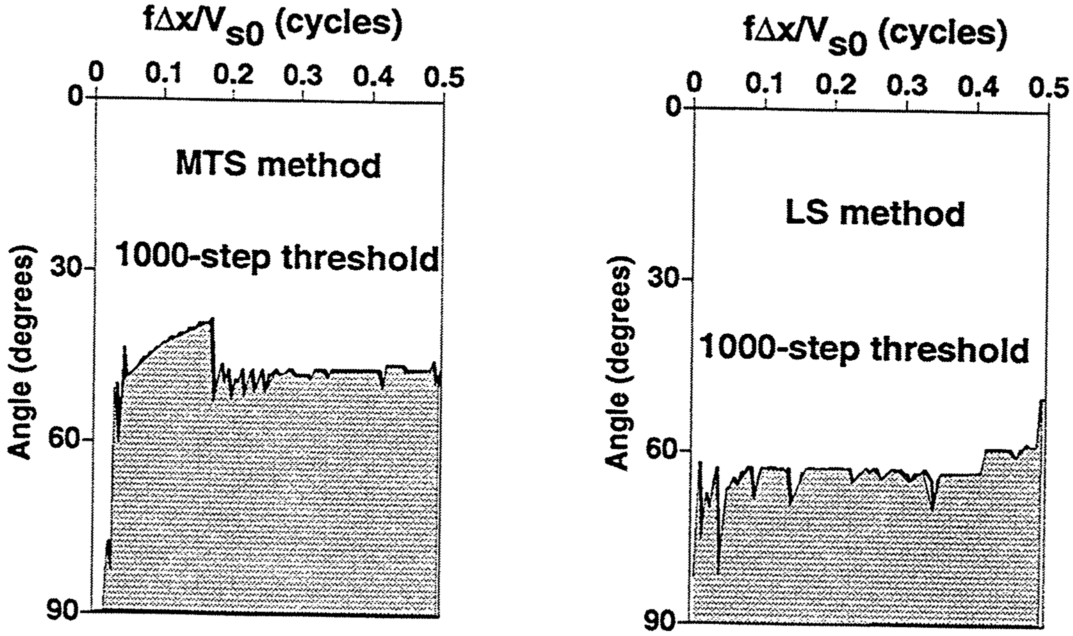

FIG. 3.16. Amplitude-error threshold for the SV mode in Taylor sandstone, for an attenuation factor of 0.4 and a 39-coefficient filter. Modified Taylor series method (left) and least-squares method (right).

squares methods will be considerable, even comparable to the cost of the depth migration itself.

In the next section, we compare the accuracy of filters computed by the three methods for TI media using migration impulse responses.

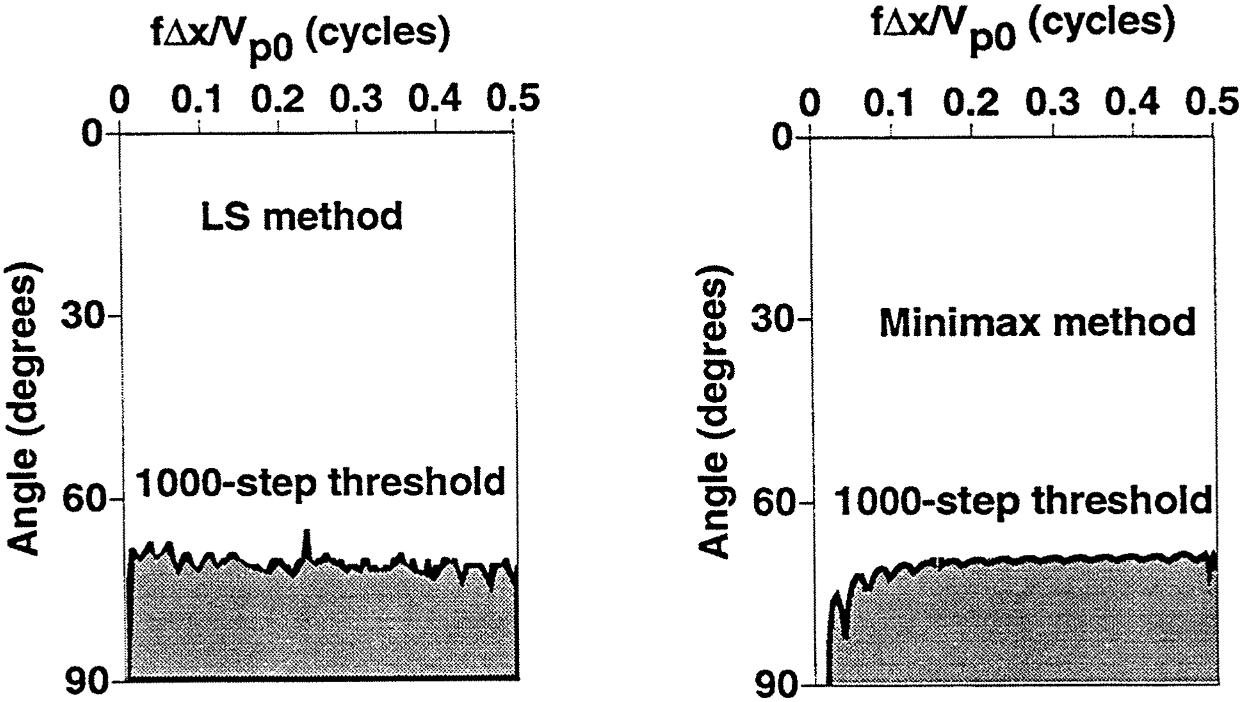

FIG. 3.17. Amplitude-error threshold for the P mode in an isotropic medium, obtained by the LS method (left) and by minimax method (right). Within the shaded zone, the accumulated amplitude error after 1000 steps is so large (greater than 6 db) that results will be inaccurate for data in that zone.

3.6 Migration impulse responses in homogenous media

3.6.1 MTS and LS methods

The performance of the operators can perhaps best be exemplified through study of migration impulse responses. The same $\omega - x$ domain migration program used by Hale (1991a) for isotropic media was used here to calculate the migration impulse responses for the P and SV propagation modes. This same program can be used for both isotropic and anisotropic media because, in migration by explicit filtering, the downward-continuation process in both cases is performed by space-variant convolution of the data with the explicit filters (Holberg, 1988). The convolution process is the same for both isotropic and TI media; we need only change the filter coefficients. In addition, the number and length of filters needed are the same for isotropic and TI media; therefore, the computational cost of migration is exactly the same, independent of the degree of anisotropy, although the accuracy of the extrapolation might be poorer for the TI medium. On the other hand, to get comparable accuracy for isotropic and TI media, fewer filter coefficients may be needed for the isotropic case. However, as Hale (1991a) showed for isotropic

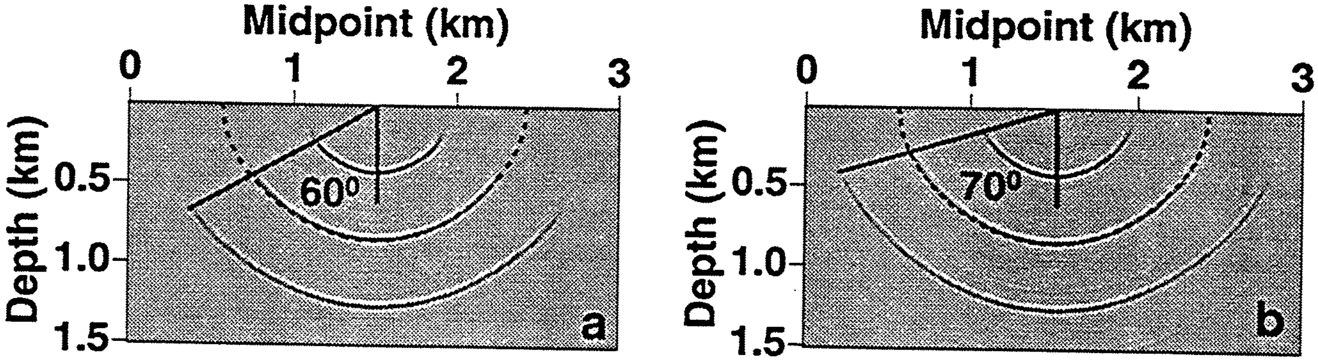

FIG. 3.18. Migration impulse responses via N=39-coefficient explicit extrapolators for the P propagation mode in Taylor sandstone. Modified Taylor series method (a), and least-squares method (b).

media, accuracy for an additional 15 degrees of dip is gained when the number of filter coefficients is doubled from N=19 to N=39. Similarly, for those TI media for which accuracy is more restricted than that for isotropic media, more coefficients might be required. Therefore, for some TI media, the cost of the depth extrapolation can be higher than that for isotropic media. However, as we will see in Section 4.3.2, the opposite holds for TI media with certain values of anisotropy parameters.

Figure 3.18 shows P impulse responses for the Taylor sandstone using the modified Taylor series method (a) and the least-squares method (b). In both tests, spatial sampling intervals $\Delta x = \Delta z = 10$ m, and the time sampling interval $\Delta t = 10$ ms; therefore, the Nyquist frequency is 50 Hz. For these parameters, the normalized frequency ($\tilde{f} = f\Delta x/V_{ph}(0)$) varies from 0 to 0.3 cycles. The trajectory of one of the theoretical impulse responses (shown in the figures as a dotted line) was calculated using the theoretical group velocity and ray angle [equations (2.21) and (2.19)] for this medium. The number of extrapolation steps needed to completely migrate each of the three impulse responses from the top to the bottom of the section were about 40, 85, and 125 steps, respectively. Note that the maximum dip propagated by the filters in each method is basically the same for all the impulse responses, and corresponds to about 60 and 70 degrees for the MTS and LS methods, respectively. Consistent with results above, the large dips are more severely attenuated by the modified Taylor series filter than by the least-squares filter. Although steep events (corresponding to high propagation angles) are attenuated for both filters, the fit with the theoretical impulse response is good for the range of angles over which the impulse responses are not severely attenuated.

The amplitude- and phase-error plots in Figures 3.10 and 3.14 can help us understand the dip limitations observed in the migration impulse responses of Figure 3.18. However, it would be difficult try to explain completely the results in Figure 3.18 using only those amplitude- and phase-error threshold plots, because those plots were calculated for just

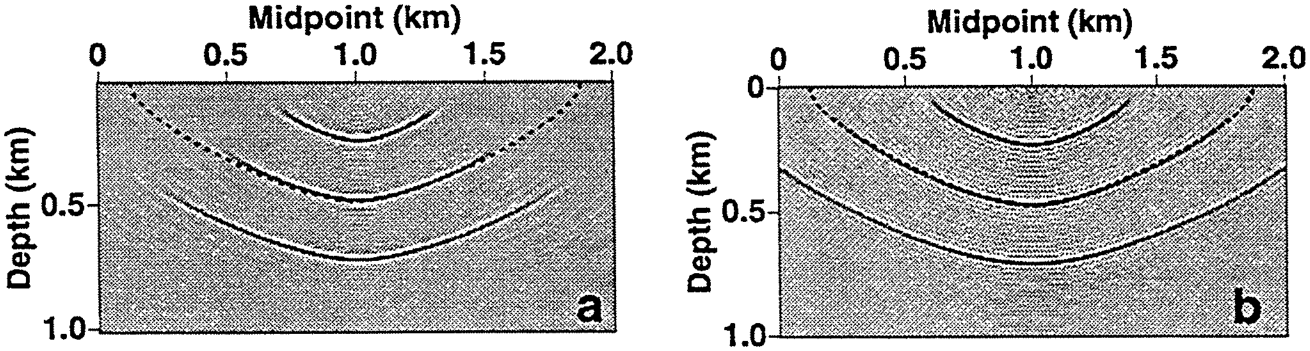

FIG. 3.19. Migration impulse responses via N=39-coefficient explicit extrapolators for the P propagation mode in the weathered gypsum. Modified Taylor series method (a) and least-squares method (b).

a few selected attenuation factors. Although Figures 3.10 and 3.14 were calculated for severe attenuation factors of 0.1, these figures roughly show the maximum dips that would be seen in a depth-migrated section calculated using these filters. Thus, for the MTS method, Figure 3.10 shows that for dip less than 60 degrees and normalized frequencies less than 0.3 cycles, wavefield components will be attenuated by a factor of 0.1 or less after 100 steps of extrapolation. The maximum propagation angle observed in Figure 3.18a corresponds to about 60 degrees. For the LS method, Figure 3.14 shows that dip less than 70 degrees and normalized frequencies less than 0.3 cycles will also be attenuated by a factor of 0.1 or less after 100 extrapolation steps. Seventy degrees is basically the maximum propagation angle observed in Figure 3.18b.

Figure 3.19 shows P impulse responses for the highly anisotropic weathered gypsum, using the modified Taylor series method (a) and the least-squares method (b). The largest dip present in this response is lower than that obtained for the P-mode Taylor sandstone filter (compare with Figure 3.18). The filters for the highly anisotropic weathered gypsum are much less accurate than the filters for the Taylor sandstone.

Figure 3.20 shows SV impulses for Taylor sandstone (a) and Mesaverde clayshale (b), respectively. Both responses were calculated using 39-coefficient filters derived by the more accurate least-squares method. Note the attenuation at large dips for the Taylor sandstone. However, for the Mesaverde clayshale, steep events can be propagated accurately. Given the same number of coefficients for both media, more accurate propagation of the SV wave is obtained for the nearly elliptical Mesaverde clayshale.

3.6.2 LS and Minimax methods

Figure 3.21 shows P impulse responses for isotropic media using the LS method (a) and the minimax method (b). In both tests, spatial sampling intervals $\Delta x = \Delta z = 10$ m,

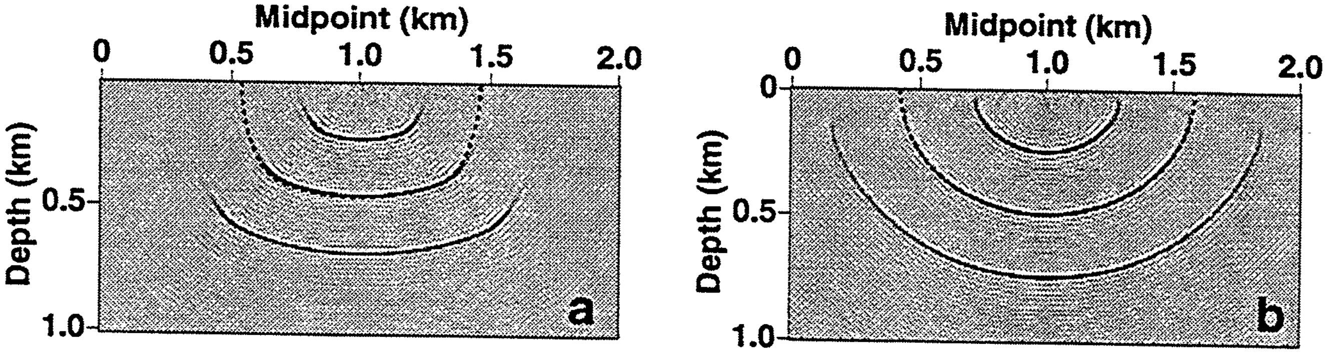

FIG. 3.20. Migration impulse responses via N=39-coefficient, explicit extrapolators for SV waves in the Taylor sandstone (a) and SV waves in the Mesaverde clayshale (b). Least-squares method.

the time sampling interval $\Delta t = 10$ ms, and the velocity $v = 2$ km/s. The only nonzero input trace, located at $x = 1.0$ km, contained a single zero-phase Ricker wavelet centered at $t = 1.0$ s, with a peak frequency of 45 Hz. The two impulse responses look almost identical.

Figure 3.22 shows P impulse responses using the LS method (a) and the minimax method (b) for a vertical transversely isotropic medium with Thomsen parameters $V_{p0} =$ 2.0 km/s, $V_{s0} = 1.0$ km/s, $\epsilon = 0.0$, and $\delta =$ -0.2. In both methods, the maximum design angle used was 65 degrees. The CPU time required to calculate the explicit operators was 0.9 minutes for the minimax method, and 6.0 minutes for the LS method. Again, it is difficult to see differences in the two impulse responses. For comparison, Figure 3.23 shows impulse responses for a medium that is the same as that of Figure 3.22, except that now $\epsilon = 0.3$ and $\delta = 0.2$. I change only the values of ϵ and δ, because (as I will show in the next chapter) V_{p0} and V_{s0} have no influence on the shape of the P migration impulse response. Compared with the results in Figures 3.21 and 3.22, the impulse responses here are broader. Thus, the maximum midpoint value shown is now 3 km, and the nonzero input trace, located at $x = 1.5$ km, contains the same zero-phase Ricker wavelet used in Figures 3.21 and 3.22. The midpoint range was increased relative to that in Figure 3.22 because the higher ϵ value implies a higher horizontal P velocity, which broadens the impulse response. For this test, the CPU time required to calculate the explicit operators was 1.1 minutes for the minimax method, and 6.5 minutes for the LS method.

As opposed to migration of diffraction hyperbolas where the migration aperture plays an important role in the collapsing of the energy, depth migration of a single impulse in a zero-offset section ($x - t$ domain) distributes the energy of this impulse along a locus of points (migration impulse response) in the $x - z$ domain, so the migration aperture only limits the final size of this impulse response. For most of the impulse responses shown in this thesis, the migration aperture used was just enough to see propagation angles of 90

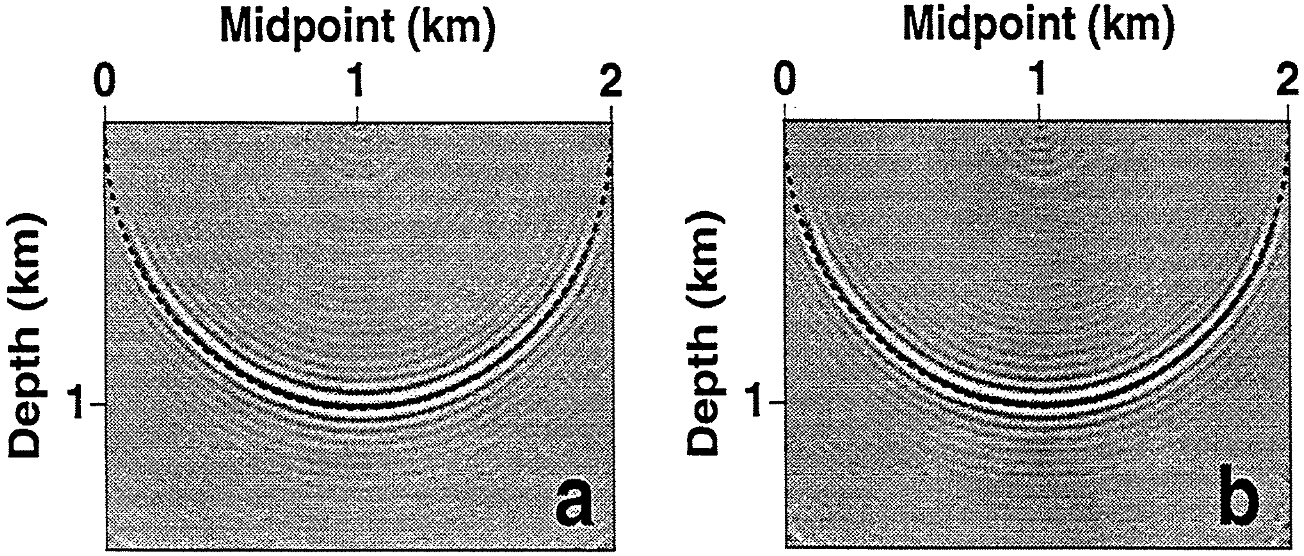

FIG. 3.21. Migration impulse responses via N=39-coefficient explicit extrapolators for the P propagation mode in isotropic media. Least-squares (a) and minimax (b) methods. The dashed curves represent the exact impulse response.

degrees; therefore, the dip limitations observed in the calculated impulse responses are due solely to dip limitations in the filters.

Figure 3.24 summarizes the accuracy characteristics of the three methods implemented. Three impulse responses for the P mode in the Taylor sandstone were calculated using the MTS, LS, and minimax methods. The impulse response on the MTS method shows a maximum propagation angle of 60 degrees, while the LS and minimax impulse responses show a maximum propagation angle of 70 degrees. In all the three methods, the position of the theoretical impulse response (dotted line) is honored for the range of propagation angles shown in the figures. While the accuracy in the LS and minimax methods is basically the same, the CPU time required to calculate the explicit operators in the LS method is again almost five times longer than the time required in the minimax method. Even the less accurate MTS method is twice as slow as the minimax method for calculating the explicit operators.

It is difficult to establish a direct expression for the computational cost of the MTS method in calculating the extrapolation filters. We already saw in Section 3.2 that the MTS method requires the solution of several linear system of equations with sizes depending on the number of derivatives M matched; therefore, the cost to calculate a single filter in the MTS method changes with normalized frequency. Low normalized frequencies require use of a small number of values M (see Section 3.5.1), so small systems of equations would result. For high normalized frequencies, M approaches the number

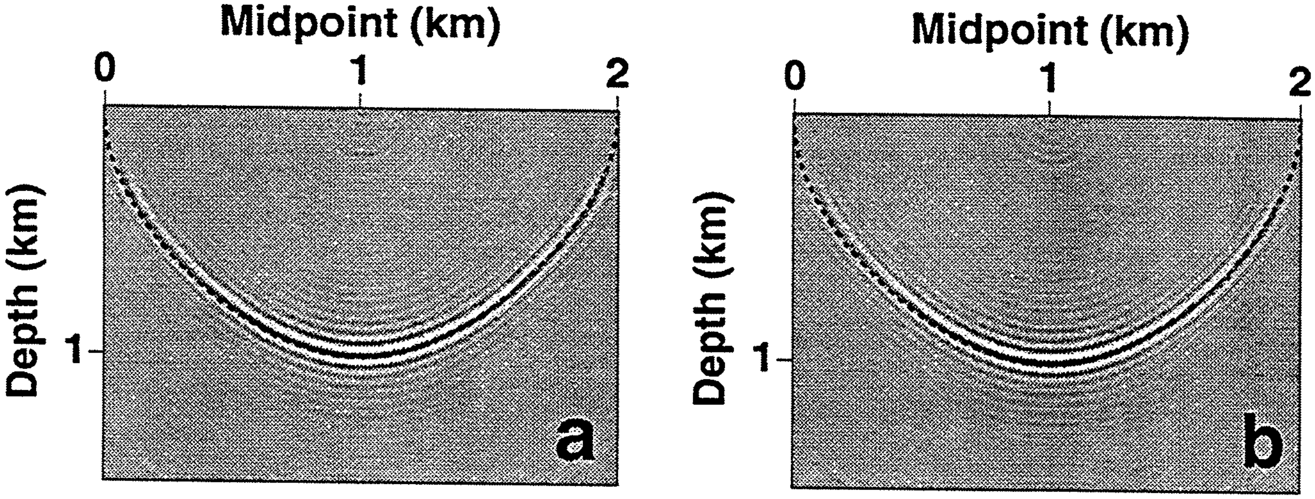

FIG. 3.22. Migration impulse responses via N=39-coefficient explicit extrapolators for the P propagation mode in a TI medium with ϵ = 0.0 and δ = -0.2. Least-squares (a) and minimax (b) methods.

of independent filter coefficients $(N+1)/2$, so the cost would not be greater than that of solving a linear system of equations of $(N+1)/2$ by $(N+1)/2$. On the other hand, as discussed before, the computer cost in the minimax method is independent of frequency and requires only an iterative evaluation of one analytic function N times and a Lagrange interpolation of an N^{th}-order trigonometric polynomial to obtain N interpolated values (see Appendix B).

To calculate downward continuation filters for the SV mode, the same algorithms can again be used. The only change is that now we use the SV phase-velocity function. Figure 3.25 shows SV impulse responses for the LS (a) and minimax method (b), for a medium with the same Thomsen parameters used in Figure 3.22. In both methods, the maximum design angle used was 65 degrees. Curiously, the minimax impulse response can handle the triplication better than does the LS impulse response. As we see in Figure 3.25, the fit with the theoretical triplication (dotted line) obtained by the LS method is worse than the fit obtained using the minimax method. Much the same as for the previous examples, the CPU time required to calculate the explicit operators here was 0.9 minutes for the minimax method, and 6.0 minutes for the LS method. For comparison, the CPU time taken in the migration step itself was 2.3 minutes. This is about a third the time required just to calculate the filters in the LS approach. Therefore, use of the minimax approach entails considerable savings for the overall migration process (3.2 minutes versus 8.3 minutes). Speed and accuracy were the main reasons for Soubaras (1992) to try the

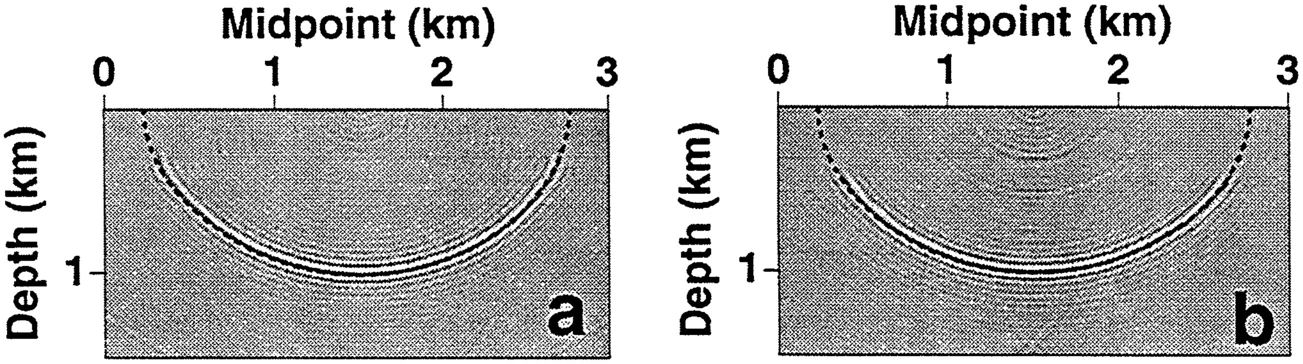

FIG. 3.23. Migration impulse responses via N=39-coefficient explicit extrapolators for the P propagation mode with $\epsilon = 0.3$ and $\delta = 0.2$. Least-squares (a) and minimax (b) methods.

minimax method to calculate isotropic depth-extrapolation filters.

As discussed before, in real applications where some 1000 extrapolators may be needed, roughly, multiplying by 10 the times above, the LS method would need about 60 minutes to calculate a table of 1000 extrapolators against some 9 minutes needed by the minimax method. Naturally, the total cost of depth migration would depend on the samples in time and midpoints to migrate in a zero-offset section, but for a typical stack section of some 1000 midpoints and 1000 samples in time, the cost of depth migration by using explicit operators would be roughly 6 hours. For cases like this, the minimax method would represent a considerable saving in time for the overall migration process.

Figure 3.26 summarizes the accuracy characteristics for the SV mode of the three implemented methods. Three impulse responses for the SV mode and for a constant value of σ=1.6, were calculated using the MTS, LS, and minimax methods. The filters were calculated for a constant value of σ because (as I show in the next chapter) this parameter mainly controls the depth-migration impulse response for the SV mode. Figure 3.26 shows that the MTS method is unable to reproduce the triplications in the impulse response. For this relative high value of σ, the phase velocity (and therefore, the DEO) changes rapidly with propagation angle, and the Taylor expansion around θ=0 in the MTS method loses accuracy quickly with propagation angle. In contrast, the LS and minimax methods use the exact expression for the DEO, and the accuracy in both methods is limited by other factors (see Chapter 4).

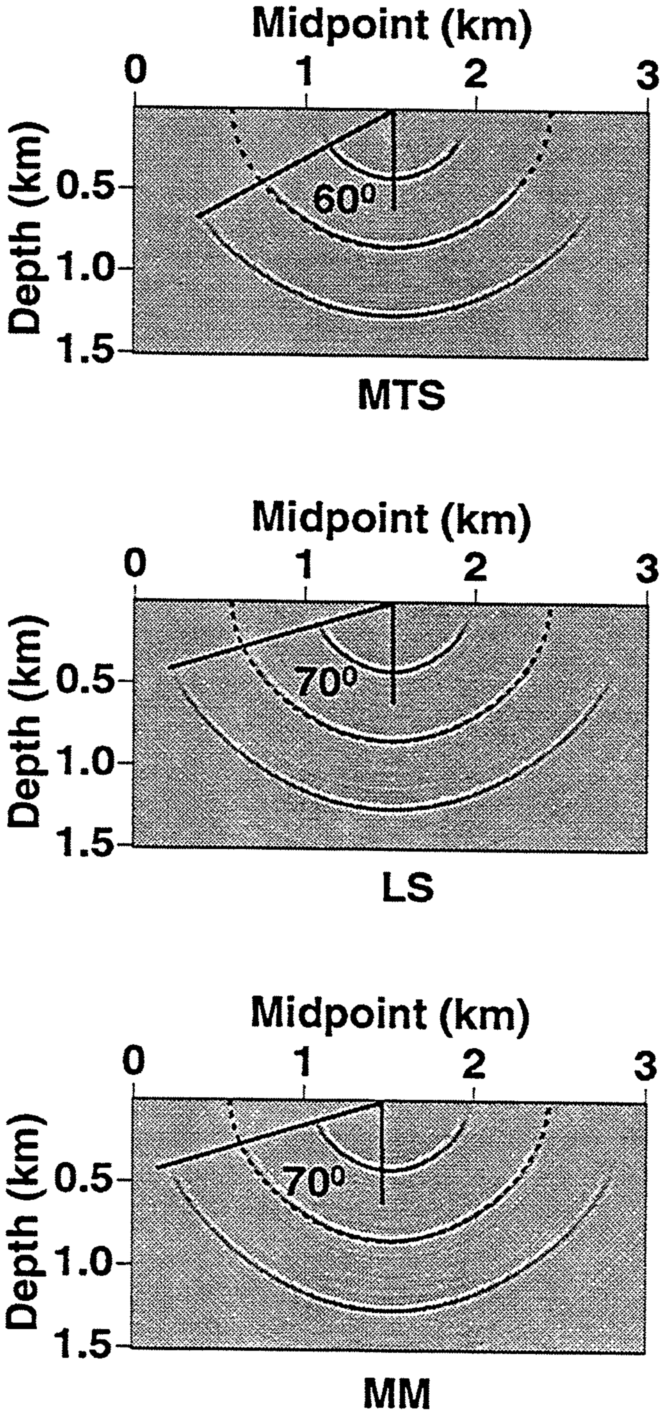

FIG. 3.24. Migration impulse responses via N=39-coefficient explicit extrapolators for the P propagation mode in Taylor sandstone using the MTS, LS, and minimax (MM) methods.

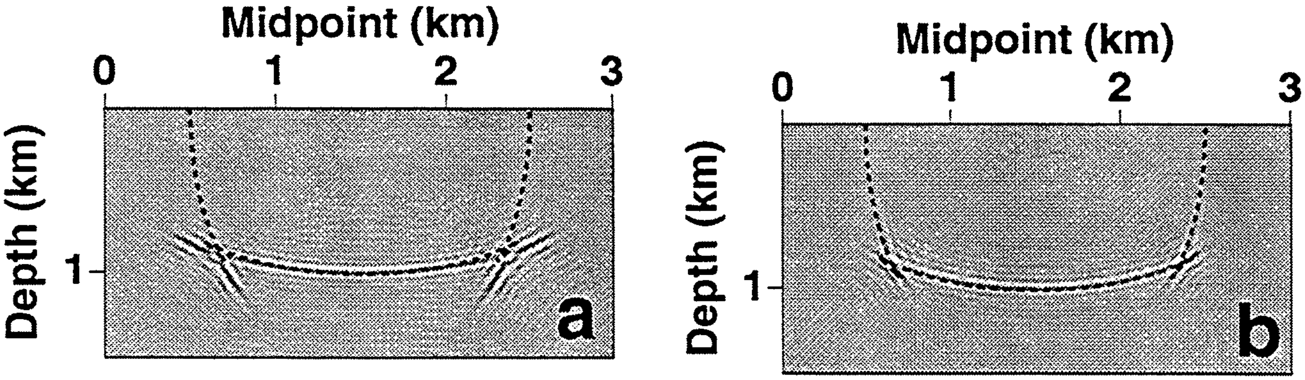

FIG. 3.25. Migration impulse responses via N=39-coefficient explicit extrapolators for the *SV* propagation mode with $\epsilon = 0.0$ and δ = -0.2. Least-squares (a) and minimax (b) methods.

3.7 Angular amplitude distribution in explicit depth-extrapolation

In Section 2.7 we compared the amplitudes of depth-migration impulse responses in TI media using a Gazdag algorithm against the amplitudes obtained by Tsvankin (1994) using a weak-anisotropic approximation. The results showed that the two amplitudes agree for a wide range of propagation angles, and that only when the weak-anisotropic condition is violated do the amplitudes differ.

Figure 3.27 shows maximum wavelet amplitude values of the *P*-wave as a function of group angle for depth-migration impulse responses (not shown here) obtained using the Gazdag method (solid black line), the MTS method (dotted black line), the LS method with θ_{max}=60 degrees (dotted gray line), and the minimax method with θ_{max}=60 degrees (solid gray line). The VTI medium has Thomsen parameters V_{p0}= 2.0 km/s, V_{s0}= 1.0 km/s, ϵ=0.0, and δ=-0.3. In the test, I use the same spatial and time sampling intervals used in Figure 2.5 ($\Delta x = \Delta z = 10$ m; $\Delta t = 10$ ms.). The depth-migration impulse response was calculated with up to 100 steps of depth extrapolation. Figure 3.27 shows that MTS amplitudes follow closely the Gazdag amplitudes for group angles less than 45 degrees. For the same range of group angles, LS and minimax amplitudes also follow closely the Gazdag amplitudes but with larger errors than MTS amplitudes. Beyond 45 degrees, the LS and minimax amplitudes are closer to Gazdag amplitudes than are the MTS amplitudes.

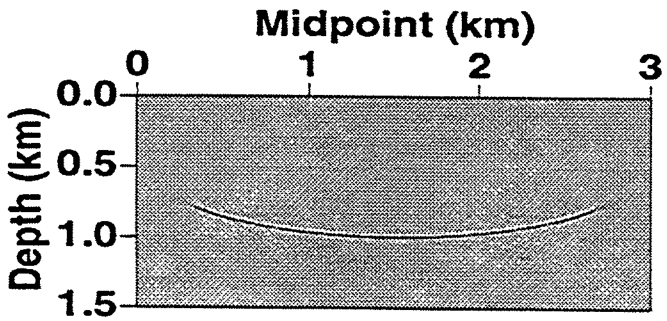

MTS

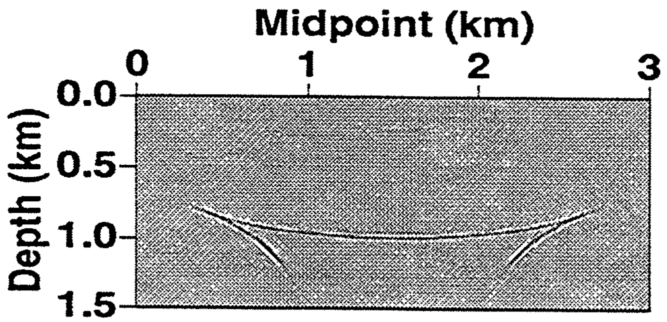

LS

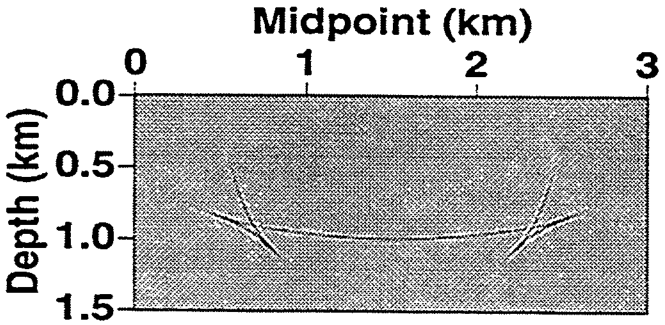

MM

FIG. 3.26. Migration impulse response via N=39-coefficient explicit extrapolators for the *SV* propagation mode with σ= 1.6 using the MTS, the LS, and the minimax (MM) methods.

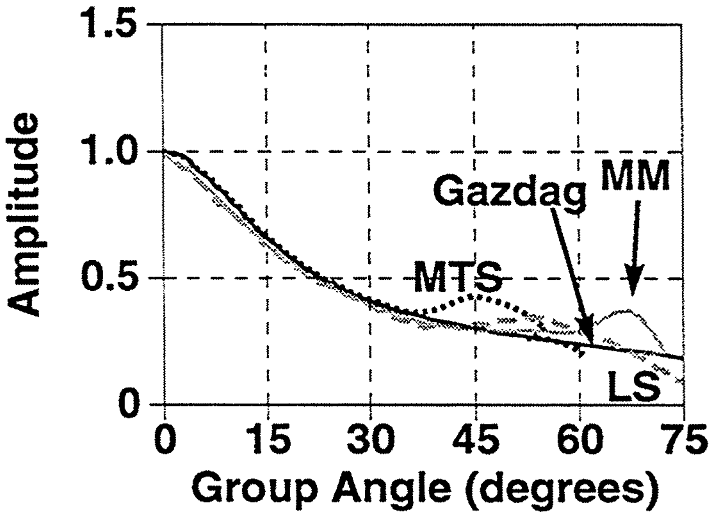

FIG. 3.27. Amplitude as a function of propagation angle for the P mode, for the same VTI medium as in Figure 2.10. Black solid line: Gazdag amplitudes. Black dotted line: MTS amplitudes. Gray dotted line: LS amplitudes. Gray solid line: minimax (MM) amplitudes.

Figure 3.27 reflects the main characteristics of the explicit methods implemented and as seen in previous curves. In the MTS method, the Taylor expansion of the filter is made around vertical propagation so the error (with respect to the DEO) for low propagation angles is small; however, this error increases quickly with propagation angle. In the minimax and LS methods, the amplitude errors for low propagation angles are greater than those for the MTS method, however these errors do not increase quickly as in the MTS method for large propagation angles; they remain relatively small for a wider range of propagation angles.

We saw in Sections 3.5 and 3.6 that the amplitude and phase errors of explicit filters do not change much with normalized frequency. Here, as a rough approximation, I will use the amplitude and phase errors of one explicit filter calculated for a single normalized frequency to explain the amplitude distribution observed in Figure 3.27. Thus, Figures 3.28 and 3.29 show amplitude and phase errors in the propagation region for filters used in Figure 3.27 with a normalized frequency of 0.25 cycles, and calculated using the MTS, LS, and minimax (MM) methods. For angles less than about 30 degrees, the amplitude and phase errors for the MTS method are very small in relation to the errors for the LS and minimax methods. In both figures, MTS errors are in the order of 10^{-5} for angles less than 30 degrees. Beyond about 40 degrees, however, MTS errors grow quickly and become larger than the LS and minimax errors. The LS and minimax errors also grow quickly close to the maximum design angle of the filter ($\theta_{max} = 60$ degrees).

Although Figures 3.28 and 3.29 show amplitude and phase errors just for a single

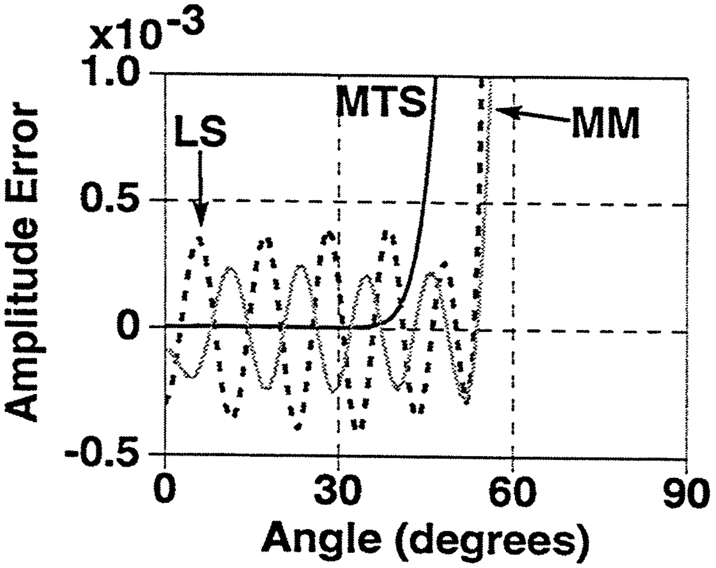

FIG. 3.28. Amplitude error for filters with a normalized frequency of 0.25 cycles used in Figure 3.27. Black solid line: MTS error. Black dotted line: LS error. Gray solid line: minimax (MM) error.

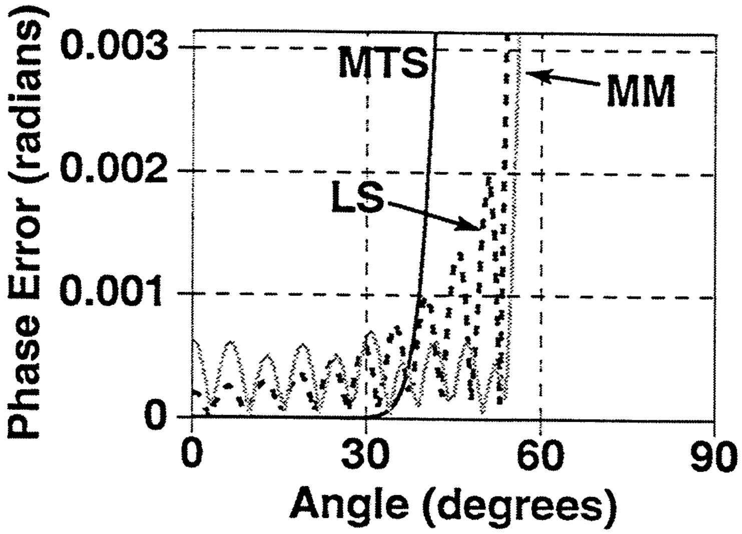

FIG. 3.29. Phase error for the same filters used in Figure 3.28.

filter, the behavior for filters with other normalized frequencies is similar, so Figures 3.28 and 3.29 help us to understand the amplitude distribution in Figure 3.27. MTS amplitude and phase errors for low propagation angles are so small, that MTS amplitudes basically match perfectly Gazdag amplitudes for group angles of less than about 40 degrees. In contrast, LS and minimax amplitude errors are on the order of 5.10^{-4} for phase angles of less than θ_{max}= 60 degrees. If we take this error as an average error for all the frequencies, the total amplitude error after 100-steps of depth-extrapolation would be $(1 \pm 5.10^{-4})^{100} \approx \pm 5$ percent of amplitude error, and 65 percent after 1000 steps. The main advantage of the LS and minimax methods over the MTS method, is that they maintain this small amplitude error for a wide range of propagation angles (close to θ_{max}).

These results suggest that in order to best preserve amplitudes, it would be desirable to apply MTS filters in areas with low dips. However, in areas with larger dips, the LS and minimax methods can be applied to better recover the shape of the reflectors. I must also point out that according with Soubaras (1992), the amplitude and phase errors in isotropic filters designed by the minimax and LS methods, can be reduced if we reduce the maximum design angle θ_{max}. The same statement can be applied to filters in TI media. Figure 3.30 shows amplitude and phase errors for the same MTS and minimax filters in Figures 3.28 and 3.29, but in this case, the maximum design angle in the minimax method was reduced from 60 to 40 degrees. The minimax errors in the passband in Figure 3.30 are about 10 times smaller than those in Figures 3.28 and 3.29. The reduction in the maximum design angle from 60 to 40 degrees, has reduced about 10 times the amplitude and phase errors for propagation angles less than 30 degrees. However, as we see in Figure 3.30, the errors in the minimax method are still higher than those in the MTS method even though the MTS method here gives better large-dip accuracy. Similarly (not shown here) the LS filter can be made more accurate in the passband by reducing θ_{max}, but not as accurate as the MTS method.

In all the results obtained in this thesis, the minimax and LS methods showed similar accuracy, but the minimax method was always less expensive than the LS method. Soubaras (1992) also obtained similar results for isotropic media. I therefore conclude that, from this point of view, we would always prefer to use the minimax method over the LS method.

3.8 Explicit filters for the *SH* wave mode

For elliptical anisotropy ($\epsilon = \delta$), the *P*-wave phase velocity is given by

$$V_{ph}^2(\theta) = V_{P0}^2(1 + 2\delta \sin^2 \theta). \tag{3.26}$$

This expression is exactly equivalent to the *SH* phase velocity [equation (2.13)] if we make $V_{p0} = V_{s0}$, and $\delta = \gamma$. Therefore, we can obtain *SH* wave filters by using the same computer programs used for *P* wave filters after making the above associations among Thomsen's parameters. Figure 3.31 shows a depth-migration impulse response for Taylor sandstone using the same MTS method for *P* waves but with $V_{p0} = V_{s0} = 1.829$ km/s, and $\epsilon = \delta = \gamma = 0.255$. This figure also shows that up to a maximum group angle

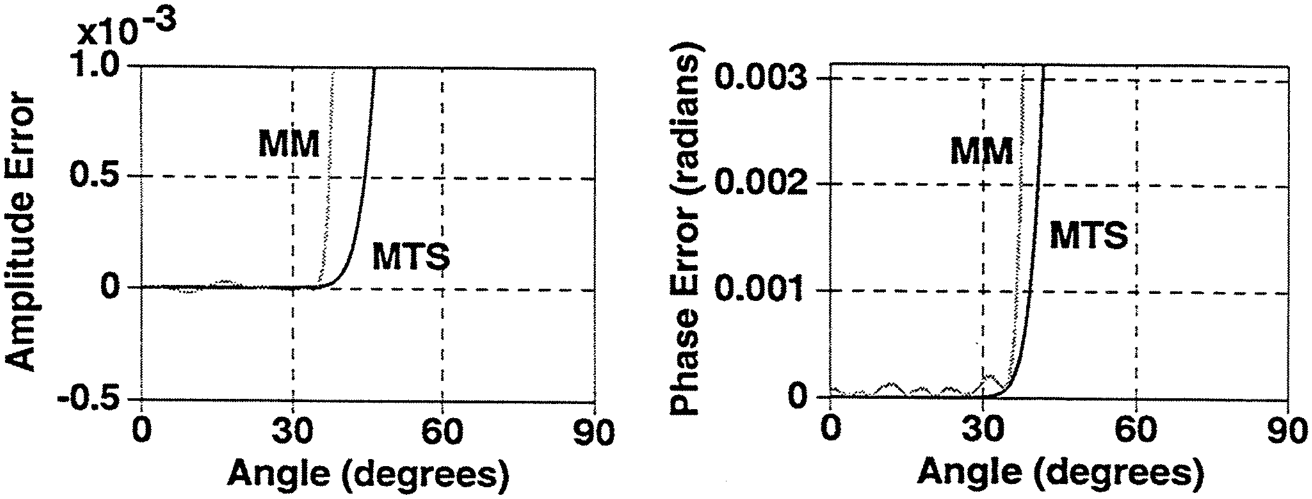

FIG. 3.30. Amplitude and phase errors for the same MTS and MM filters used in Figure 3.28, but for a MM filter designed with θ_{max}= 40 degrees.

of 60 degrees, the MTS impulse response matches the shape of the theoretical impulse response obtained using the exact *SH* velocity and group angle. Figure 3.32 shows the impulse response for the same medium as in Figure 3.31 but now using the minimax method for *SH* waves. Some 10 degrees of reflector dip has been gained through the use of the minimax method. A similar result (not shown here) is obtained by using the LS method.

3.9 TI media with a tilted axis of symmetry

In Chapter 2 we saw that the phase velocity at angle θ in a medium with a non-vertical axis of symmetry is equivalent to the phase velocity at angle $\theta - \phi$ in a medium with a vertical axis of symmetry, where ϕ is the angle of the tilted axis of symmetry with the vertical. I assume here that the tilted axis of symmetry is in the sagittal plane (plane of propagation) so the phase and group velocity vectors do not deviate from the incidence plane; therefore, a 2D treatment of the problem is possible. In azimuthally anisotropic media, out-of-plane propagation needs to be considered and the problem can be treated as a 2D problem only if the anisotropy is weak (Sena, 1991).

One might think, then, that the change in the argument of the phase velocity is the only modification required to calculate filters for non-vertical TI media. However, additional considerations are neccesary. The phase velocity $V_{ph}(\theta)$ is an even function of the propagation angle θ, so in VTI media, the horizontal wavenumber k_x is an odd function of θ ($k_x = \omega \sin\theta / V_{ph}(\theta)$). The DEO [equation (3.1)] is a function of k_x^2; therefore, the DEO is an even function of θ, and this symmetry of the DEO is reflected in the filter coefficients, which are also symmetrical with respect to θ. For TI media with a tilted axis

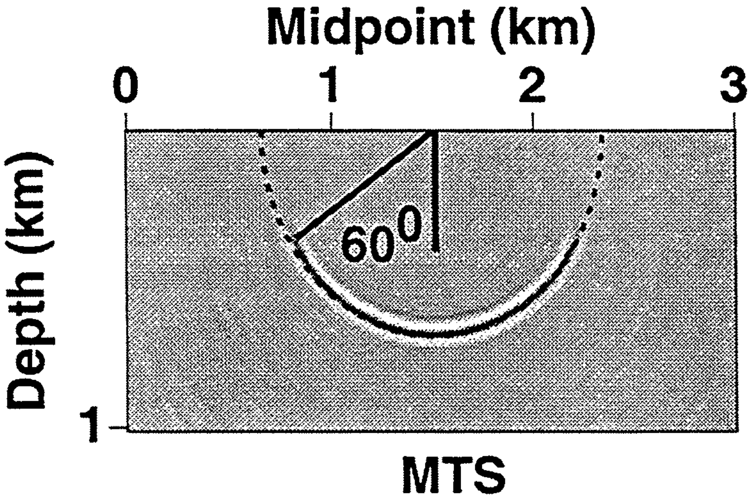

FIG. 3.31. Migration impulse responses via the MTS method for the *SH* propagation mode in Taylor sandstone.

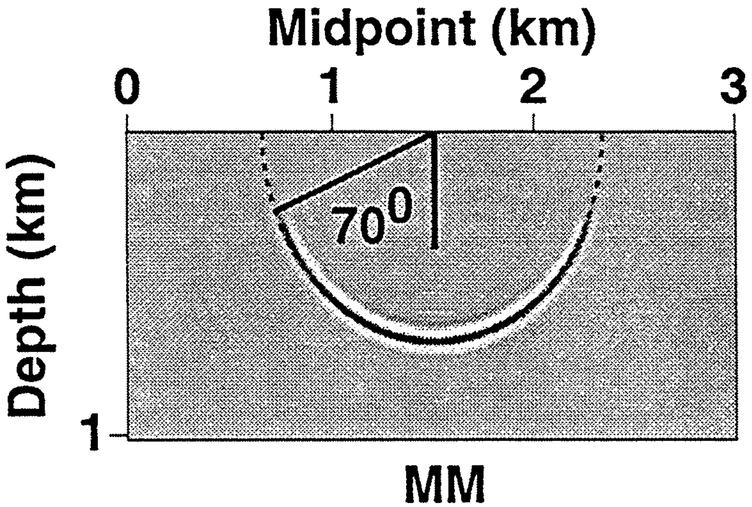

FIG. 3.32. Depth-migration impulse responses via the minimax (MM) method for the *SH* propagation mode in Taylor sandstone.

of symmetry, however, the horizontal wavenumber is given by $k_x = \omega \sin\theta / V_{ph}(\theta - \phi)$, which is no longer symmetrical with respect to θ $[k_x(\theta) \neq k_x(-\theta)]$. This result introduces loss of symmetry in the filter coefficients, so now, for the same filter length as in VTI media, twice the number of filter coefficients need to be calculated.

Doubling the number of filter coefficients increases the computer time in the filter calculation more than twice. For N=39 in the MTS method, for example, instead of solving a 20x20 linear system of equations, we need to solve a 40x40 system. Similar considerations can also be applied for the LS and minimax methods. However, the filter calculation for non-vertical axis of symmetry can be made independently for positive and negative values of the phase angle θ. In Appendix C, I show that the complex filter coefficients for a tilted axis of symmetry (t_n) can be expressed as

$$\begin{aligned} t_n &= \frac{1}{2}(p_n + n_n) + \frac{1}{2}H * (p_n - n_n) \quad n = 0, \ldots, N/2 \\ t_n &= \frac{1}{2}(p_n + n_n) + \frac{1}{2}H * (n_n - p_n) \quad n = -N/2, \ldots, -1 \end{aligned} \tag{3.27}$$

where p_n and n_n are symmetric complex filter coefficients, H is a discrete Hilbert transform operator, and * stands for convolution in the time domain. Rather than try to calculate a single filter with a large number of coefficients, I calculate two filters, each with half of the needed number of coefficients; one filter for positive (p_n) and another for negative (n_n) values of θ. The filters are calculated using a horizontal wavenumber k_x given by

$$k_x = \begin{cases} 2\omega \sin\theta / V_{ph}(\theta - \phi), & \text{if } \theta > 0, \ \theta = 0, \ldots \theta_{max} \\ -2\omega \sin\theta / V_{ph}(\theta + \phi), & \text{if } \theta < 0, \ \theta = -\theta_{max}, \ldots, 0, \end{cases} \tag{3.28}$$

where I have replaced $V_{ph}(-\theta - \phi)$ by $V_{ph}(\theta + \phi)$. With this approach, the computer time needed to calculate the explicit operators for non-vertical TI media is just twice the time needed for VTI media plus the time needed to calculate equation (3.27). The computer cost of equation (3.27) is small; it involves only $3N$ complex additions and the cost of two convolutions to calculate the Hilbert transform of the real and imaginary part of the difference $p_n - n_n$,

The computer time for the depth-migration process also increases for non-vertical TI media. In VTI media, the convolution process that does the depth-extrapolation from depth z to depth $z + \Delta z$ is defined (Holberg, 1988) as

$$\begin{aligned} P(\omega, x, z + \Delta z) = h_0(\omega) P(\omega, x, z) + \\ \sum_{l=1}^{(N-1)/2} h_l(\omega)[P(\omega, x + l\Delta x, z) + P(\omega, x - l\Delta x, z)], \end{aligned} \tag{3.29}$$

where P is the seismic wavefield, and $h_l(\omega)$ are the filter coefficients. The convolution process in equation (3.29) uses the symmetry of the filter coefficients when it multiplies $h_l(\omega)$ with the wavefield evaluated at positions $x + l\Delta x$ and $x - l\Delta x$. For non-vertical TI

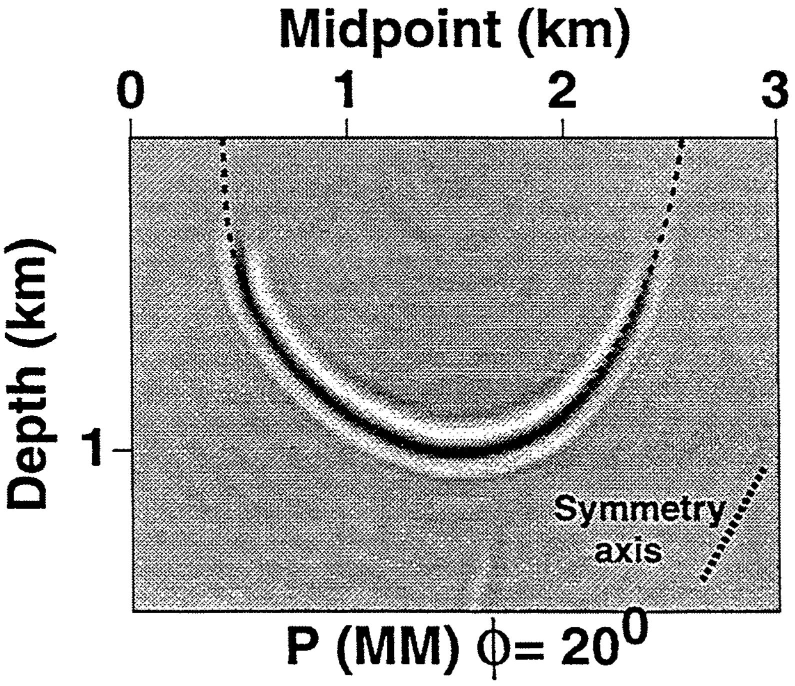

FIG. 3.33. Depth-migration impulse responses via the minimax (MM) method for the P propagation mode and for axis of symmetry tilted at 20 degrees from vertical. The dotted line represents the shape of the theoretical impulse response.

media, the symmetry in the filter coefficients is lost, and the convolution process becomes

$$P(\omega, x, z+\Delta z) = h_0(\omega)P(\omega, x, z) + \sum_{l=1}^{(N-1)/2} h_l(\omega)P(\omega, x+l\Delta x, z) + h_{-l}(\omega)P(\omega, x-l\Delta x, z), \tag{3.30}$$

where $h_l \neq h_{-l}$. The total cost in explicit depth extrapolation is proportional to the number of times that the convolution process in equations (3.29) or (3.30) has to be executed. This process must be executed for all frequencies, horizontal distances, and depths. From equation (3.29) we see that for a filter of N= 39 complex coefficients, the convolution process for VTI media consists of 20 complex multiplies and 38 complex adds. Comparing equations (3.29) and (3.30), we see that the increase in the cost of the convolution process for a tilted axis of symmetry is just the addition of $(N-1)/2$ complex multiplications; the number of complex adds is the same for both process. However, on the IBM RS/6000 workstation the loop that executes equations (3.29) or (3.30) can be highly optimized, so the final cost of the convolution process for non-vertical TI media is just 24-percent higher than the cost for VTI media for a filter of N=39 coefficients.

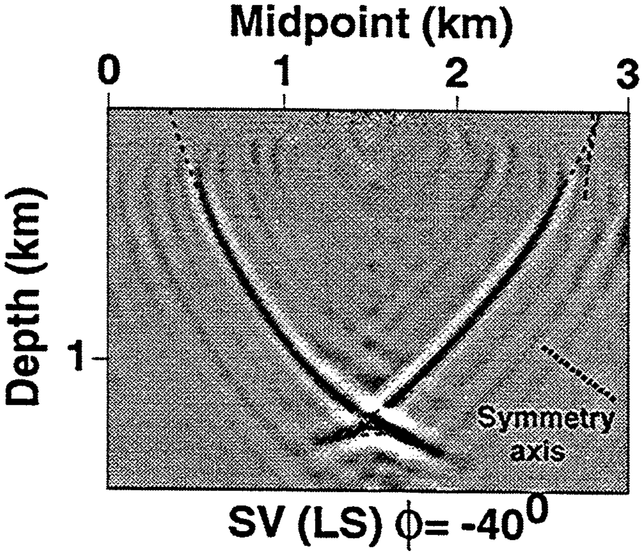

FIG. 3.34. Depth-migration impulse response via the LS method for the SV propagation mode and for a tilted axis of symmetry of -40 degrees.

Figure 3.33 shows a migration impulse response for the P mode using the minimax method. The TI medium has Thomsen parameters V_{p0}= 2.0 km/s, V_{s0}= 1.0 km/s, ϵ= 0.1, δ= -0.1, and an angle of 20 degrees of the symmetry axis with the vertical. Again the minimax impulse response follows the shape of the theoretical impulse response (dotted line) for a wide range of propagation angles. In Chapter 4, I study the accuracy of the operators for non-vertical axis of symmetry. For the particular values of ϵ=0.1 and δ=-0.1 in Figure 3.33, the filter coefficients p_n and n_n of equation (3.27) were calculated using the same $\theta_{max} = 65$ degrees.

The CPU time to calculate the depth-migration section was 1.86 minutes. For the same medium, but with a vertical axis of symmetry, the CPU time to calculate a similar depth migrated section was 1.45 minutes; thus, here, 28 percent more CPU time is required to calculate the migrated section for non-vertical axis of symmetry.

Figure 3.34 shows an impulse response, now using the LS method for the SV mode, for a TI medium with Thomsen parameters V_{p0}= 4.0 km/s, V_{s0}= 2.0 km/s, ϵ= 0.4, δ= 0.0, and for an angle of -40 degrees of the symmetry axis with the vertical. Figure 3.34 also shows that the calculated impulse response fits well the shape of the theoretical response (dotted line). The CPU times required to calculate the depth-migration section are the same as for the example in Figure 3.33. For comparison, Figure 3.35 shows the shapes of theoretical impulse responses for the same medium as in Figure 3.33, but for symmetry axis that is vertical and symmetry axis tilted at -40 degrees.

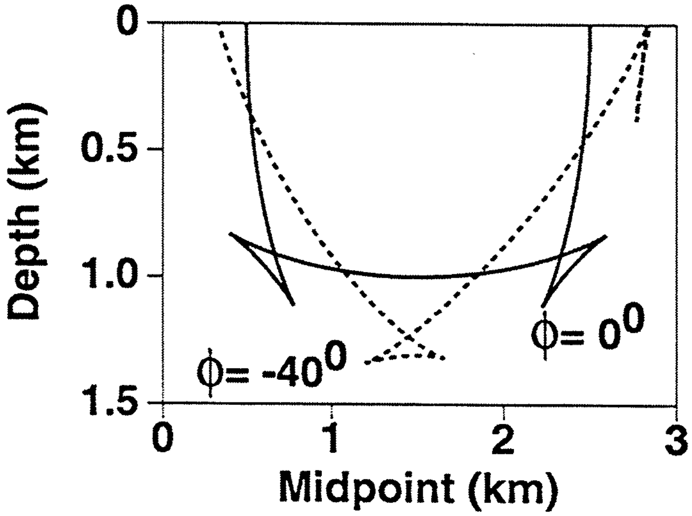

FIG. 3.35. Shapes of the theoretical *SV* depth migration impulse responses for the same TI medium as in Figure 3.24, but for a vertical and -40 degrees axis of symmetry.

Chapter 4

ACCURACY OF EXPLICIT DEPTH EXTRAPOLATION IN TI MEDIA

4.1 Introduction

In Chapter 3 we saw that for all the explicit methods developed, and for the TI media considered, the accuracy of the explicit depth-extrapolation process as applied to depth migration in TI media depends not only the propagation mode under consideration (*P* or *SV*), but also on the elastic properties of the medium.

Rather than study filter accuracy for specific media, here I examine the filter accuracy as a function of Thomsen's parameters. Existing laboratory and field data (Thomsen, 1986) indicate that many sedimentary rocks have weak to moderate anisotropy with $|\epsilon| \leq 0.3$, and $|\delta| \leq 0.2$. In addition, I also limit the variation of Thomsen's parameters V_{p0} and V_{s0} to an important range of practical applications, $0.3 \leq V_{s0}/V_{p0} \leq 0.7$. First, I study which of the Thomsen's parameters most influence the calculation of explicit operators for the *P* and *SV* propagation modes. As described in Chapter 3, the downward-extrapolation operator (DEO) in TI media is a function of the phase velocity $V_{ph}(\theta)$. Specifically, the dependence of the DEO on propagation angle is determined by the angular dependence of phase velocity $V_{ph}(\theta)$. Previous studies by Tsvankin (1995) and by Alkhalifah and Tsvankin (1994) have determined which anisotropy parameters control most the values of the phase and group velocity. In addition, Alkhalifah and Larner (1994) determined that ϵ and δ are the parameters that mainly control the migration error produced when isotropic migration algorithms are used to migrate data from anisotropic media. Here, I build on some of those results to study how the anisotropy influences the theoretical and computed migration impulse response for the *P* and *SV*-wave propagation modes in TI media.

After studying migration impulse responses for several choices of anisotropy values, I do tests on synthetic seismograms to show that for the *P* propagation mode, we need only calculate explicit operators for each pair of ϵ and δ values. Lateral and vertical changes in vertical *P*-wave velocity (V_{p0}) are handled by calculating tables of operators for different ratios of normalized frequency, $f\Delta x/V_{p0}$, just as is done for isotropic media. The vertical shear-wave velocity (V_{s0}) does not affect the phase-velocity itself and therefore does not have a significant influence on accuracy for typical values of ϵ and δ found in sedimentary basins. By comparing theoretical migration impulse responses for the *SV* mode, I show that to a good approximation, we need only compute explicit operators for each σ value in the *SV* mode, where $\sigma = (V_{p0}/V_{s0})^2(\epsilon - \delta)$ is a parameter introduced by Tsvankin and Thomsen (1994).

I use the least-squares method to calculate explicit operators for several values of ϵ and δ, and for the *P* mode. The minimax method (not shown here) would give comparable results. Somewhat surprisingly, I find that the accuracy of the operators in the P mode can actually surpass that for isotropic media, increasing with increasing value of δ, and decreasing for increasing value of ϵ. For the SV mode, I use the minimax method to calculate the explicit operators because it produces better impulse responses than does the least-squares method. The accuracy in the SV mode appears to be independent of σ, for typical values of σ.

To study the accuracy problem in isotropic media, I calculate explicit filters for the real and imaginary part of the DEO, but this time, as opposed to what was done in Chapter 3, I calculate the filters without amplitude constraints in the evanescent region. The idea is to use all the degrees of freedom in the filter in order to ensure the best accuracy obtainable in the propagation region. I find that the amplitude and phase errors in the imaginary-part filter dominate the amplitude and phase errors in the total filter. This behavior can be explained by using the convergence properties of Fourier series for the imaginary-part DEO. For TI media, I follow the same approach used for isotropic media, and study the properties of the imaginary-part DEO to explain the dependence of the accuracy of the filters on the values of ϵ and δ.

4.2 Migration and DEO dependence on Thomsen's parameters

For isotropic media, Thomsen's parameters ϵ and δ are zero, so from the equations derived in Chapter 2, the P and SV phase-velocities are independent of the propagation angle. Therefore, in isotropic media, we need only calculate enough explicit extrapolators to accommodate variations of velocity with vertical and horizontal position. As pointed out by Holberg (1988) and Hale (1991a), lateral velocity variations are handled by laterally variable extrapolators.

As we saw in Section 3.6.2, the operator calculation (for any method: MTS, LS, or minimax) is sufficiently computationally intensive that calculation of the operators during the extrapolation process would slow down the speed of the overall migration process excessively. Additionally, the operator calculated for any given normalized frequency is likely to be used many times, either within the migration process (due to the recursive character of the extrapolation) or in repeated applications of migration processing. Therefore, following Blacquiére et al. (1989), I calculate the operators in advance and store them in a table.

The number of operators required will depend on the range of velocity values and the number of frequencies. During the extrapolation process, the appropriate operator, based on the determined local value of wavenumber, is selected from the table and applied to the data. This procedure could lead to a large table of operators because many different wavenumbers can be required during the migration process. The main advantage of using a table of extrapolators, however, should be its limited size. We saw in Chapter 3 that for practical applications, about 1000 extrapolators might be needed, so the size of one of these tables for a symmetric filter of N=39 complex coefficients (of which only 20 are independent) will be about (1000 extrapolators)x(40 real numbers)x(4 bytes)=1.6 kbytes. The disadvantage of using such a table is that, for any local computation, the

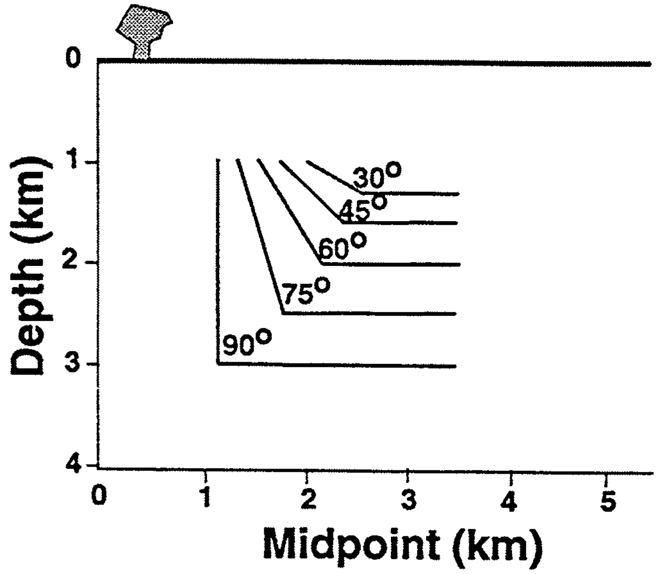

FIG. 4.1. Reflector model consisting of horizontal reflectors and segments with dip ranging from 30 to 90 degrees.

operator actually required is not likely to be present in the table. I address this problem by simple rounding, i.e., I select the operator from the table with normalized frequency nearest to the required one.

Thus, a table of extrapolators is calculated for a typical range of normalized frequencies $f\Delta x/V_{ph}$; then, during the depth-extrapolation process, from one depth to the next and for a constant frequency f, lateral velocity variations are handled by choosing different precalculated filters. For constant spatial sampling intervals Δx and Δz, a filter calculated to propagate the normalized frequency $f_1\Delta x/V_{1p}$ can also be used to propagate any normalized frequency $f_2\Delta x/V_{2p}$ such that $f_1/V_{1p} = f_2/V_{2p}$.

In TI media, the P and SV phase velocities and, therefore, the downward-continuation operator are functions of four variables (Thomsen's parameters). Therefore, it might seem that we need a different extrapolator table for each combination of the four Thomsen's parameters. However, as mentioned earlier, a look at the phase-velocity equation for the P mode [equations (2.11) and (2.14)] reveals that the dependence on vertical P-wave velocity for P data is just a multiplicative factor. Elsewhere in the equation, V_{p0} always appears in the combination V_{s0}/V_{p0}. For example, equation (2.14) depends just on the ratio V_{s0}/V_{p0}, so if we keep ϵ, δ, and the V_{s0}/V_{p0} ratio constant, the ratio of P phase velocities for two different values of V_{p0} (e.g., V^1_{p0}, V^2_{p0}) will be independent of propagation angle θ. That is,

$$\frac{V_{\mathrm{P}}(\theta; V^1_{p0}, \frac{V^1_{s0}}{V^1_{p0}}, \epsilon, \delta)}{V_{\mathrm{P}}(\theta; V^2_{p0}, \frac{V^1_{s0}}{V^1_{p0}}, \epsilon, \delta)} = \mathit{constant}. \tag{4.1}$$

A similar relation holds for the SV mode when two different values of V_{s0} are considered.

To test this relation for the P mode, I generated synthetic seismograms for a heterogeneous (V_{p0} variations only; ϵ, δ, and V_{s0}/V_{p0} are independent of position) transversely isotropic medium with a vertical axis of symmetry (VTI). Figure 4.1 shows a model containing horizontal reflectors and segments with dip ranging from 30 to 90 degrees. The medium has the elastic properties of Mesaverde clayshale (Thomsen, 1986), with a P-wave vertical velocity $V_{p0}(x,z) = 3.794 + 0.5x + 0.5z$ km/s, where x and z are in km. Figure 4.2a shows the zero-offset P-wave section corresponding to this model and calculated using a ray-tracing program for TI media (Alkhalifah, 1995b). This Kirchoff-based algorithm does not yield true amplitudes of elastic wavefields, but does yield accurate reflection-time information. Figure 4.2b shows the depth migration obtained using Hale's (1991a) $w - x$ depth-migration program, with VTI depth extrapolators calculated using the LS approach for a range of normalized frequencies ($f\Delta x/V_{p0}$) from 0 to 0.5 cycles. During the calculation of the operators I assume constant V_{p0}= 3.794 km/s, so the changes in normalized frequency where just due to changes in f. The maximum design angle in the LS method was 60 degrees; therefore, only reflectors with dip up to 60 degrees are recovered. The 75-degree reflector is attenuated and misplaced due to the amplitude and phase errors of the filter for dip greater than 60 degrees, and the 90-degree reflector is completely lost.

The results in Figure 4.2b show that even when V_{p0} changes with vertical and horizontal position, depth extrapolators calculated for constant V_{p0}, but for different values of f, can adequately handle these velocity variations. That is, the depth extrapolators all have the same θ dependence. For the depth migration, Figure 4.2b, 501 common midpoints, 301 time samples, and 401 depth extrapolation steps were used. The total CPU time on the IBM RS/6000 Model 530 workstation was 20.5 minutes, the same as for an isotropic migration for a medium with comparable heterogeneity. For comparison, the CPU time taken for the same depth-migration calculation but using a Gaussian-beam algorithm (Alkhalifah, 1995a) was 28.5 minutes.

Now, let's consider the dependence of migration results for the P mode on V_{s0}/V_{p0}. As suggested by Tsvankin (1995), the ratio of vertical velocities , V_{s0}/V_{p0}, does not have a significant influence on the P-mode phase velocity, for typical values of ϵ and δ found in sedimentary basins ($0 \leq \epsilon \leq 0.3$, $-0.2 \leq \delta \leq 0.2$). If the ratio V_{s0}/V_{p0} has little influence on the P-wave phase-velocity, then this ratio should also have little influence on the group velocity and group angle, and therefore, on the migration impulse response given by equation (2.21). Figure 4.3 shows impulse responses calculated using the theoretical behavior of group velocity as a function of ray angle for a medium with ϵ=0.3 and δ=-0.2, and for ratios V_{s0}/V_{p0} of 0.3, 0.5, and 0.7 (a wide range). All the impulse responses overlap to such an extent that it is hard to distinguish them.

The same reasoning may be applied to study the influence of the ratio V_{s0}/V_{p0} on depth migration via explicit filtering. As a test, I calculated a zero-offset section (Figure 4.4a) using the same ray-tracing program used to generate Figure 4.2a, corresponding to the model of Figure 4.1, but now using constant values for the four parameters: $V_{p0}(x,z)$ = 3.0 km/s, V_{s0}/V_{p0} = 0.5, ϵ =0.0, and δ =-0.2. Because the medium is

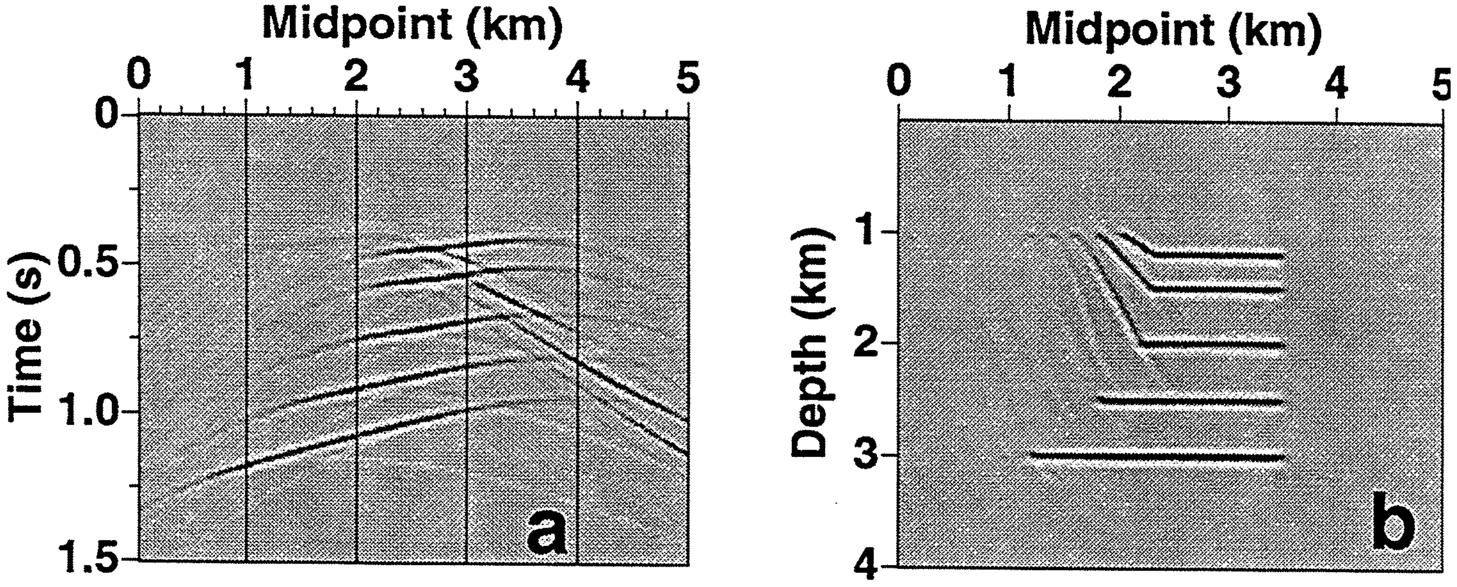

FIG. 4.2. Zero-offset synthetic section (left), for a model with the anisotropic properties of Mesaverde clayshale, corresponding to the reflector model in Figure 4.1 and vertical velocity $V_{p0}(x,z) = 3.794+ 0.5x+ 0.5z$ km/s. Depth migration (right) obtained using LS extrapolators.

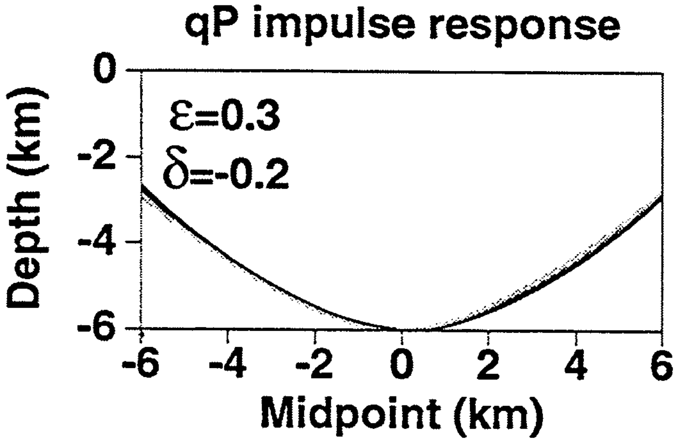

FIG. 4.3. P-wave migration impulse responses for a constant value of $V_{p0} = 3$ km/s, $\epsilon = 0.3$, $\delta = -0.2$, and for ratios $V_{s0}/V_{p0} = 0.3$, 0.5, and 0.7.

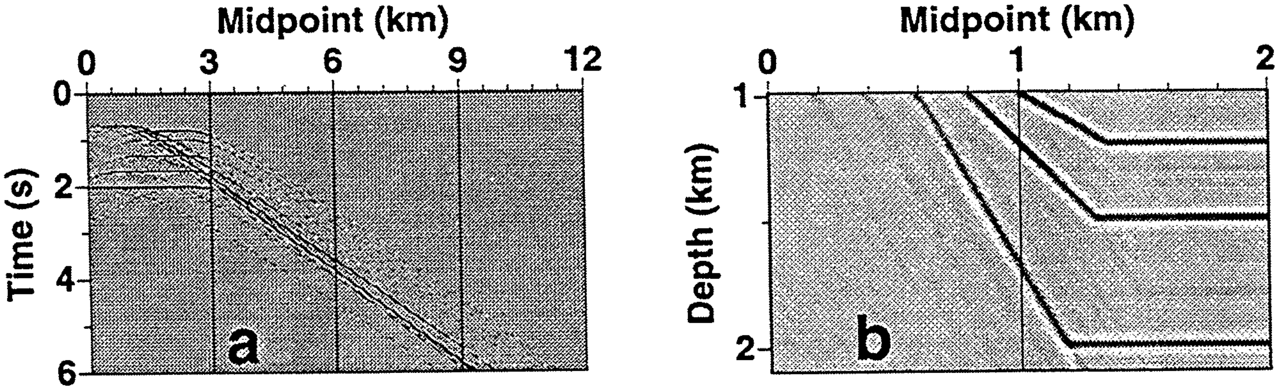

FIG. 4.4. Zero-offset synthetic section (left), for a homogenous model with $V_{p0} = 3$ km/s, $V_{s0} = 1.5$ km/s, $\epsilon = 0.0$, and $\delta = 0.2$, corresponding to the reflector model in Figure 4.1. Detail of depth-migration (right) obtained using minimax explicit filters with the correct Thomsen's parameters.

homogeneous, only the reflectors with relatively small dip (up to 60 degrees) can be recorded in the zero-offset section for reasonable values of midpoint distance and two-way time. Figure 4.4b shows the depth-migration results using minimax explicit filters with $\theta_{max} = 65$ degrees and with the correct ratio V_{s0}/V_{p0}=0.5. For comparison, Figures 4.5a and 4.5b show depth migration results when we use the correct vertical velocity $V_{p0} = 3.0$ km/s, but with erroneous ratios V_{s0}/V_{p0}=0.3 and 0.7, respectively. All the minimax filters in Figures 4.4b and 4.5 were calculated using the same $\theta_{max} = 65$ degrees, so differences in the results can be related to just the choice of V_{s0}/V_{p0} ratio. From Figure 4.5, we see that the use of the wrong V_{s0}/V_{p0} ratio has not produced any significant changes in the depth-migrated sections.

Similar tests done for different values of ϵ and δ, showed the strongest influence of the ratio V_{s0}/V_{p0} was observed for $\epsilon = 0.3$ and negative values of δ. As we will see later in this chapter, however, the accuracy of explicit filters calculated for $\epsilon = 0.3$ is so low that the filters would cause severe attenuation of the 60-degree reflector. To study the influence of the ratio V_{s0}/V_{p0} for ϵ=0.3 and $\delta \leq 0$, I used a Gaussian-beam migration algorithm because it has no dip limitations for homogeneous media. First, I calculated a zero-offset section (not shown here) using the same ray-tracing program as for Figures 4.2a and 4.4a, and the same V_{p0} and V_{s0} values as in Figure 4.4a, but with ϵ=0.3 and δ=-0.2. Figures 4.6a and 4.6b show the depth-migration results using a Gaussian-beam migration algorithm (Alkhalifah, 1995a) when we use the correct vertical velocity $V_{p0} = 3.0$ km/s, but with erroneous ratios V_{s0}/V_{p0}=0.3 and 0.7, respectively. In Figure 4.6, we see that the use of the wrong V_{s0}/V_{p0} ratio produces lateral mispositioning of the reflectors dipping at 45 and 60 degrees. However, the position errors even for this worst case of ϵ=0.3 and $\delta \leq 0$ are still relatively small. The errors in lateral position are approximately only ($\Delta y/y \simeq 100$ m/12000 m) 0.8 percent of the total migration distance,

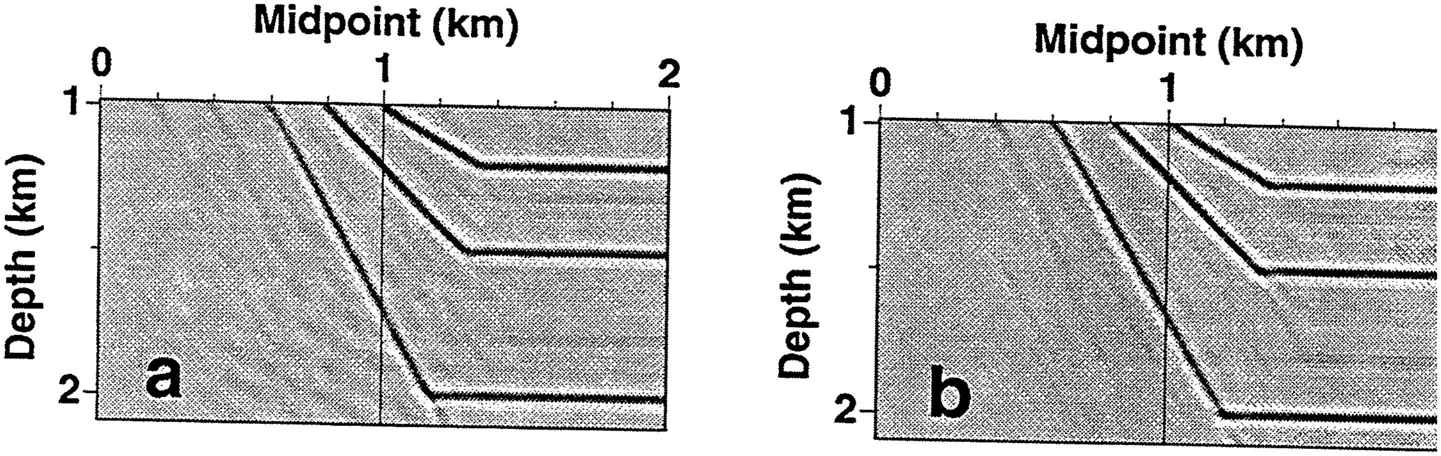

FIG. 4.5. Depth migration of synthetic section in Figure 4.4a obtained using minimax explicit filters with the same V_{p0}, ϵ, and δ as in Figure 4.4b, but with $V_{s0}/V_{p0} = 0.3$ (right), and $V_{s0}/V_{p0} = 0.7$ (left).

corresponding to an equivalent error in migration velocity $(\Delta v/v \simeq \frac{1}{2}\Delta y/y)$of only 0.4 percent. Clearly the migration is not sensitive to the velocity ratio V_{s0}/V_{p0}. For the special case of elliptical media (ϵ=δ), as shown by Thomsen (1986), V_{s0} has no influence on the P phase-velocity.

In contrast to the behavior of the P mode, for the SV mode the theoretical impulse response of migration *is* influenced by changes in V_{p0}, a phenomenon not seen in isotropic media. Tsvankin and Thomsen (1994) have shown that in the weak-anisotropy approximation, the SV phase-velocity depends on a particular combination of V_{p0}, V_{s0}, ϵ, and δ given by the parameter $\sigma = (V_{p0}/V_{s0})^2(\epsilon - \delta)$. For constant values of ϵ, δ, and V_{s0}, the value of σ changes with V_{p0} altering the SV phase-velocity. To study how the changes in phase-velocity alter the SV migration impulse response, Figure 4.7 shows impulse responses for media with $\epsilon = 0.0$, $\delta =$ -0.1, $V_{s0} = 1.0$ km/s, and for V_{s0}/V_{p0} ratios of 0.3, 0.5, and 0.7. The largest differences occur for intermediate propagation angles (near possible triplication points). For near-vertical and near-horizontal propagation angles, results are independent of V_{s0}/V_{p0}.

In order to test the last result, we generate synthetic seismograms for the homogeneous VTI medium of Figure 4.8a containing a horizontal reflector and a segment dipping 45 degrees. The medium has the elastic properties of the shale of Jones and Wang (1981) with V_{p0}= 3.048 km/s, V_{s0}=1.490 km/s, ϵ=0.255, and δ=-0.05. Figure 4.8b shows the zero-offset x−component generated by vertical-force exploding sources distributed along the reflector. The wavefield was calculated using an elastic anisotropic finite-difference program (Fei, 1993). This program calculates the complete elastic wavefield (multiples, converted waves, etc.), so the x-component section of Figure 4.8b shows not only P-waves generated by the vertical forces, but also SV-waves produced along the dipping reflector.

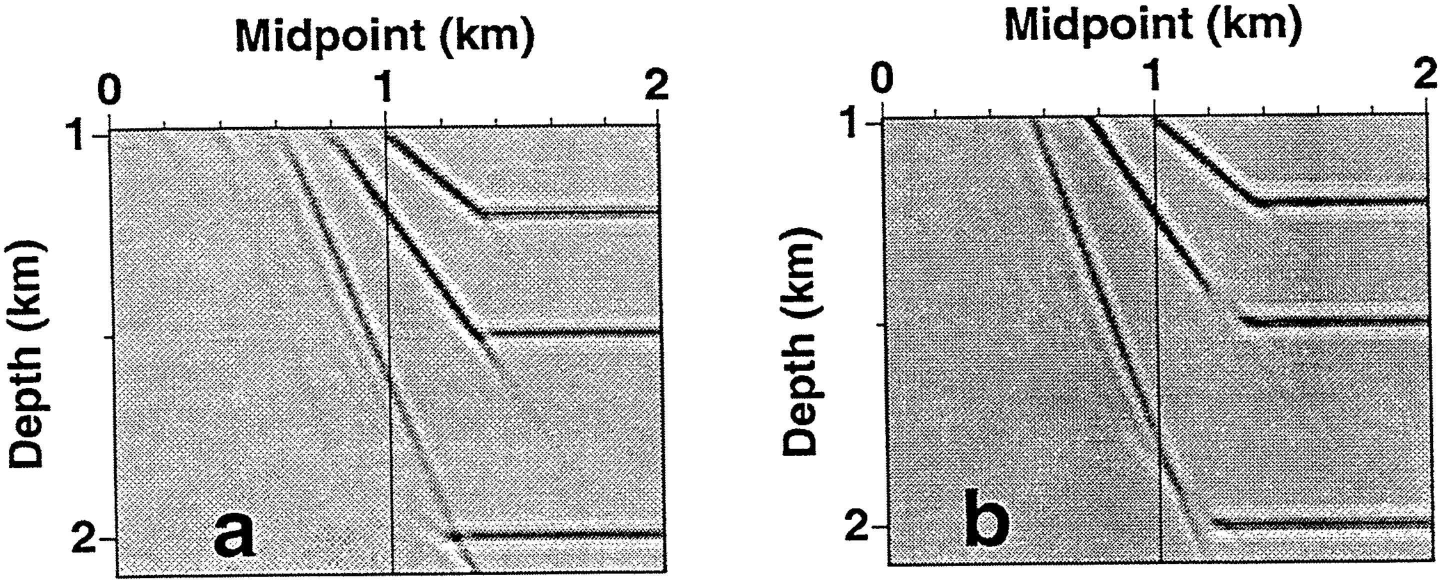

FIG. 4.6. Depth-migration of synthetic section in Figure 4.4a obtained using a Gaussiam-beam migration algorithm with the same V_{p0}, ϵ, and δ as in Figure 4.4, but with $V_{s0}/V_{p0} = 0.3$ (right), and $V_{s0}/V_{p0} = 0.7$ (left).

To obtain stability in the finite difference program, Fei (1993), I use a sampling interval of $\Delta t = 3.5$ ms and spatial sampling intervals of Δx=Δz=20 m to generate Figure 4.8b. Because the zero-offset section in Figure 4.8a has no high-frequency content (the source function is a Ricker wavelet with dominant frequency of 15 Hz), I resampled the original section to a new sampling interval of Δt=10 ms to reduce the cost of the migration process.

Figure 4.9a shows the depth-migration corresponding to the zero-offset section of Figure 4.8a obtained using SV-mode minimax explicit filters with the correct vertical velocity V_{s0}=1.490 km/s and the correct ratio V_{s0}/V_{p0}=0.49. For Figure 4.9b, an erroneous ratio V_{s0}/V_{p0}=0.7 was used. The dashed line shows the original model in depth. As I pointed out in Chapter 2, in the downward extrapolation of zero-offset data I assume that the recorded wavefield contains only a single propagation mode. P-wave events present in the (full elastic wavefield) zero-offset section of Figure 4.8a are propagated erroneously by the SV filters, so these events appear in erroneous positions and, thus, as noise in the final depth-migrated sections of Figures 4.9. To image these events properly, elastic anisotropic full-wave migration schemes are needed such as, for example, reverse-time migration (Fei, 1993). Alternatively, the P- and S-wavefields in the elastic-wave data need to be separated prior to applying the migration process.

Our main interest in Figure 4.9, however, is to see how the choice of the ratio V_{s0}/V_{p0}

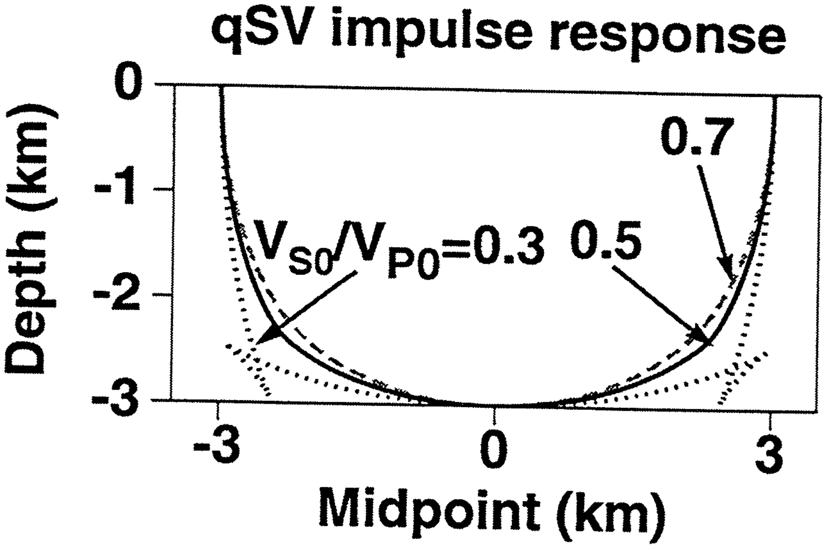

FIG. 4.7. Migration impulse responses for the *SV* mode and for constant $V_{s0} = 1.0$ km/s, but changing the velocity ratio V_{s0}/V_{p0} from 0.3 to 0.7. In all the curves, ϵ and δ are the same ($\epsilon = 0.0$, $\delta = -0.1$).

changes the depth-migrated section. Figure 4.9a shows a good fit between the position of the dipping reflector in the migrated section and the position in the original depth model, when the correct ratio V_{s0}/V_{p0} is used. Because each of the exploding sources used in the modeling program is a vertical force, no *SV* energy was generated for the flat reflectors; therefore, the flat reflectors cannot be recovered using just shear-wave data. On the other hand, Figure 4.9b shows that the use of the wrong V_{p0} value produces a lateral mispositioning of the dipping reflector. As pointed out above, this mispositioning would not appear in isotropic media, where migration of shear-wave data can be done independently of the value of the *P*-wave velocity.

The CPU time to calculate the depth-migration sections in Figure 4.9 via explicit filtering was 3.8 minutes. If we were to migrate the *z*- and *y*-components of the zero-offset section (shown later), the migration times for all the sections would be the same. Thus, the total CPU time to migrate the three-component section via explicit filtering would be 11.4 minutes. For comparison, the CPU time needed by the reverse-time migration algorithm (Fei, 1993) was 29 minutes. The comparison may seem unfair because in the depth-migration calculation via explicit filtering I increased the sampling interval from 3.5 to 10 ms. However, for the frequency content in these tests, the reverse-time migration algorithm still needs a small sampling interval of 3.5 ms in order to avoid numerical

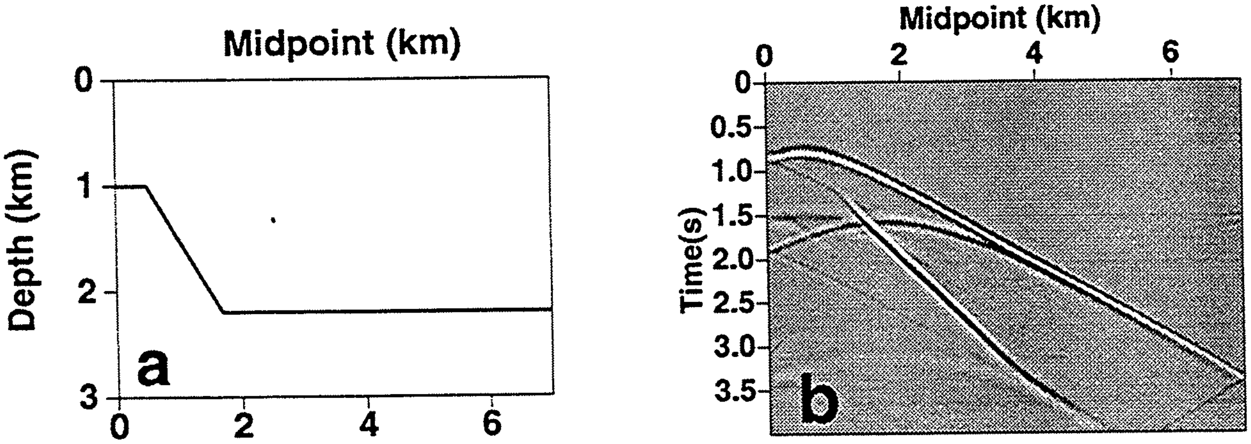

FIG. 4.8. Reflector model consisting of a horizontal reflector and a segment with a dip of 45 degrees (a). Zero-offset, x-component synthetic section for a homogenous model with Thomsen parameters corresponding to the Jones and Wang shale.

dispersion, whereas the explicit filtering approach does not. The cost of migration via explicit filtering and reverse-time migration would be about the same if the number of samples in time were equal in both process.

The final depth-migrated sections produced by reverse-time migration would not have the mode-conversion problems that we saw in Figure 4.9. However, today's conventional sequence of seismic data processing [velocity analysis and normal moveout (NMO) correction based on a particular propagation mode, followed by common midpoint (CMP) stacking] would typically yield a "zero-offset section" that emphasizes one mode, while attenuating others, such as seen in Figure 4.8b.

Let us now consider the influence of Thomsen parameters in the SV mode, but with the value of σ held constant. Figure 4.10 shows migration impulse responses for a constant value of $\sigma = 1.6$, and for $V_{s0} = 1.0$ km/s. The solid black curve corresponds to a $V_{p0} = 2$ km/s, $\epsilon = 0.2$, and $\delta = -0.2$. The dashed gray curve was calculated for $V_{p0} = 2.828$ km/s, $\epsilon = 0.0$, and $\delta = -0.2$; and, for the dotted black curve, $V_{p0} = 2.309$ km/s, $\epsilon = 0.15$, and $\delta = -0.15$. Even when all the ratios V_{p0}/V_{s0} are different, as are the values of ϵ and δ, the three curves are similar except in the region close to the caustic. Figure 4.11 shows a detail of depth migration obtained via SV minimax filters for the same zero-offset section of Figure 4.8a with the correct vertical velocity V_{s0}=1.490 km/s and for a fixed value of σ. V_{p0}=4.96 km/s, ϵ=0.1, and δ=-0.015 for the section in Figure 4.11a, and V_{p0}=2.98 km/s, ϵ=0.319, and δ=0.0 for the section in Figure 4.11b. Although all the ϵ, δ, and V_{p0} values are quite different in Figures 4.11a and 4.11b, use of the correct value of σ produces a good fit of the depth-migration results with the original depth model. In general, for migration of the SV mode for TI media, instead of using four Thomsen's parameters, it apparently suffices to use just σ, along with V_{s0}.

Returning again to the P-wave mode, recent studies [Alkhalifah and Larner (1994),

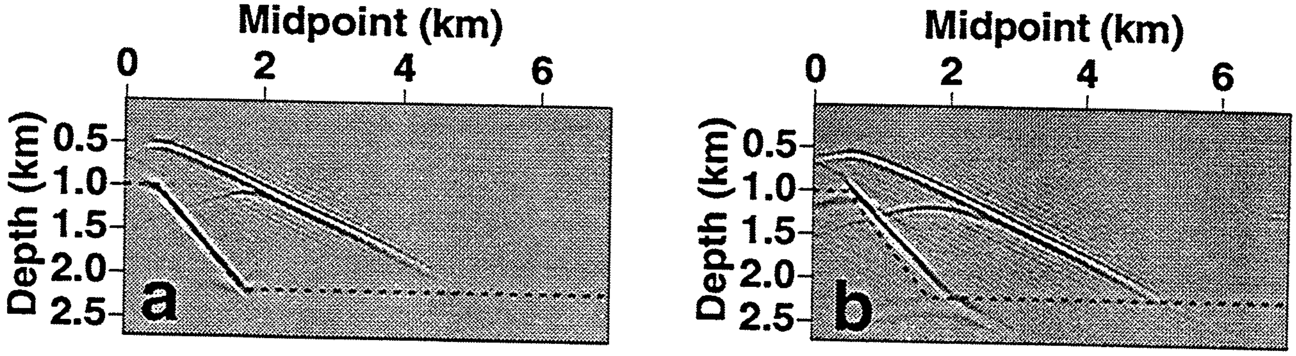

FIG. 4.9. Depth-migration of synthetic section in Figure 4.8b obtained using minimax SV filters with the same V_{s0}, ϵ, and δ in Figure 4.8b, but with the true V_{s0}/V_{p0}=0.49 (left), and V_{s0}/V_{p0}=0.7 (right).

Tsvankin (1994)], indicate that ϵ and δ control basically the P-wave propagation mode; therefore, we should also expect that these two parameters influence the migration results obtained via explicit filtering. Thomsen (1986) indicated that δ and ϵ control the near-vertical and near-horizontal propagation in the P-mode, respectively. Alkhalifah and Larner (1994) also showed that the migration error produced when anisotropy is ignored is controlled mainly by ϵ and δ. These results suggest that in order to reduce migration errors in explicit filtering, we must calculate extrapolation operators for each pair of different ϵ and δ values. If the area under study consists mainly of low-dipping reflectors (dip less than about 30 degrees), ϵ may not influence the migration results, so we could take, ϵ=0.0, for example, to calculate the filters. For intermediate and high propagation angles, knowledge of ϵ and δ would be essential to calculate accurate explicit filters.

Figure 4.12 shows the vertical (z-component) zero-offset section for the model of Figure 4.8a obtained using the same finite-differences modeling program used in Figure 4.8b. Figure 4.13 shows detail of depth migration obtained using P-wave minimax filters calculated for a VTI medium with the correct Thomsen parameters (a), and assuming an isotropic medium (b). Ignoring anisotropy has produced undermigration of the dipping reflector in Figure 4.13b.

The results in this section indicate that, for the P-mode, we must calculate explicit filters for each pair of ϵ and δ values. V_{s0} can be set as a constant during the calculation and V_{p0} variations are taken into account by calculating a table of operators for different values of normalized frequency $f\Delta x/V_{p0}$. On the other hand, explicit filters for the SV-mode must be calculated for each value of just one parameter, σ. Again, V_{s0} variations are considered by calculating a table of operators. Thus, during the filter calculation, only two parameters are needed for the P-mode and just one for the SV-mode. Nevertheless, to do the depth migration, the values of V_{p0} must be known for the P-mode in order to calculate the normalized frequency $f\Delta x/V_{p0}$, and thus, select the correct explicit operator to use at each depth step. A similar stament holds for the SV-mode, with V_{s0} being the

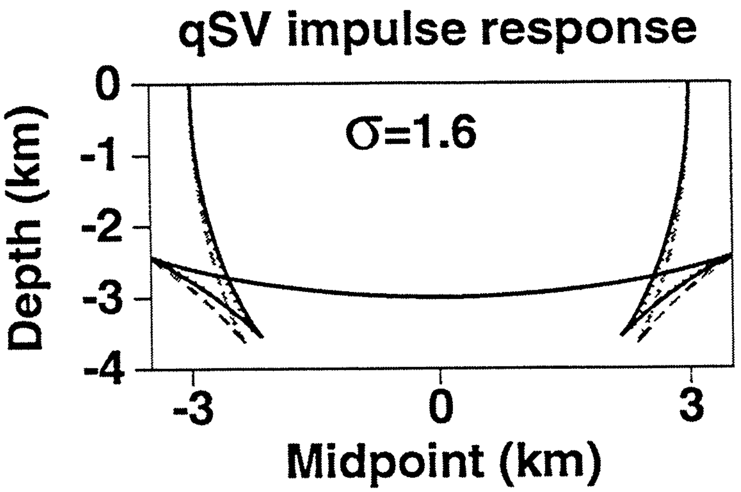

FIG. 4.10. Migration impulse responses for the SV mode for constant $\sigma = 1.6$, and for $V_{s0} = 1.0$ km/s.

value needed to calculate $f\Delta x/V_{s0}$.

Thomsen (1986) pointed out that δ values can be obtained from P-wave surface seismic velocity analysis and well information (well-logs, VSP, or check-shot) through the relation

$$V_{NMO} = V_{p0}\sqrt{1+2\delta}, \tag{4.2}$$

where V_{p0} is the vertical velocity obtained from the well information. Alkhalifah and Tsvankin (1994) showed that if the vertical velocity is known, ϵ and δ can be found by inverting two P-wave NMO velocities corresponding to a horizontal and a dipping reflector. For the SV-mode, Thomsen (1986) also find

$$V_{NMO} = V_{s0}\sqrt{1+2\sigma}. \tag{4.3}$$

Thus, we see from this equation that if V_{s0} information is available from a shear wave check-shot, or from a multicomponent VSP, the values of σ can be estimated.

4.3 Influence of anisotropy on filter accuracy

In Section 4.2 we studied the anisotropy parameters needed to calculate explicit operators for the P- and SV-mode. Also, in Chapter 3 we saw that the accuracy of the explicit filters changes from one TI medium to other, and also, for a given TI medium, the accuracy can change with the propagation mode. In this section, I study how the anisotropy, represented by Thomsen parameters, influences the accuracy of the calculated explicit filters. However, even in the isotropic case, Holberg (1888), Hale (1991a), and

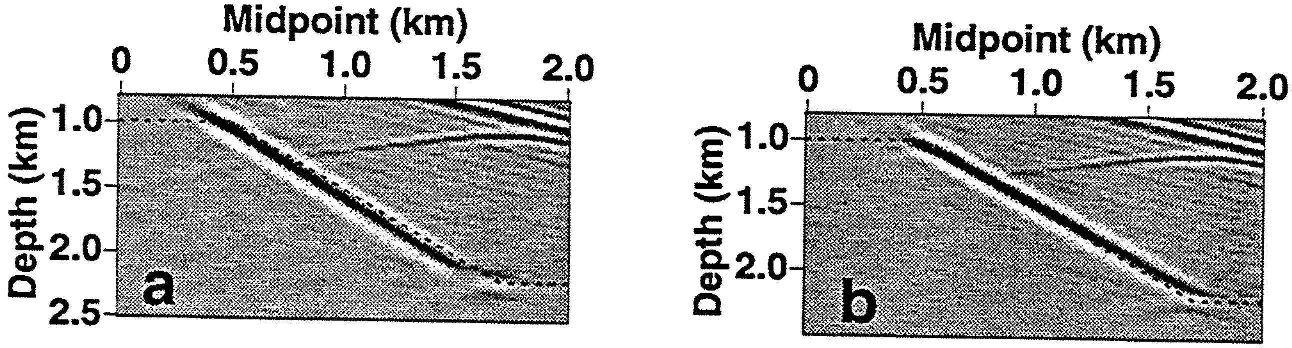

FIG. 4.11. Depth-migration of synthetic section in Figure 4.8b obtained using minimax SV filters with the same V_{s0}, ϵ, and δ in Figure 4.8b, but with the true V_{s0}/V_{p0}=0.49 (left), and V_{s0}/V_{p0}=0.7 (right).

Soubaras (1992) have shown that explicit filters have a limited accuracy, so I begin this section describing the accuracy problem for isotropic media in order to get the tools needed to describe the same problem in transversely isotropic media.

4.3.1 Filter accuracy in isotropic media

As Hale (1991a) has pointed out for isotropic media, stability is achieved only at the expense of accuracy, measurable in the ability to position steep reflectors correctly.

Let us consider first the accuracy problem in isotropic media. Figure 4.14 shows the theoretical (gray curve) and the actual (black curve) amplitude responses for an isotropic depth-extrapolation operator, as a function of normalized wavenumber (cycles). The minimax method was used to calculate the filter coefficients. The number of filter coefficients was $N = 39$, $\Delta z/\Delta x = 1$, the normalized frequency ($f\Delta x/V_{p0}$) was equal to 0.25 cycles, and the maximum design angle used in the minimax method was $\theta_{max} =$ 70 degrees. Figure 4.15 shows the amplitude (left) and phase (right) error of the filter in Figure 4.14, as a function of propagation angle. As pointed out by Hale (1991a), amplitude and phase errors less than 0.001 and $\pi/1000 \simeq 0.003$, respectively, guarantee the application of this filter for at least 1000 steps of downward-extrapolation without a significant accumulated error in amplitude or phase. If we were to increase θ_{max} beyond the 70 degrees used in Figure 4.14, the filter could become unstable, with amplitude values greater than unity in the evanescent region, or it could become inaccurate, with amplitude and phase errors in Figure 4.15 greater than 0.001 and $\pi/1000$, respectively.

Now, let us assume for a while that we do not care about stability in the evanescent region, so we can use all the degrees of freedom in the filter to get accuracy in the propagation region. Naturally, this kind of filter cannot be used in practice because it will amplify random noise components that may exist in the evanescent region. However, this test can help us determine the maximum angle that could possibly be accurately

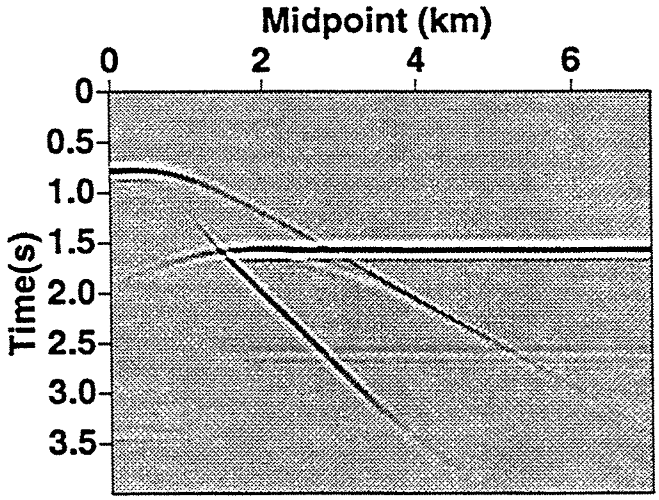

FIG. 4.12. Zero-offset z-component synthetic section for the homogeneous model of Figure 4.8a.

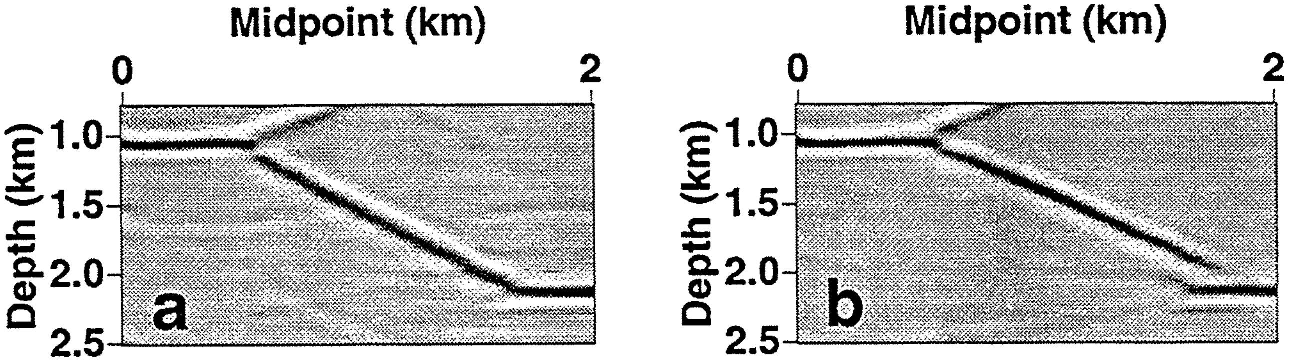

FIG. 4.13. Depth-migration of synthetic section in Figure 4.12 obtained using minimax P filters with the same values of V_{p0} and V_{s0} as in Figure 4.8b, but with the true ϵ=0.255 and δ=-0.05 (a), and with the wrong values of ϵ=0.0 and δ=0.0 (b).

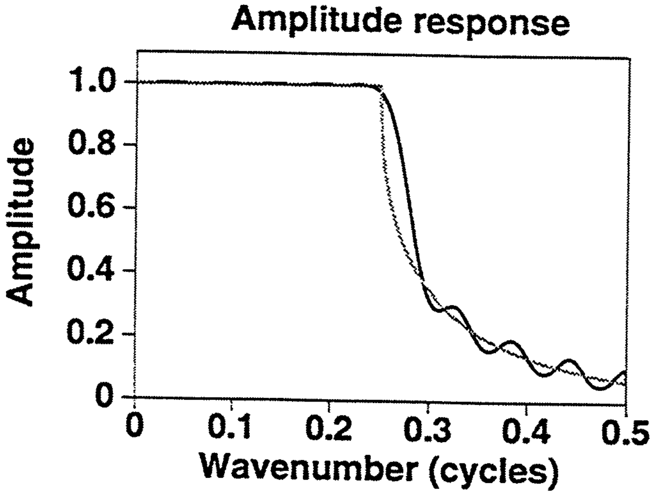

FIG. 4.14. Theoretical (gray curve) and actual (black curve) amplitude response for an isotropic DEO. The filter was calculated using the minimax method with $\theta_{max} = 70$ degrees. The boundary between the propagation and evanescent region is at 0.25 cycles.

propagated for a given number of filter coefficients. Figure 4.16 shows the theoretical (gray curve) and actual (black curve) amplitude response of the same filter as in Figure 4.14, but now using a maximum design angle $\theta_{max} = 85$ degrees, and without any amplitude constraints in the evanescent region (note the huge amplitude values for some wavenumbers greater than 0.25 cycles). Figure 4.17 shows the amplitude (left) and phase (right) error of the filter in Figure 4.16, but now as a function of propagation angle. Note that even when all the degrees of freedom in the filter are used to get accuracy in the propagation region, the amplitude and phase errors in Figure 4.17 are large relative to those of Figure 4.15 (because of the large value of θ_{max} used here). It seems that there are not enough degrees of freedom in a filter of $N = 39$ coefficients to propagate a maximum angle of 85 degrees, even when we have no amplitude constraints in the evanescent region.

In the analysis of Figure 4.14 through Figure 4.16, we studied the amplitude and phase response of the filters. The depth-extrapolation filters are actually composed of two filters; one filter propagates the real part of the DEO [equation (3.1)], and another propagates the imaginary part. Let us take a look at the amplitude error of the real- and imaginary-part filters of Figure 4.16. Figure 4.18 shows the amplitude error of the filters calculated to match the real (left) and imaginary (right) part of the downward-continuation operator in Figure 4.16. Interestingly, the amplitude error for the imaginary-part filter is about 20 times larger than that of the real-part filter. For practical purposes, therefore, all the amplitude error in Figure 4.17 is produced by the error in the imaginary part. Thus, we see from Figure 4.18 that, in reality, we have enough degrees of freedom to fit the real part of the operator. The fit to the imaginary part, however, is poor;

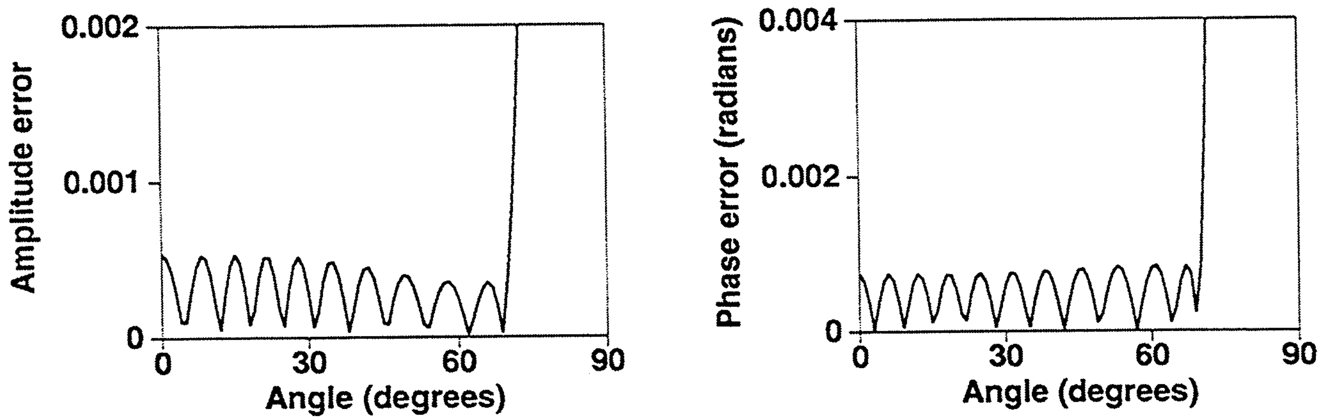

FIG. 4.15. Amplitude (left) and phase (right) error as a function of propagation angle for the filter in Figure 4.14.

the behavior of the imaginary-part operator is such that it cannot be well fit with a finite-length filter.

Calculating depth-extrapolation filters is basically equivalent to finding a convergent Fourier series expansion for the DEO (Holberg, 1988). Different treatments can be used to attenuate the evanescent energy and to improve the convergence of the Fourier series expansion (Holberg, 1988; Hale, 1991a), but, in general, the fit to the DEO in the propagation region is made by a Fourier series expansion. The convergence properties of a Fourier series expansion for any function depend on the degree of continuity of the function and its derivatives. Thus, roughly speaking, if the function and its first $p-1$ derivatives are bounded and continuous, the coefficients in the Fourier's series for the function will be less in absolute value than L/N^{p+1}, where L is some positive number independent of N, and N is the number of terms used in the expansion (Tolstov, 1976).

Figure 4.19 shows the theoretical amplitude response for the real (left) and imaginary (right) parts of the same theoretical operator as in Figure 4.16. In the propagation region (wavenumbers less than 0.25 cycles), both operators are continuous. Figure 4.20 shows the derivative of the real (left) and imaginary (right) parts of the DEO in Figure 4.19. The real-part derivative has a discontinuity at the threshold wavenumber that separates the propagation and evanescent regions, and is unbounded in the evanescent region ($\lim_{k \to 0.25^+} Re(k) = -\infty$). However, in the propagation region (wavenumbers between 0 and 0.25 cycles), the real-part derivative is continuous and bounded (at least, $p = 2$); therefore, the coefficients in the Fourier series for the real-part operator will be smaller in absolute value than L/N^3. For this analysis, we do not care so much about the convergence of the Fourier series in the evanescent region. For that region, we require only that amplitude values be less than unity. The imaginary-part derivative also has a discontinuity at the threshold wavenumber, but this time, the imaginary part derivative

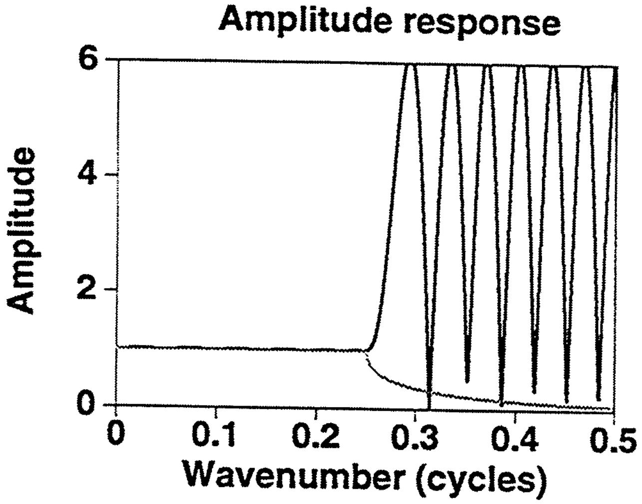

FIG. 4.16. Theoretical (gray curve) and filter (black curve) amplitude response for an isotropic DEO. The filter was calculated using the minimax method with θ_{max} = 85 degrees, and without amplitude constraints in the evanescent region.

is unbounded in the propagation region ($\lim_{k \to 0.25^-} Im(k) = -\infty$); therefore, the coefficients in the Fourier's series for the imaginary part operator will be less in absolute value than only L/N^2. This suggests an explanation for the different convergence properties and errors for the real- and imaginary-part filters.

4.3.2 Filter accuracy in TI media

For the P mode, we showed above that ϵ and δ mainly determine the behavior of the migration impulse responses. Figure 4.21 shows the 1000-step phase-error threshold for VTI media with ϵ = 0, δ = -0.2 (black curve); and ϵ = 0, δ = 0.2 (gray curve), using a 39-coefficient filter based on the LS method. The error thresholds are shown as a function of normalized frequency ($f\Delta x/V_{p0}$) and propagation angle. As before, the 1000-step phase-error contour corresponds to an error of $\pi/1000$ radians. Figure 4.21 exemplifies that for a given value of ϵ, the accuracy of the filters increases as the value of δ increases. Thus, the filters for ϵ = 0; δ = -0.2, and δ = 0.2, will propagate waves at about 65 and 75 degrees, respectively, with one-half cycle of phase error after 1000 steps of downward extrapolation. Almost 10 degrees of reflector dip has been gained in changing δ from -0.2 to 0.2. Interestingly, the result for δ = 0.2 is more accurate than that for isotropic media (ϵ = δ =0). A similar conclusion holds for accuracy based on amplitude.

Figure 4.22 again shows phase-error thresholds for VTI media by the LS method, but now using ϵ = 0.3, again with δ = -0.2 (black curve), and δ = 0.2 (gray curve). As I find for all choices of ϵ and δ, accuracy still increases for increasing values of δ; however,

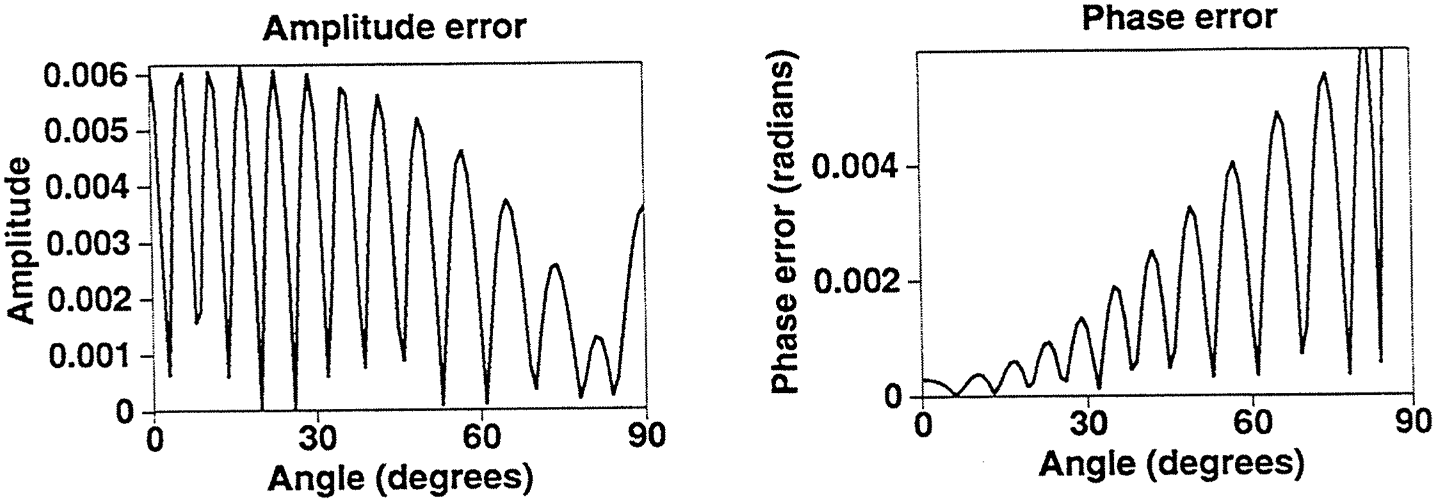

FIG. 4.17. Amplitude (left) and phase (right) error as a function of propagation angle for the filter in Figure 4.16.

comparing with the results in Figure 4.21, we see a decrease in accuracy for the larger value of ϵ. Figures 4.21 and 4.22 thus show that almost 10 degrees of reflector dip has been lost when we change ϵ from 0.0 to 0.3. The results in Figures 4.21 and 4.22 are representative of results of tests with all other choices for ϵ and δ over the practical ranges $0 \leq \epsilon \leq 0.3$ and $-0.2 \leq \delta \leq 0.2$.

Following the same reasoning employed in the isotropic case, we try to explain the results in Figures 4.21 and 4.22, by examining the behavior of the imaginary-part derivative of the depth-extrapolation operator for VTI media. Figure 4.23 shows this derivative, now as a function of dip angle in the propagation region, for values of ϵ = 0.0 (left) and ϵ = 0.3 (right). In both plots, the δ values used are δ = -0.2, 0.0, and 0.2. All these derivatives are unbounded (they go to minus infinity as the propagation angle approaches 90 degrees). Both plots show only the amplitude range -10 to 0. Figure 4.23 shows that for a constant value of ϵ, the rate of decay of these derivatives changes with the value of δ. Increasing the value of δ slows the decay rate; that is, the curves go to minus infinity more slowly than do those for lower values of δ. The slower the decay rate of the imaginary-part derivative, the smaller the magnitude of this derivative for high propagation angles; therefore, the larger the propagation angle that can be accurately handled with a finite-length filter.

Let's see if we can understand why accuracy has this dependence on the values of ϵ and δ. Figure 4.24 shows theoretical migration impulse responses for the P-mode and for constant values of V_{p0}=2.0 km/s and V_{s0}=1.0 km/s, for three different TI media, corresponding to cases where we expect relative poor, medium, and good accuracy for the explicit filters. Thus, the solid black curve corresponds to a medium with ϵ=0.3, and δ=-0.2 (poor relative accuracy); the gray curve corresponds to an isotropic medium

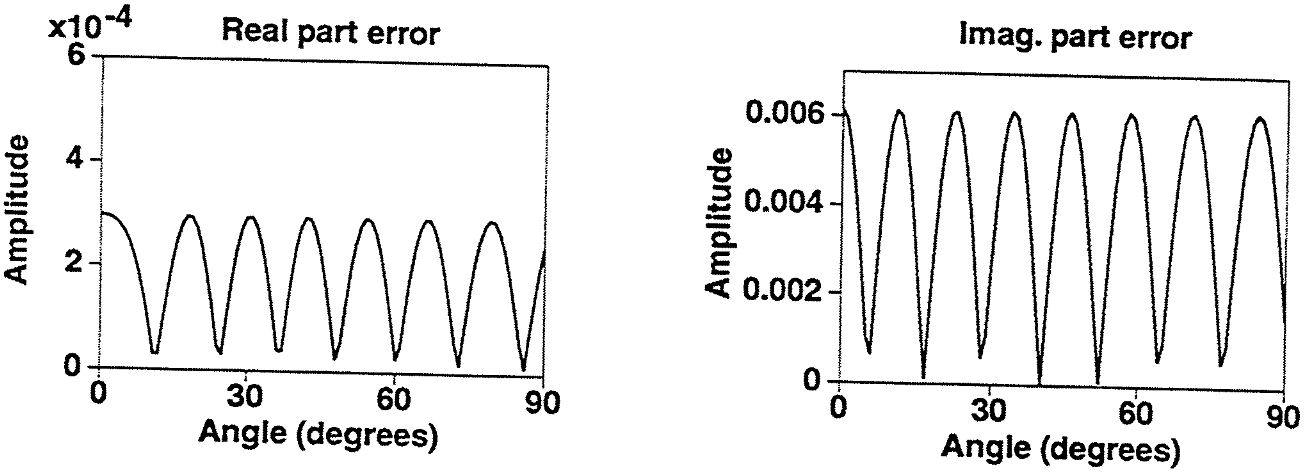

FIG. 4.18. Amplitude error for the real-part (left) and imaginary-part (right) filters in Figure 4.16.

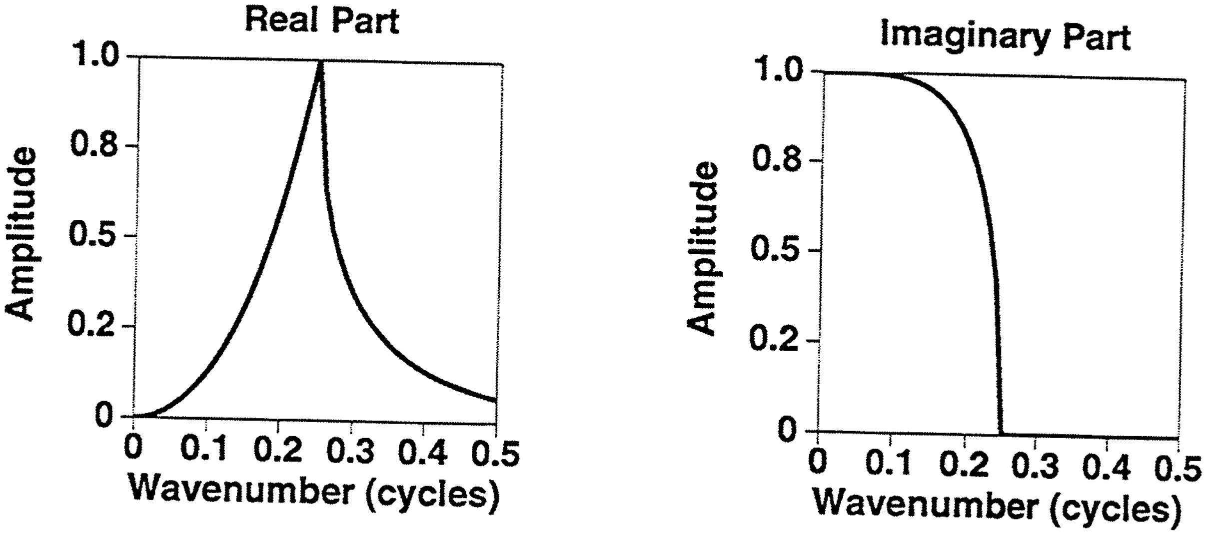

FIG. 4.19. Theoretical amplitude response of the real (left) and imaginary (right) part of an isotropic DEO.

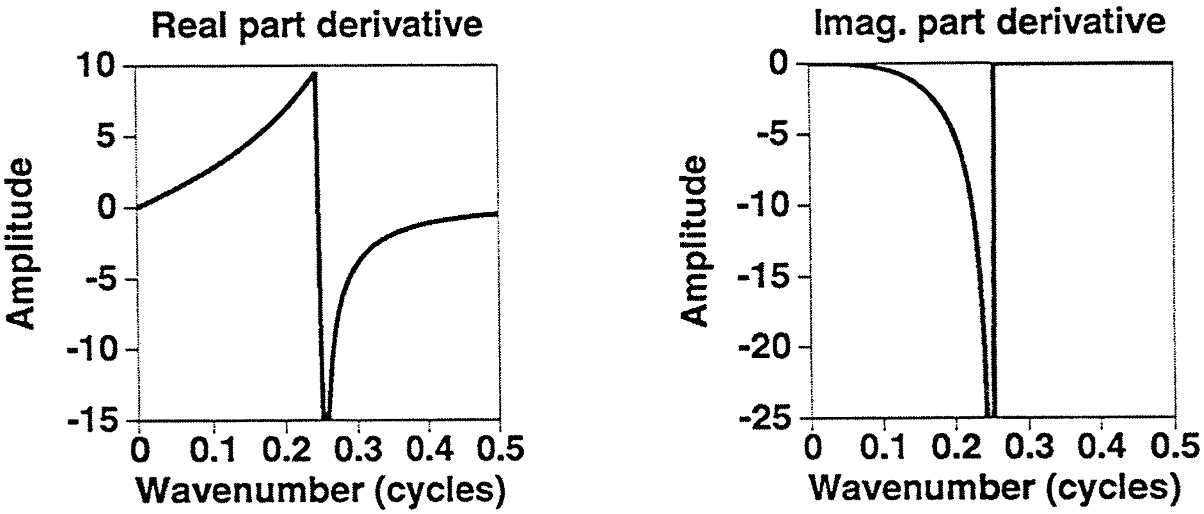

FIG. 4.20. Theoretical amplitude response for the derivative of the real (left) and imaginary (right) part of the same DEO as in Figure 4.19.

(ϵ=0.0 and δ=0.0) (medium relative accuracy); and the dashed curve corresponds to a medium with ϵ=0.0, and δ=0.3 (good relative accuracy). The solid black curve shows that the reflector dip increases more slowly with midpoint along the impulse response than do the dips for the other two curves.

A fixed group angle in Figure 4.24 corresponds to different maximum propagation dips in each one of these impulse responses. Figure 4.25 shows the maximum dips that can be seen in these three impulse responses for a group angle of 70 degrees. This choice of group angle is taken from the maximum angle that can be propagated using an isotropic filter of N=39 coefficients. I show only half of each of the impulse responses to emphasize the differences between the maximum dips propagated. The slopes of segments along the impulses responses in Figure 4.25 correspond to various dips in the subsurface. Therefore, in the poor-accuracy case (solid line), a relatively gentle dip (about 48 degrees) is seen in the impulse response at a group angle of 70 degrees. For isotropic media, the group angle is equal to the phase angle so the maximum dip obtained here is equal to 70 degrees. However, a steeper dip (about 76 degrees) is seen at group angle of 70 degrees in the curve for best accuracy (dashed curve).

For the SV mode, I use the minimax method to calculate depth-extrapolation filters. We saw in Chapter 3 that the minimax method can better handle triplications in the SV mode than does the least-squares method; both methods have similar accuracy otherwise. I also showed above that the σ parameter mainly determines the behavior of the SV migration impulse response. Figure 4.26 shows phase-error thresholds for VTI media with $\sigma = 1.6$ ($V_{p0} = 4.0$ km/s, $V_{s0} = 2.0$ km/s, $\epsilon = 0.3$, and $\delta = -0.1$), and $\sigma = 0.4$ ($V_{p0} = 4.0$ km/s, $V_{s0} = 2.0$ km/s, $\epsilon = 0.3$, and $\delta = 0.2$), using a 39-coefficient filter based on the

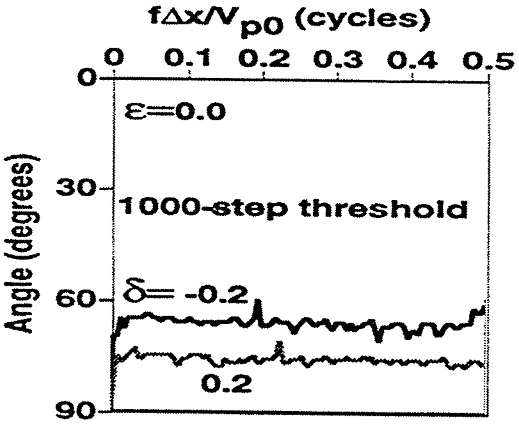

FIG. 4.21. Phase-error thresholds for the *P* mode in VTI media and for constant ϵ = 0.0, δ = -0.2 (black curve) and δ = 0.2 (gray curve). The phase-error contours correspond to $\pi/1000$ radians. After 1000 steps of depth-extrapolation, the accumulated phase error in the region beneath either contour will be one-half wavelength (π radians).

minimax method, and for a maximum design angle of 70 degrees. The two filters yield similar accuracy. A similar result (not shown here) was obtained for a filter calculated for σ = -0.2.

Figure 4.27 shows a detail of theoretical *SV* migration impulse responses for the same VTI media used in Figure 4.26 and for another VTI medium with σ=-0.2 (V_{p0}=2.86 km/s, V_{s0}=2.0 km/s, ϵ=0.1, δ=0.2). As opposed to the *P*-wave mode, where for a constant group angle the migration impulse responses showed different maximum dips, Figure 4.27 shows that for different values of σ, and for a constant group angle of 70 degrees, the impulse responses show basically the same maximum dips.

The maximum dip propagated with accuracy (about 70 degrees) by Holberg (1988) and Soubaras (1992) for isotropic media, combined with the results for the accuracy of the operators in the *P*-wave mode in Figures 4.21 through 4.23, and also the results of Figure 4.25, suggest that the depth-extrapolation filters can propagate with accuracy up to a maximum *group angle*. For the case of filters of length N=39 coefficients, that maximum group angle is about 70 degrees. For isotropic media, the group angle is equal to the phase angle, so the maximum dip that can be propagated with accuracy will also be 70 degrees. In TI media, the anisotropy in the media changes the relation between phase angle and group angle. Depending on the anisotropy values for a given medium, different phase angles can correspond to a group angle of 70 degrees. Therefore, details of the anisotropy will determine the maximum dip of structures in the subsurface that can be migrated with accuracy.

Let us try to test this result for *SV*-wave filters. Figures 4.26 and 4.27 suggest that explicit filters for the *SV*-wave mode can propagate up to a maximum dip angle of 70 degrees. In Figure 4.28, I show *SV* migration impulse responses for the same VTI media

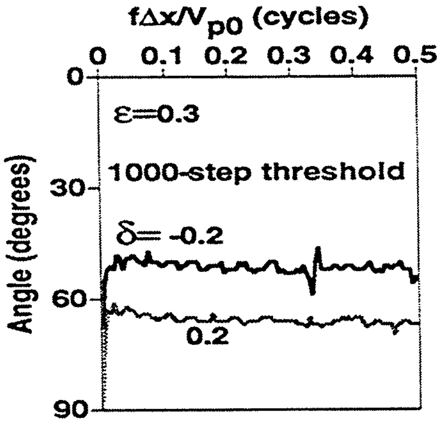

FIG. 4.22. Phase-error thresholds for the P mode in VTI media and for constant ϵ = 0.3, δ = -0.2 (black curve) and δ = 0.2 (gray curve). For the region beneath either contour level, the phase error would exceed a half-cycle after 1000-steps of downward continuation.

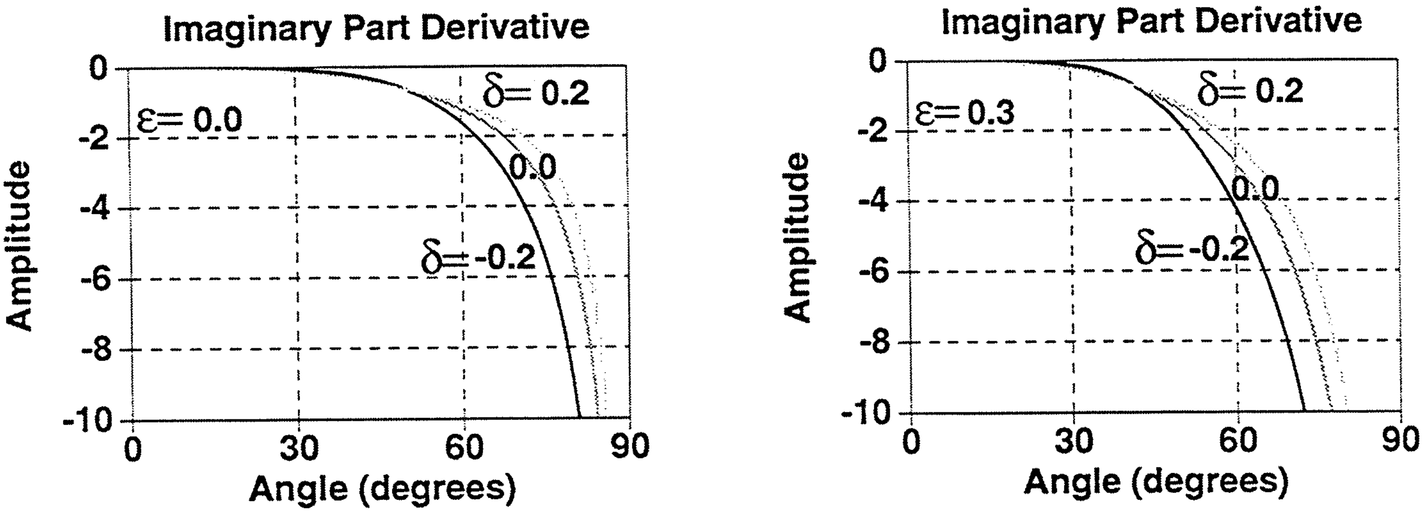

FIG. 4.23. Derivative of the imaginary part of the DEO for the P mode in VTI media and for different values of ϵ and δ.

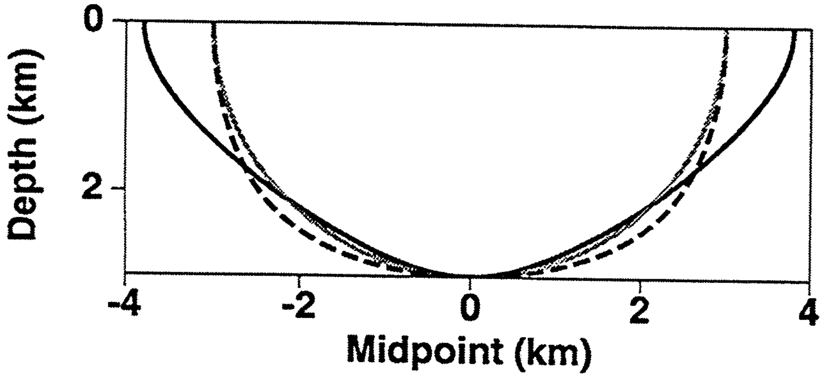

FIG. 4.24. P-wave migration impulse responses for constant values $V_{p0} = 2$ km/s, V_{s0}=1.0 km/s. Solid black curve, $\epsilon = 0.3$, $\delta = -0.2$. Gray curve, ϵ=0.0, δ=0.0. Dashed curve, ϵ=0.0, δ=0.3.

used in Figure 4.27, using explicit operators based on the minimax method. The depth-extrapolation filters calculated in Figure 4.26, and another filter calculated for $\sigma = -0.2$, were used to calculate the migration impulse responses of Figure 4.28. The same $\omega - x$ domain depth-migration program used by Hale (1991a) for isotropic media was used here to calculate these anisotropic migration impulse responses. All that has been changed in the migration program is the table of depth-extrapolators. Figure 4.28 confirms the result obtained in Figure 4.27. It shows that the three migration impulse responses have similar accuracy (up to about 70 degrees) even when the shapes of the impulse response differ considerably from one another.

Following the above reasoning, we can also estimate the accuracy of explicit filters in TI media with a non-vertical axis of symmetry. Figure 4.29 shows the same SV theoretical migration impulse responses shown in Figure 3.35, but now, the responses are displayed up to only a maximum group angle of 70 degrees. This group angle is the maximum group angle expected to propagate with accuracy using an explicit filter of N=39 coefficients. Therefore, Figure 4.29 shows the shape of the ideal impulse response that would be obtained using explicit filters of N=39 coefficients. We note a good agreement in comparing this figure with the impulse response calculated for σ=1.6 in Figure 4.28, and the impulse response calculated in Figure 3.34.

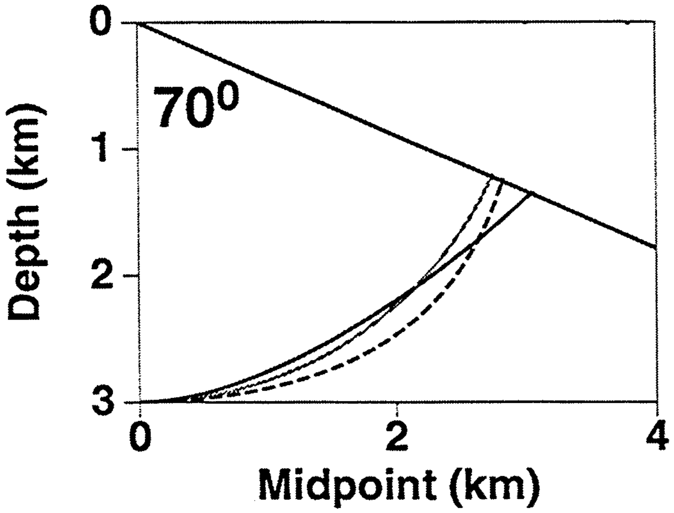

FIG. 4.25. Detail of the P-wave migration impulse responses of Figure 4.24 showing maximum dips observed for a group angle of 70 degrees. Solid black curve, $\epsilon = 0.3$, $\delta =$ -0.2. Gray curve, ϵ=0.0, δ=0.0. Dashed curve, ϵ=0.0, δ=0.3.

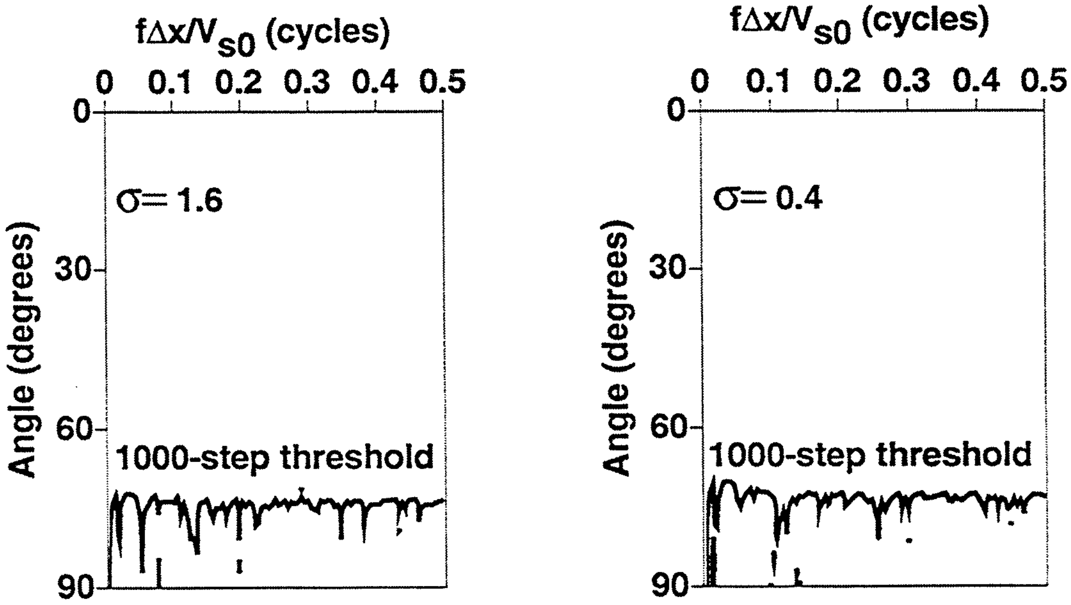

FIG. 4.26. Phase-error thresholds for the SV mode in VTI media and for $\sigma = 1.6$ ($V_{p0} =$ 4.0 km/s, $V_{s0} = 2.0$ km/s, $\epsilon = 0.3$, and $\delta = -0.1$), and $\sigma = 0.4$ ($V_{p0} = 4.0$ km/s, $V_{s0} =$ 2.0 km/s, $\epsilon = 0.3$, and $\delta = 0.2$).

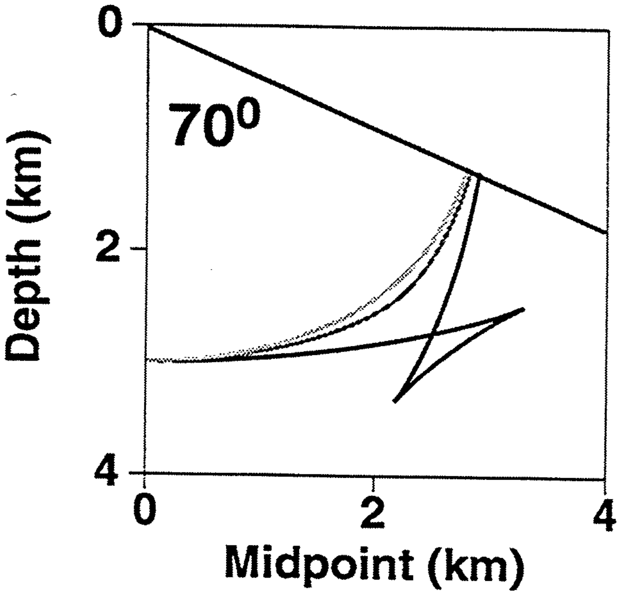

FIG. 4.27. Detail of the *SV*-wave migration impulse responses for VTI media with σ values of -0.2, 0.4, and 1.6 showing maximum dips observed for a group angle of 70 degrees.

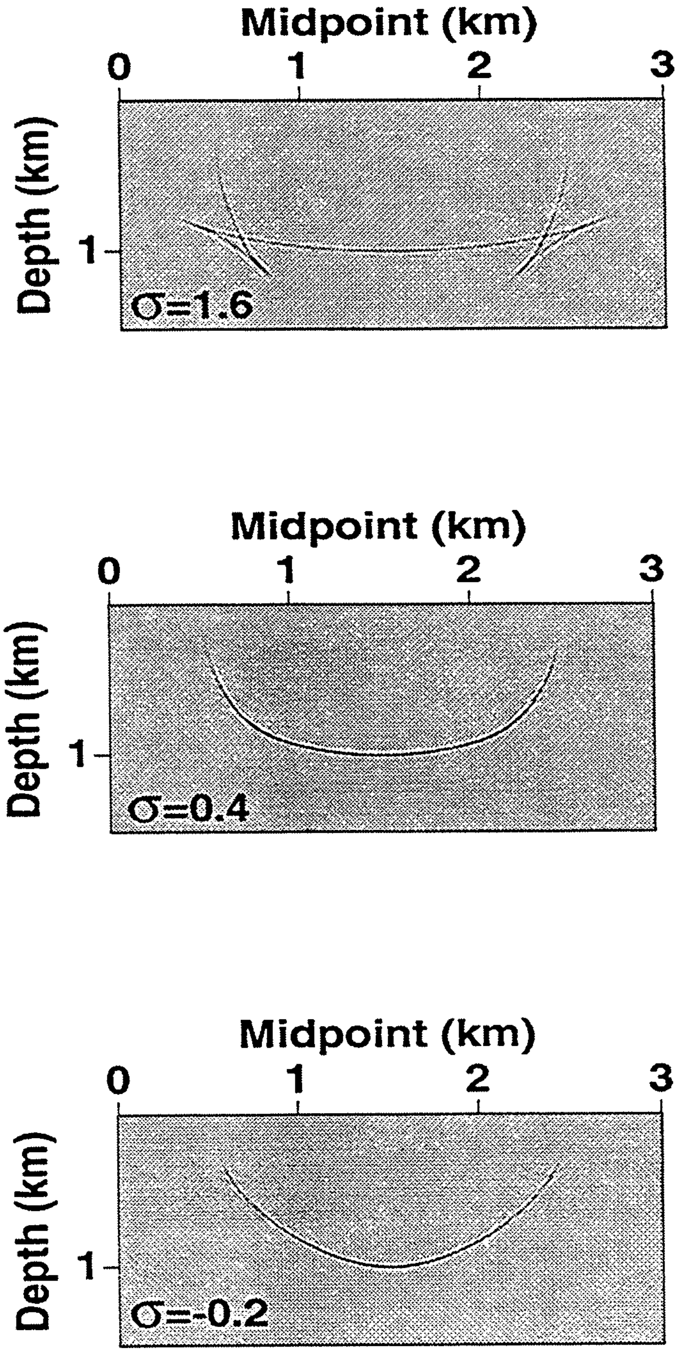

FIG. 4.28. Impulse response of migration via N=39-coefficient explicit extrapolators obtained using the minimax method, for the *SV* propagation mode in VTI media with $\sigma = 1.6$, 0.4, and -0.2.

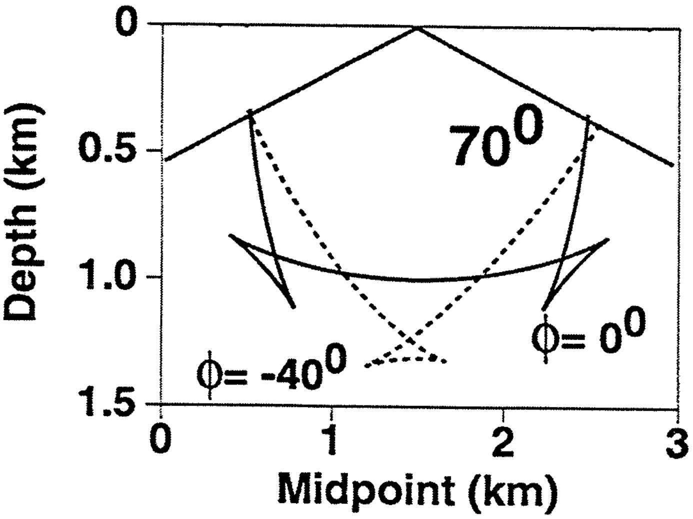

FIG. 4.29. *SV*-wave migration impulse responses for VTI media with σ=1.6 and for a vertical axis of symmetry and a tilted axis of -40 degrees. Only the dips observed for a group angle of 70 degrees are shown.

Chapter 5

APPLICATIONS OF DEPTH-EXTRAPOLATION FILTERS FOR TI MEDIA

5.1 Introduction

In Section 5.2 of this chapter, I use the MTS method to obtain depth migration sections for a field data set. Using an anisotropic dip moveout (DMO) algorithm (Anderson, et al., 1994), I obtain a zero-offset section with variable velocity and $\eta = (\epsilon - \delta)/(1 + 2\delta)$ by "painting" or interpolating multiple constant-η, zero-offset panels. The MTS filters were used because reflector dips in the data set do not exceed about 45 degrees; also, the values of the anisotropic constants obtained in the anisotropic DMO processing were relatively small.

In Section 5.3, following the same approach that Hale (1991b) used for isotropic media, I obtain 3D depth-migration impulse response for the *P*-mode in VTI media by using McClellan transformation and VTI depth-extrapolation filters for 2D depth migration. Unfortunately, for TI media with a non-vertical axis of symmetry, the circular symmetry with respect to spatial wavenumbers of the 3D depth-extrapolation operator is lost, so the McClellan transformation cannot be applied.

In Section 5.4, I describe an implementation of "pipelining" of 2D and 3D depth migration via explicit filtering using the Message Passing Virtual System (PVM). Prototype versions of 2D and 3D depth migration were implemented on a network of 25 IBM's RISC/6000 workstations, model 520 and 530.

Finally, in Section 5.5, I use VTI depth-extrapolation filters for 2D poststack depth-migration to do depth extrapolation of synthetic common midpoint-gather data in TI media. The results show that anisotropic filters produce a better focussing of the energy than that obtained using isotropic filters.

5.2 Application to field data

In this section, I apply 2D depth-migration to field data acquired in offshore Cabinda, a small detached enclave of Angola, courtesy of Chevron Oil Field Research.

Figure 5.1 shows an interpretation of a conventional time-migrated section in the area. The different tectonic movements in the area are identified in an interpretation made by Tagir Galikeev at Colorado School of Mines. Two different parts of the section, with different seismic data quality, can be defined. The upper part, of good seismic data quality, corresponds to postsalt deposition. In Figure 5.1, the top of SynRift II corresponds to the top of salt. The lower part (poor seismic data quality) corresponds to presalt structures. Approximately 25 percent of the oil in Cabinda has been found within presalt reservoirs. Of importance in the figure is the sedimentation of a shaly clastic sequence during a period of regional subsidence. This unit thickens rapidly to the left of Figure 5.1 and is faulted to the right. The faulting could be a result of both salt intrusion, most possibly high-pressure shale movement. Anisotropy estimates have been made by Chevron in the area from VSP and well-logging data; however, these estimations were not available.

The main oil target in this area are the presalt structures. Depth migration is an appropriate tool for imaging the presalt structures, as well as other structures in the section. However, as discussed in Chapter 4, in the presence of anisotropy, depth migration requires an estimate for the vertical velocity V_{p0}, as well as for the anisotropic constants ϵ and δ. Thus, the first problem to address here is to get an estimate of the vertical velocity field and these anisotropic constants.

As pointed out in Chapter 4, Alkhalifah and Tsvankin (1994) showed that in order to perform all major seismic data time-processing steps including DMO, prestack, and poststack time migration in TI media, we need to know only the zero-dip NMO velocity $V_{NMO}(0)$ and the anisotropic parameter $\eta = (\epsilon - \delta)/(1 + 2\delta)$. Anderson et al., (1994), devised a Fowler-type DMO algorithm for transversely isotropic media using the analytic expression for normal-moveout velocity given by Tsvankin (1995). Using this DMO algorithm, Anderson et al., (1994) obtain the values of $V_{NMO}(0)$ and η by inspecting zero-offset panels for different pairs of constant values of the two parameters. In order to simplify this procedure, they restrict the search in the anisotropic Fowler DMO algorithm to a single parameter η by first obtaining the NMO velocity for horizontal reflectors $V_{NMO}(0)$ from conventional velocity analysis. Then, a final zero-offset section with variable velocity and η can be "painted" or interpolated from a number of constant-η DMO/stack panels.

Figure 5.2 shows the DMO-plus-stack section calculated for η=0.0 (isotropic), and Figure 5.3 shows the DMO-plus-stack section for the time-variant η values obtained by the anisotropic Fowler DMO analysis. The estimated η values increase linearly from 0.0 in the isotropic water layer up to 0.20 at about 3 s. The arrows in both figures point to reflections produced by a major fault that has been recognized in the area. The area inside the rectangles in both figures is magnified and shown in Figures 5.4 and 5.5. Figure 5.5 shows a somewhat stronger fault reflection than does Figure 5.4. Mapping of this fault is important because this fault can act as a seal due to salt intrusion. To better see the imaging of this fault by migration, I apply a dip filter over both sections to strengthen events with slopes near that of the fault reflections in Figures 5.2 and 5.3. The approximately slope of the fault-diffractions is -0.67 s/km. The dip filter applied multiplies the amplitude of the slopes between -0.8 and -0.5 s/km by 2.5, while it simply passes all the slopes less than -1.0 s/km and greater than -0.4 s/km. Figures 5.6 and 5.7 show the same magnified area of Figures 5.4 and 5.5 after the dip filtering. The anisotropic DMO algorithm produces better delineation of the fault reflection than does its isotropic counterpart in Figure 5.6.

As opposed to time migration in TI media, where only $V_{NMO}(0)$ and η are needed, depth migration requires the individual values of ϵ and δ to produce the correct location

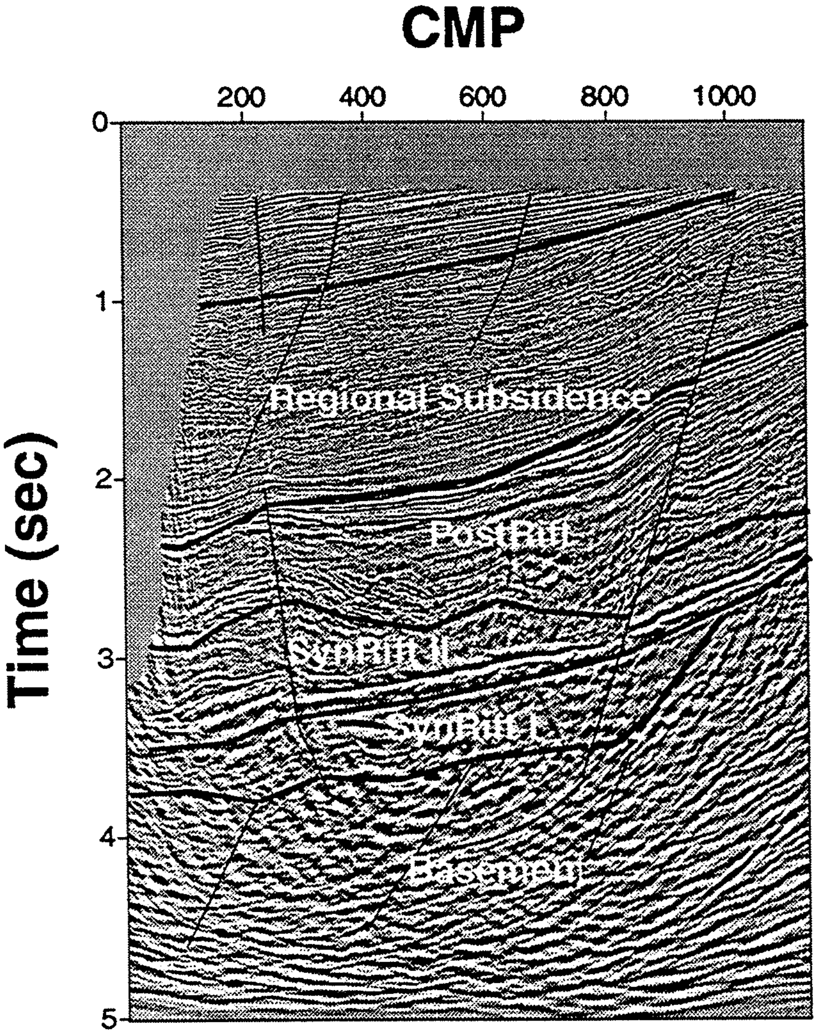

FIG. 5.1. Seismic interpretation of the line in study showing the different tectonic movement in the area.

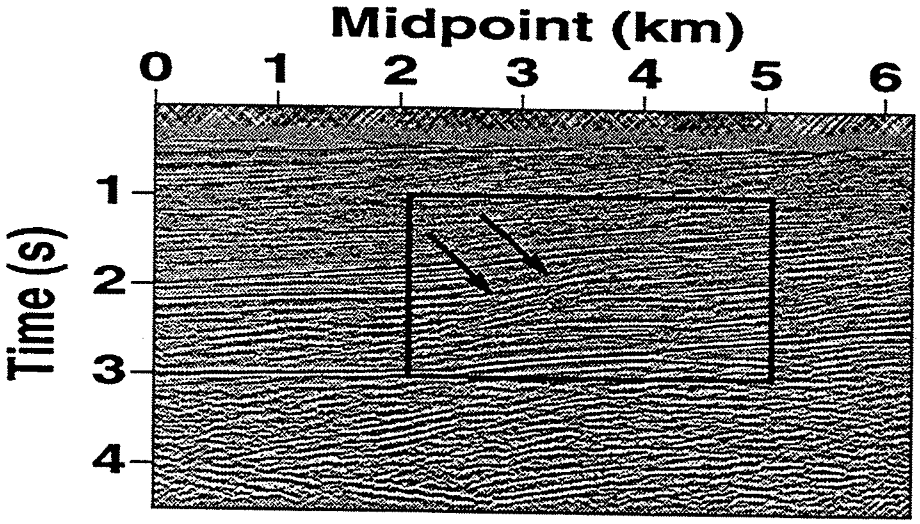

FIG. 5.2. DMO-plus-stack section obtained assuming an isotropic medium.

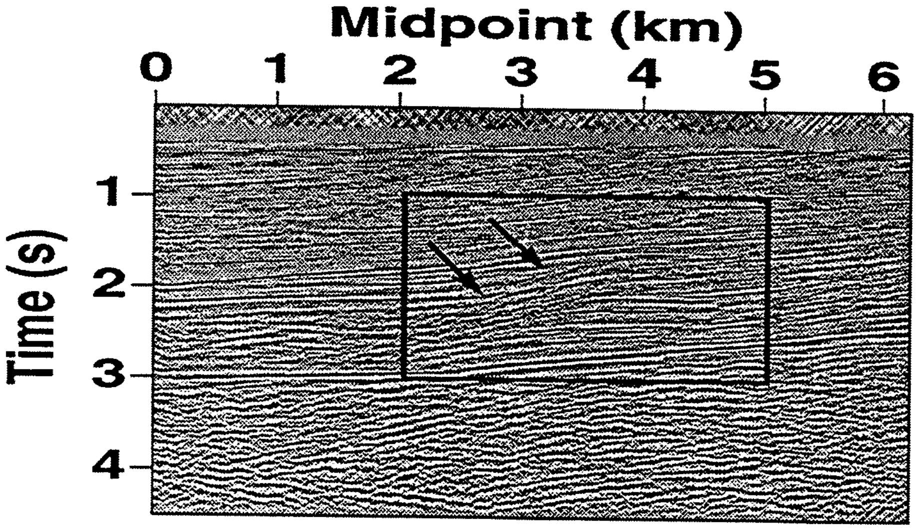

FIG. 5.3. DMO-plus-stack section obtained assuming an anisotropic medium with η variable in time.

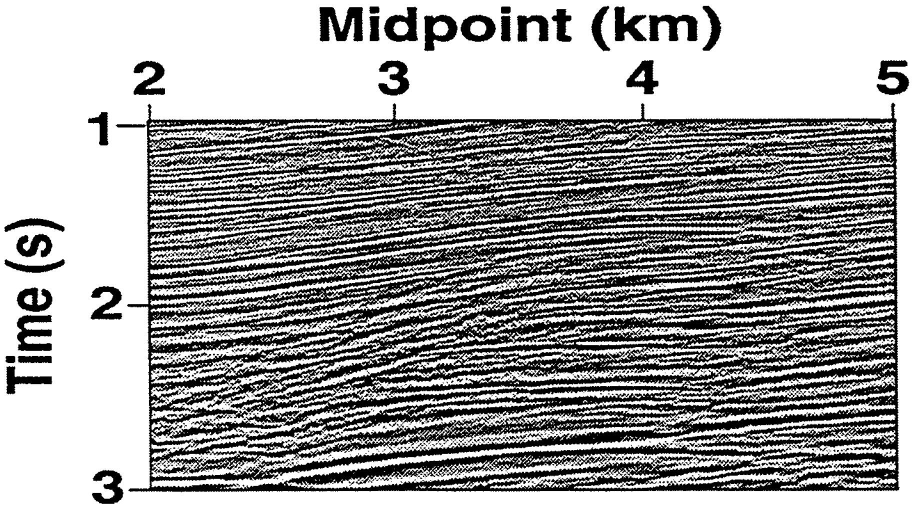

FIG. 5.4. Detail of the isotropic DMO-plus-stack section in Figure 5.2.

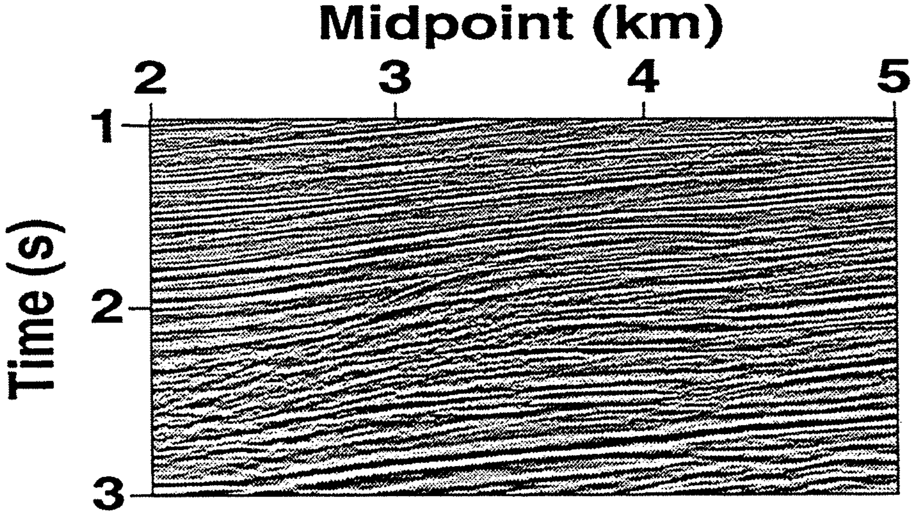

FIG. 5.5. Detail of the TI DMO-plus-stack section in Figure 5.3.

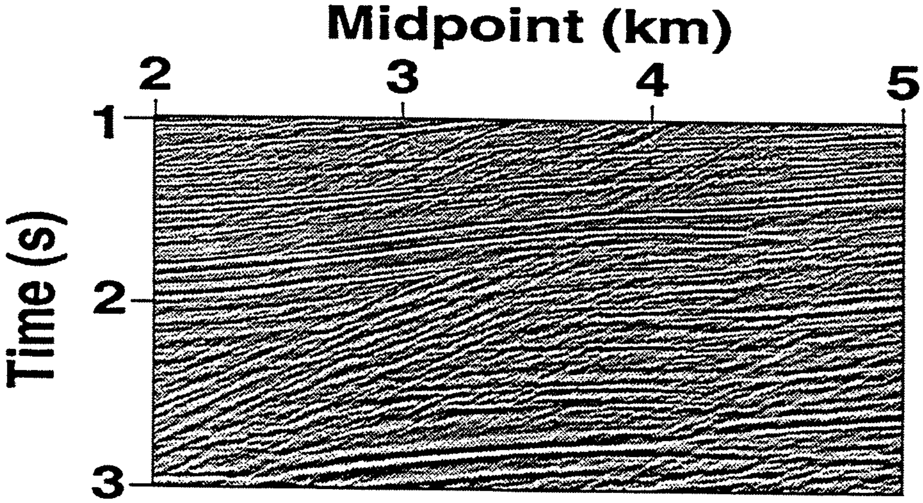

FIG. 5.6. Detail of the same isotropic DMO-plus-stack section as in Figure 5.2 but with a dip filter applied to strengthen the sloping reflections.

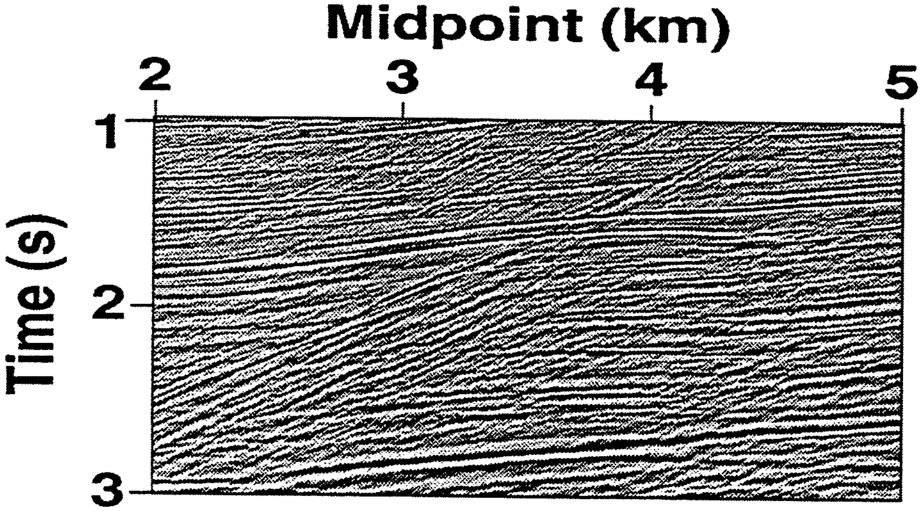

FIG. 5.7. Detail of the same TI DMO-plus-stack section as in Figure 5.3 but with a dip filter applied to strength the sloping reflections.

of reflectors in depth. Given a constant value of η, many different combinations of ϵ and δ can produce the same η value. Alkhalifah and Tsvankin (1994) have shown that for a fixed $V_{NMO}(0)$ and η, all possible combinations of ϵ and δ would produce the same lateral displacement of dipping reflectors in time migration. In depth migration, this same result holds because lateral displacements in time and depth migration are the same. However, in depth migration, and where vertical velocities V_{p0} are obtained from NMO velocities, V_{p0} has to be recalculated from the relation $V_{p0} = V_{NMO}(0)/\sqrt{1+2\delta}$ each time that a new value of δ is used. Changes in V_{p0} would produce vertical displacements of horizontal and dipping reflectors, but the lateral displacement of dipping reflectors would be about the same if we always keep η constant.

If, instead, V_{p0} values are obtained from well-logging or VSP data, the depth-migration solution is unique because we can calculate δ from the relation $V_{p0} = V_{NMO}(0)/\sqrt{1+2\delta}$, and ϵ from the η values obtained during the seismic data processing in time using the approach of either Anderson et al., (1994) or Alkhalifah and Tsvankin (1994).

For simplicity, and due to the many different possible combinations of ϵ and δ that can produce a constant value of η, here I calculated only four different depth-migration sections using explicit operators. One section was calculated assuming an isotropic medium for the depth-migration step (the DMO was the one in Figure 5.5, which took anisotropy into account). The other two sections were calculated for the same constant value of η, equal to the average value obtained from the anisotropic-DMO analysis (η=0.1), but for two different pairs of ϵ and δ: ϵ=0.1 and δ=0.0, and ϵ=0.0 and δ=-0.083. In addition to producing the same η value, these values of ϵ and δ were chosen to show two important situations: First, when δ=0.0, the V_{p0} velocity field derived from the values of $V_{NMO}(0)$ is the same for isotropic and TI media, so differences in migration results between the isotropic and TI media would be due just to the influence of anisotropy in the depth-migration step. Second, when $\delta \neq 0.0$, the velocity V_{p0} field obtained from $V_{NMO}(0)$ values for TI media differs from that obtained for isotropic media, producing a relative displacement of the imaged reflectors in depth with respect to the depths obtained in the isotropic migrated section. In both situations, the lateral displacement of the dipping reflectors are the same because the same value of η is used in both depth migrations.

Also, because the maximum dip for the fault is about 45 degrees, and the anisotropic values obtained from the DMO analysis for η are small, MTS filters can be used with confidence; they will produce better amplitude estimates than will the LS and minimax filters.

Figure 5.8 shows the depth-migration output obtained using isotropic MTS filters over the stack section of Figure 5.5 obtained using the TI DMO. Because the sedimentary section is gently dipping and velocities are believed to be controlled by depth, the interval velocities used in the depth-migration process were obtained from the stacking velocities using the Dix equation. Basically, Figure 5.8 shows the result of ignoring anisotropy just in the depth-migration process; a relatively good imaging of the fault has been obtained.

For comparision, Figure 5.9 shows the depth migration obtained using VTI depth extrapolation filters calculated for $\epsilon = 0.1$ and $\delta = 0.0$ on the stack section of Figure 5.5.

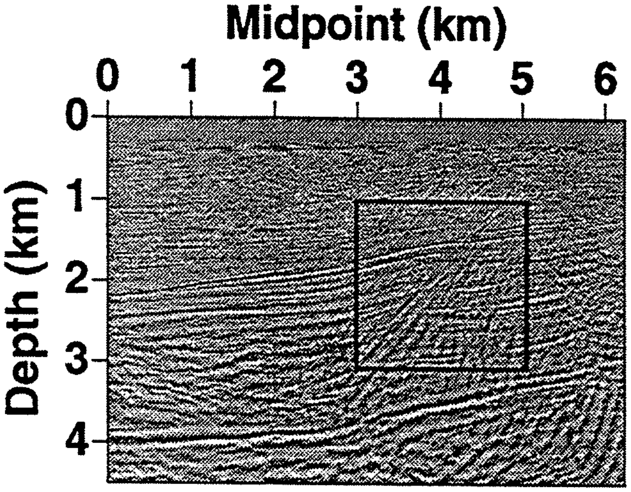

FIG. 5.8. Isotropic depth migration obtained using explicit extrapolators for the TI DMO-plus-stack section in Figure 5.5

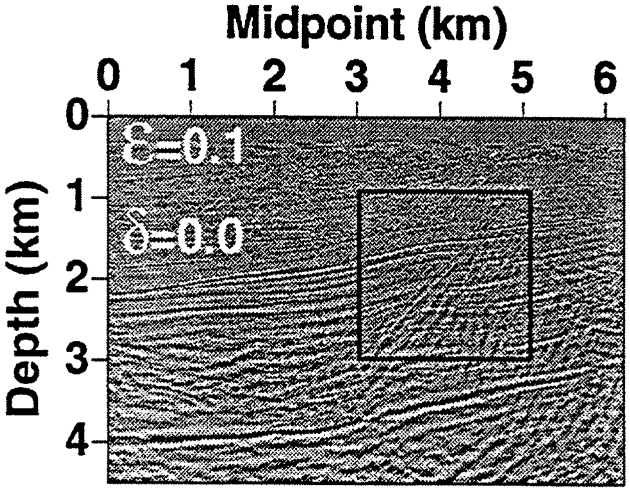

FIG. 5.9. Anisotropic depth migration obtained using explicit extrapolators for the TI DMO-plus-stack section in Figure 5.5, for ϵ=0.1 and δ=0.0

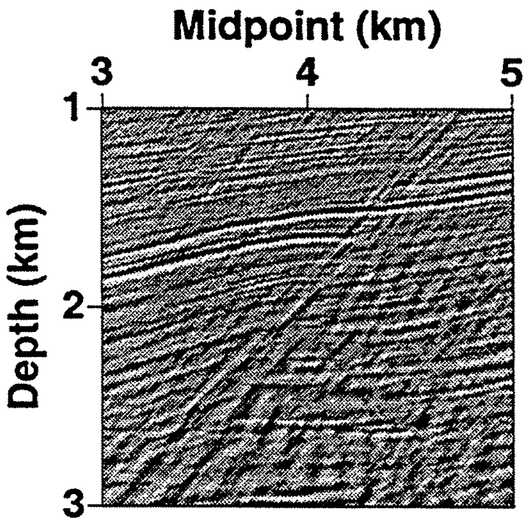

FIG. 5.10. Detail of isotropic depth migration in Figure 5.8 obtained for the TI DMO-plus-stack section in Figure 5.5.

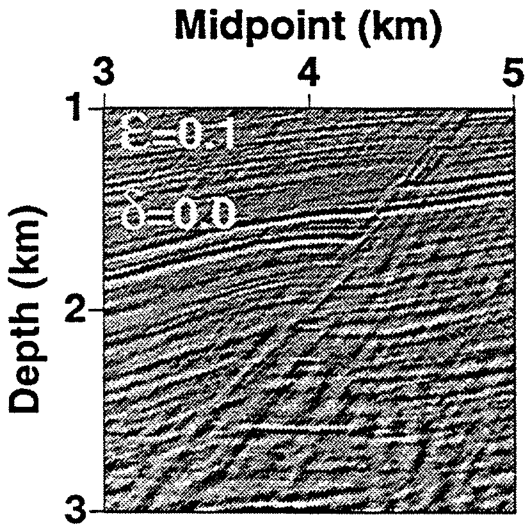

FIG. 5.11. Detail of anisotropic depth migration in Figure 5.9 obtained for the TI DMO-plus-stack section in Figure 5.5.

Because δ=0.0, and the V_{p0} velocity field is obtained from NMO velocities, the V_{p0} values used in Figure 5.9 are the same as those used in Figure 5.8, so the differences between these two sections are due solely to ignoring anisotropy during the depth-migration step, but not during the DMO process. Figure 5.9 shows an imaging of the fault that is similar to that obtained in Figure 5.8, and Figures 5.10 and 5.11 give a close view of the fault area imaged in Figures 5.8 and 5.9, respectively. The closeup images differ almost inconsequentially. The fault, which has about 50-degree dip, is imaged just slightly further to the right by the TI migration. Here, while use of anisotropy in the DMO process was important to getting a good image of the fault, upon comparing Figures 5.10 and 5.11 we conclude that the influence of anisotropy in the depth-migration process of these data was negligible. These results agree with numerical results obtained by Alkhalifah and Larner (1994), which predict small lateral position errors for dip less than 50 degrees (for low values of ϵ and δ, that is $\epsilon \leq 0.1$ and $\delta \leq 0.1$) when data from TI media are migrated with isotropic migration algorithms.

Again, while anisotropy is not an important factor in the depth migration process, DMO is. To see this, Figure 5.12 shows the depth-migration output obtained using the same isotropic MTS filters as in Figure 5.8, but this time, the input stack section is that of Figure 5.4, calculated using the isotropic DMO algorithm. This would be the result obtained in normal migration practice today, which completely ignores anisotropy. Figure 5.13 shows the closeup of the depth migration in Figure 5.12. The imaged fault is much weaker in this figure than in either Figure 5.9 or 5.11. Clearly, the use of anisotropy in the DMO process yields better delineation of the fault.

To see the influence of δ on the results of depth migration, Figures 5.14 and 5.15 show a depth-migration section and a detail of this section, respectively, obtained using explicit VTI filters over the TI DMO section in Figure 5.5 for ϵ=0.0 and δ=-0.083. For this example, because $\delta \neq 0$, the V_{p0} velocity field must be recalculated from the NMO velocities; specifically, because $\delta < 0$, the new V_{p0} velocity values will be greater than those used in Figures 5.8 and 5.9 by almost 10 percent. As a result, the horizontal and dipping reflectors are imaged deeper in Figure 5.14 than in Figure 5.8. However, the dipping reflectors are at the same lateral position, independent of the choice of ϵ and δ.

In summary, the results of this section show that when only seismic surface information is available, the use of Anderson et al., (1994) anisotropic DMO, as opposed to conventional isotropic DMO, can help not only to estimate anisotropic parameters (η) for time-related seismic data processing, but also to obtain a stack section with better definition of dipping events. For the low estimated values of η, and for the range of dips (0-45 degrees) present in the data, the use of the anisotropic DMO algorithm plus isotropic depth migration was enough to get a good imaging of the fault. The influence of anisotropy on just the imaging process in depth migration for this data is negligible. However, the influence of anisotropy in the DMO process was appreciable. Even when surface seismic information was not enough to estimate the complete set of parameters needed for depth migration, honoring η in depth migration guarantees at least the correct lateral position of dipping events in the final depth-migrated section. Lack of information about δ, however, leaves uncertainty in the imaged depth of flat and dipping events.

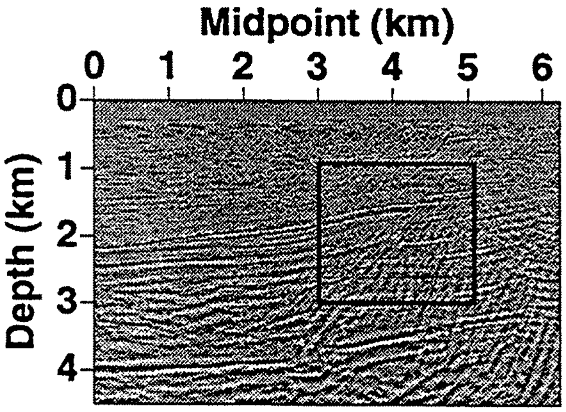

FIG. 5.12. Isotropic depth migration obtained using explicit extrapolators for the isotropic DMO-plus-stack section in Figure 5.4.

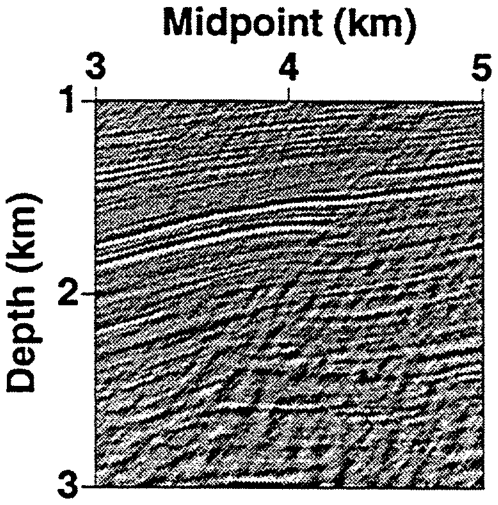

FIG. 5.13. Detail of isotropic depth migration in Figure 5.12 obtained for the isotropic DMO-plus-stack section in Figure 5.4.

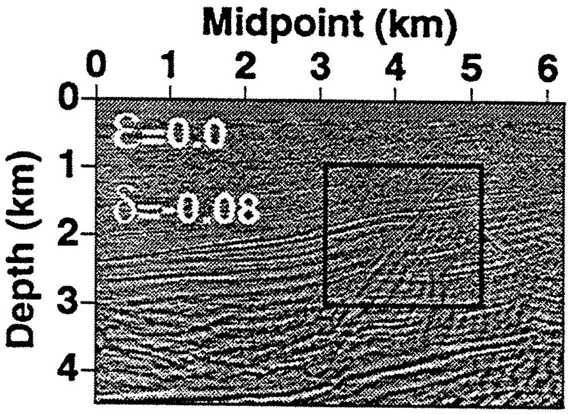

FIG. 5.14. Anisotropic depth migration obtained using explicit extrapolators for the TI DMO-plus-stack section in Figure 5.5, and for ϵ=0.0 and δ=-0.083

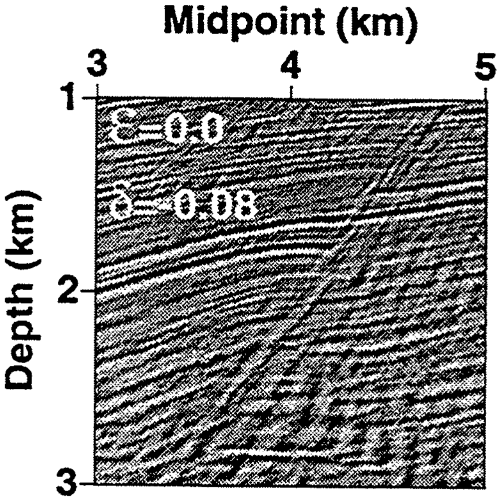

FIG. 5.15. Detail of the anisotropic depth migration in Figure 5.14 obtained applied to the TI DMO-plus-stack section in Figure 5.5.

These conclusions, which have been understood by Alkhalifah and Tsvankin (1994), are confirmed with application of the MTS operators here.

5.3 3D depth migration via McClellan transformations

Three-dimensional (3D) migration in isotropic media requires a downward-extrapolation operator (DEO) given by (Hale, 1991b)

$$D\left[k,\omega\right] = \exp\left\{i\frac{\Delta z}{\Delta x}\left[\left(\frac{\omega\Delta x}{V}\right)^2 - k^2\right]^{\frac{1}{2}}\right\}, \tag{5.1}$$

where k is given now by $k = \sqrt{k_x^2 + k_y^2}$, with k_x and k_y denoting inline and crossline wavenumbers, respectively, with azimuth φ (angle of the plane-wave with respect to the x-axis) given by $\tan\varphi = k_y/k_x$. Both wavenumbers (k_x and k_y) are normalized by the inline sampling interval Δx, which will be assumed to be equal to the crossline sampling interval Δy. This assumption ($\Delta x = \Delta y$) simplifies the application of McClellan transformation to 3D depth migration. However, as pointed out by Hale (1991b), one may resample the seismic wavefield to satisfy this assumption or use McClellan transformations that account for unequal sampling intervals (Merserau et al., 1976).

For transversely isotropic media, the 3D DEO can also be written in the form of equation (5.1), but now considering the functional dependence of the phase velocity on propagation angle θ

$$D\left[k,\omega\right] = \exp\left\{i\frac{\Delta z}{\Delta x}\left[\left(\frac{\omega\Delta x}{V_{ph}(\theta)}\right)^2 - k^2\right]^{\frac{1}{2}}\right\}. \tag{5.2}$$

For 3D depth migration in isotropic media, Hale (1991b) shows that depth extrapolation can be performed by using the same filter coefficients used for isotropic 2D depth migration. Specifically, McClellan filters transform any one-dimensional filter (as those used in 2D depth migration) into an approximately circularly symmetrical two-dimensional filter. The same reasoning followed by Hale (1991b) can be applied for 3D depth migration in TI media: we can use the filter coefficients for 2D depth migration in TI media obtained above, and the same McClellan filters used by Hale (1991b) to convert these one-dimensional filters into approximately circularly symmetrical two-dimensional filters. For TI media with a tilted axis of symmetry, however, the spatial wavenumbers in the inline and crossline directions are not symmetrically distributed about zero dip, i.e., $k_x(\theta) \neq k_x(-\theta)$, and likewise for k_y. Thus, for tilted symmetry axis, the symmetry in the two-dimensional filters is lost, so a direct application of McClellan transformations is not possible.

Figure 5.16 shows a 3D impulse response for a homogeneous TI media with a vertical axis of symmetry and Thomsen parameters of V_{p0}= 2 km/s, V_{s0}= 1 km/s, ϵ=0.0, and δ=-0.3. The 3D impulse response was obtained by using depth-extrapolation filters for 2D depth migration calculated by the MTS method, and the improved McClellan

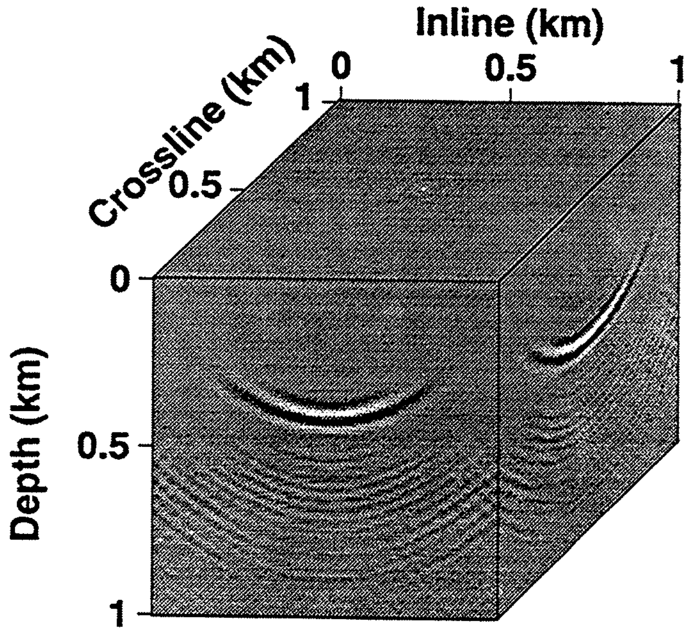

FIG. 5.16. 3D migration impulse response for the P propagation mode and for Thomsen parameters, V_{p0}=2.0 km/s, V_{s0}=1.0 km/s, ϵ=0.0, and δ=-0.3.

transformation filter given by Hale (1991b). The same 3D depth-migration program used by Hale (1991b) for isotropic media was used here to obtain the impulse response of Figure 5.16, I needed only to change the table of 2D depth-extrapolators. In this test, the spatial sampling intervals $\Delta x = \Delta y = \Delta z = 10$ m, and the time sampling interval $\Delta t = 10$ ms. The input data consisted of zeros throughout, except for the input trace located at $x = y = 0.5$ km, which contained a single zero-phase Ricker wavelet centered at $t = 0.75$ s, with a peak-frequency of 20 Hz.

To get a closer look at the results, we can look at the slice of this cube for a given constant depth, as well as inline and crossline sections through this cube. Figure 5.17 shows a slice of the 3D depth-migrated cube of Figure 5.16 for the depth z=0.5 km. The dotted curve in the figure corresponds to the theoretical position calculated using Thomsen equations for group angle and group velocity extended to 3D. To calculate the theoretical shape of the depth-migration impulse response in 3D, consider Figure 5.18 and note that the coordinates (x_0, y_0, z_0) on the depth-migration impulse response surface are given by

$$x_0(\phi) = \frac{V_g(\phi)}{2} t_0 \sin\phi \cos\varphi$$

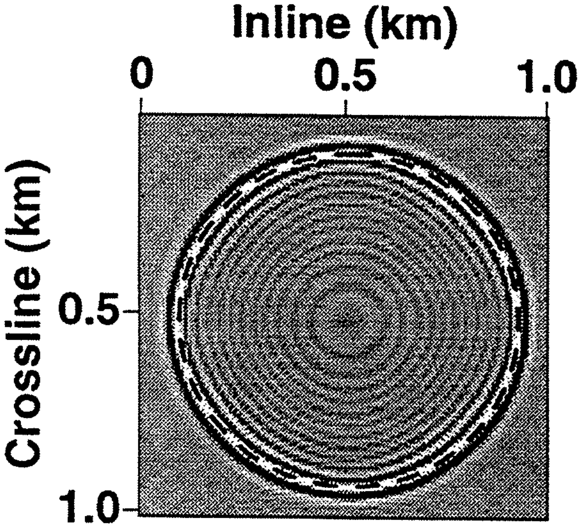

FIG. 5.17. Slice of the impulse response of TI 3D migration in Figure 5.16 for the depth z=0.5 km. The dotted line is the theoretical position of the impulse response calculated using equation (5.1).

$$y_0(\phi) = \frac{V_g(\phi)}{2} t_0 \sin\phi \sin\varphi$$
$$z_0(\phi) = \frac{V_g(\phi)}{2} t_0 \cos\phi, \qquad (5.3)$$

where t_0 is the time of the impulse on the input 3D zero-offset section, and φ is the azimuth with respect to the x-axis. For a constant group angle ϕ, a parametric plot of x_0 and y_0 as a function of the azimuth angle φ in equation (5.3) will produce a circle. $z_0(\phi)$ in equation (5.3) is constant only if ϕ is constant. To calculate a theoretical depth slice using equation (5.3), we need only fix the depth of the impulse response z_0 and let the azimuth φ change from 0 to 360 degrees. Thus, equation (5.3) is evaluated for a constant group angle ϕ, so the inline x_0 and crossline y_0 positions in the impulse response change with azimuth φ only, producing a circle for any depth-slice of the 3D migration impulse response in a homogeneous VTI medium. In homogeneous isotropic media, the depth-slices of 3D migration impulse response are also circles. Figure 5.17 shows a good agreement between the theoretical position of the impulse response and the slice obtained from the migrated cube of Figure 5.16.

To further check the impulse response in Figure 5.16, Figure 5.19 shows a cross-section of the migrated cube in Figure 5.16 for the crossline coordinate y=0.5 km. Ideally, this line would be kinematically equal to a 2D depth migration impulse response because, in the original zero-offset section, the only non-zero trace was also located at the

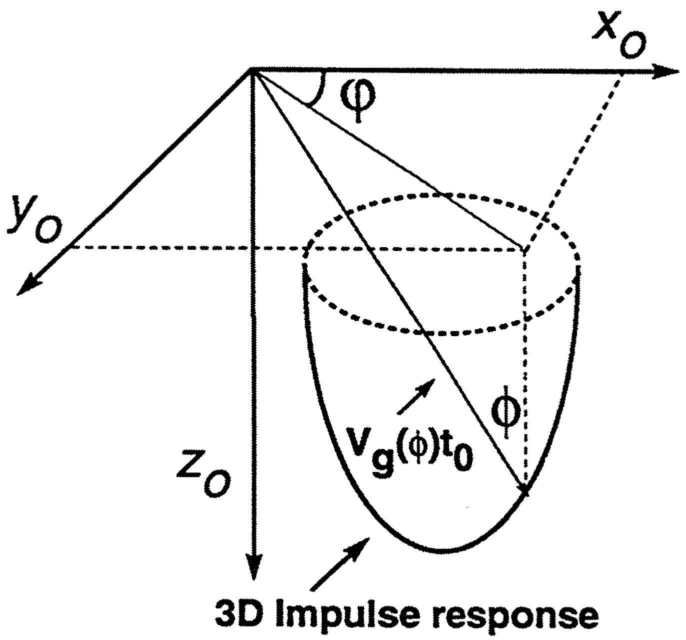

FIG. 5.18. Theoretical 3D depth-migration impulse response in anisotropic media. x_0, y_0, and z_0 represent the spatial coordinates of any point on the migration impulse response.

crossline coordinate y=0.5 km. The dotted line in Figure 5.19 shows the shape of the 2D theoretical impulse response obtained using equations (2.21). Figure 5.19 also shows a good agreement between the theoretical 2D response and the calculated 3D cross-section.

The results here show that McClellan transformations can be used to do 3D depth migration in transversely isotropic media with a vertical axis of symmetry. The essential point, comparable to that of Hale (1991b) for isotropic media, is that after calculating the explicit filters for 2D depth migration in VTI media, the same filter coefficients are ready for use in 3D depth migration; no additional cost is entailed to calculate new coefficients. This is one of the main advantages of explicit filtering in relation to other depth-migration procedures such as, for example, finite differences or Gaussian beam migration, whose extension to 3D are cumbersome and inefficient (Claerbout, 1985; Artley, 1994). I should also pointed out that in a recent work (Soubaras, 1992), 3D depth migration in isotropic media via explicit filtering has been accomplished using an approach that differs from McClellan transformation. Apparently, this new approach reduces the cost of the process and increases the accuracy of the 3D operators. However, Soubaras's approach is similar to the McClellan transformation approach in the sense that both use the same filter coefficients calculated for 2D depth migration. Therefore, Soubaras's approach for isotropic 3D depth migration could be also implemented for TI media using the extrapolation filters calculated here.

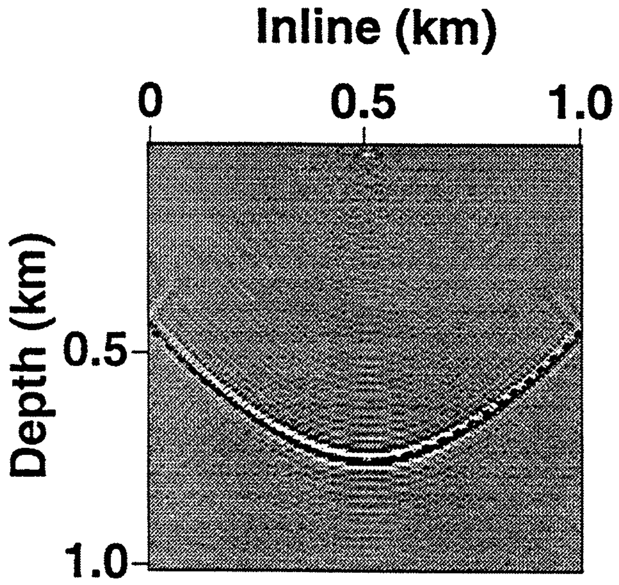

FIG. 5.19. Impulse response of TI 3D migration in Figure 5.16 for the crossline coordinate y=0.5 km. The dotted line is the position of the theoretical 2D impulse response obtained using equation (2.21).

5.4 2D and 3D pipeline implementation of explicit extrapolation

The availability of message-passing software such as PVM (parallel virtual machine, Beguelim et. al., 1991) makes possible an easy pipeline implementation of 2D and 3D depth migration via explicit filtering in a network of heterogeneous machines. Using PVM each machine in a network can be treated as an independent processor of a large parallel or vector computer. However, because the communication between machines in a network is not so effective as the communication between processors inside a parallel or vector computer, the communication cost is a limiting factor in the design of applications using PVM.

A practical implementation of the explicit depth-extrapolation process in PVM is pipelining. In pipelining, each independent processor in the computer would calculate a separate depth step in the migrated section for all x positions and frequencies ω. However, because calculation of the wavefield for a given depth z requires the previous computation of the wavefield for $z-\Delta z$, each processor has to communicate the extrapolated wavefield value to the next processor, so how can the pipelining be implemented?

Figure 5.20 shows a schematic representation of the process. The processors are represented along the vertical axis, and the total time of the process is represented along the horizontal axis. P_i represents the calculated wavefield $P(\omega_1, x, z)$. Thus, in Figure 5.20, the first processor will calculate the wavefield $P(\omega_1, x, \Delta z)$ at time t_1. Once the

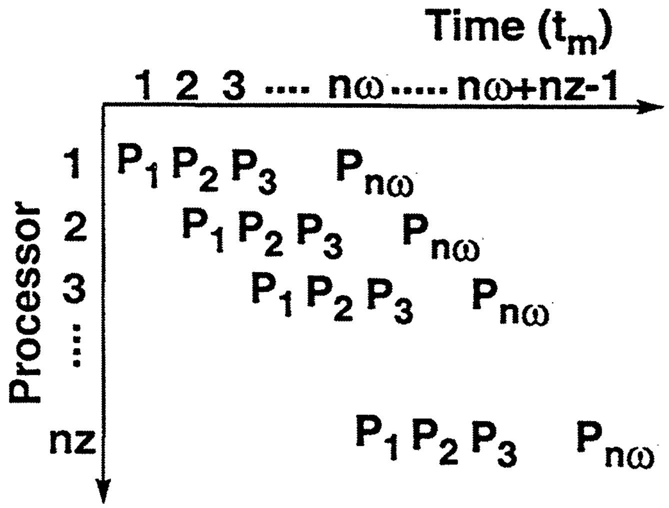

FIG. 5.20. Pipelining of the depth extrapolation process for the ideal case of nz processors.

computation is complete for the lowest frequency (ω_1), the first processor then sends the calculated wavefield to the second processor. At time t_2, neglecting the communication time between processors, the first and second processors are simultaneously calculating $P(\omega_2, x, \Delta z)$ and $P(\omega_1, x, 2\Delta z)$. The same sequencing will take place with the other processors as time increases.

The time employed by one processor in the migration process is $n\omega * t_m$, where $n\omega$ is the number of frequencies and t_m is the time needed to calculate the convolution in x. In a conventional implementation, where we have only a single processor, the total computer time required to calculate the explicit depth-extrapolation process would be approximately $t_m * nz * n\omega$, where nz is the total number of depth steps. For comparison, neglecting the communication cost, the total time employed by all the nz processors to calculate the depth migration section is $(n\omega + nz - 1) * t_m$. Thus, the ratio between the times for the conventional implementation and for the pipeline implementation (i.e. the speedup factor) with nz processors would be

$$\frac{n\omega * nz}{n\omega + nz - 1}. \tag{5.4}$$

A similar pipeline implementation to that described in Figure 5.20 applies for 3D depth migration. The only difference is that P_i in Figure 5.20 would represent the calculated wavefield $P(\omega_i, x, y, z)$ and t_m the computer time needed to calculate the convolution process in x and y. Thus, equation (5.4) also gives the speedup factor for 3D depth migration.

Let us apply equation (5.4) to estimate the computer time expected for the depth migration of the Angolan field data set. As described before, this data set consists of some 500 CMP's, 750 samples in time, and the depth-migration sections were calculated for 600 steps of depth extrapolation. If we make the approximation that $nw \approx nt$, we get $(750 * 600)/(750 + 600 - 1) \approx 333$ as the speedup factor when nz=600 processors are used and when the communication cost is neglected. The network of IBM RS6000 used for the calculation of the depth-migration sections here, however, consists of only 25 machines. Therefore, the speedup factor is roughly approximated as $(25/600) * 333 \approx 14$. For the 2D depth migration calculations, the experimental speedup factor obtained was about 12, impliying that the communication problem did not play an important role.

For the 3D migration impulse responses calculated in Section 5.3, $nx = ny = nz = nt$=101. Equation 5.4 predicts an speedup factor of about $101 * 101/201 \approx 50$, when nz=101 processors are used. For 25 processors, the speedup factor would be roughly $(25/101) * 50 \approx 12.5$. For the 3D depth migration calculations, the experimental speedup factor obtained was about 7, so the communication problem played an important role in the process.

These results for 2D and 3D depth migration are preliminary and a more detail analysis is needed to improve the depth-migration implementations in PVM. In our implementation for 3D depth migration, the communication requirement is high and needs to be improved. However, for the 2D implementation the experimental speedup factor is close to the theoretical expected factor.

5.5 Depth extrapolation of prestack data

The depth-extrapolation filters calculated in this thesis were designed basically to do 2D *poststack* depth migration. The downward-extrapolation process needed in 2D prestack migration, however, can also be accomplished using these 2D poststack depth-extrapolation filters.

Figure 5.21 shows a synthetic CMP gather calculated over a homogeneous TI model with Thomsen parameters V_{p0}=2.0 km/s, V_{s0}=1.0 km/s, ϵ=0.0, and δ=0.3. The model in depth consists of three horizontal reflectors at depths of 0.5, 1.0, and 1.5 km. The synthetic data were generated using a ray-tracing program for TI media (Alkhalifah, 1995b). Then, I used isotropic depth-extrapolation filters obtained by the minimax method to downward continue the receivers in the CMP data of Figure 5.21. The receivers are extrapolated to the true depths of the horizontal reflectors using the correct value of V_{p0}, and the results are shown in Figure 5.22. For display purposes, a time shift of $\Delta t = z/V_{p0}$ where z is the extrapolated depth has been applied in all the plots of Figure 5.22. Figure 5.22 basically shows the wavefield that the receivers would record if they were buried in the subsurface at depth z. Because we are extrapolating the receivers to the true depth of the flat reflectors, the ideal recorded wavefield in each one of the plots of Figure 5.22 would be a point. However, Figure 5.22 shows that the use of isotropic extrapolators to downward continue prestack data from TI media do not produce good focussing of the seismic energy. Moreover, the problem worsen as the depth increases.

Figure 5.23 shows the extrapolated wavefield when minimax explicit filters calculated

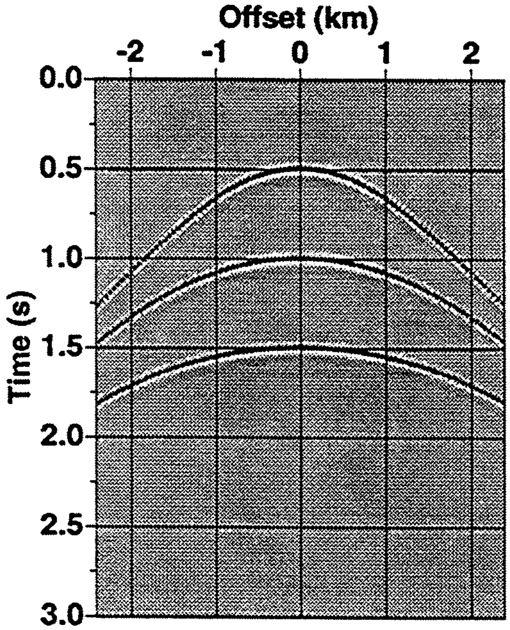

FIG. 5.21. CMP gather for a homogeneous TI medium with Thomsen parameters of V_{p0}=2.0 km/s, V_{s0}=1.0 km/s, ϵ=0.0, and δ=0.3. The original model in depth contains three flat reflectors.

for the correct set of Thomsen parameters are used. Honoring anisotropy in the prestack depth-extrapolation process has produced a better focussing of the seismic wavefield, even for the deepest reflector, at 1.5 km. This result indicates the importance of considering anisotropy in prestack migration.

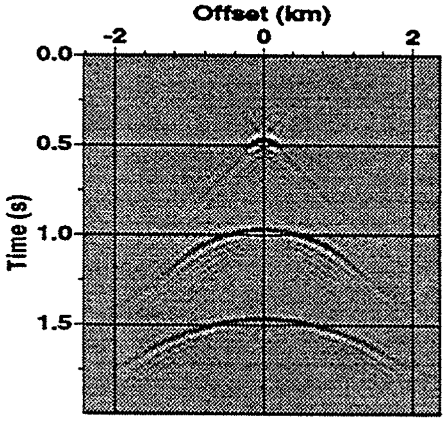

Z=0.5 km

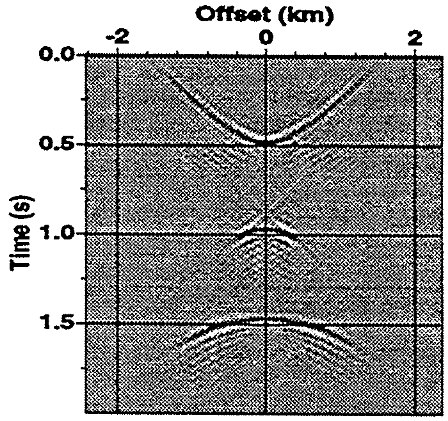

Z=1.0 km

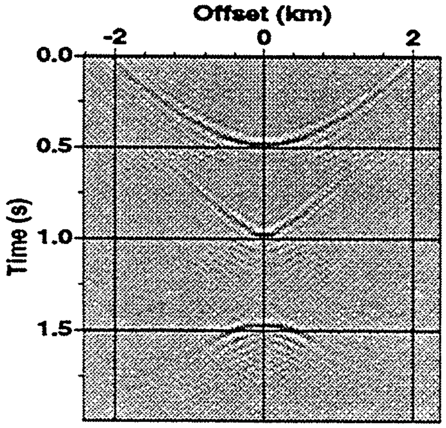

Z=1.5 km

FIG. 5.22. Downward-extrapolated wavefield from CMP data of Figure 5.21 using explicit isotropic filters.

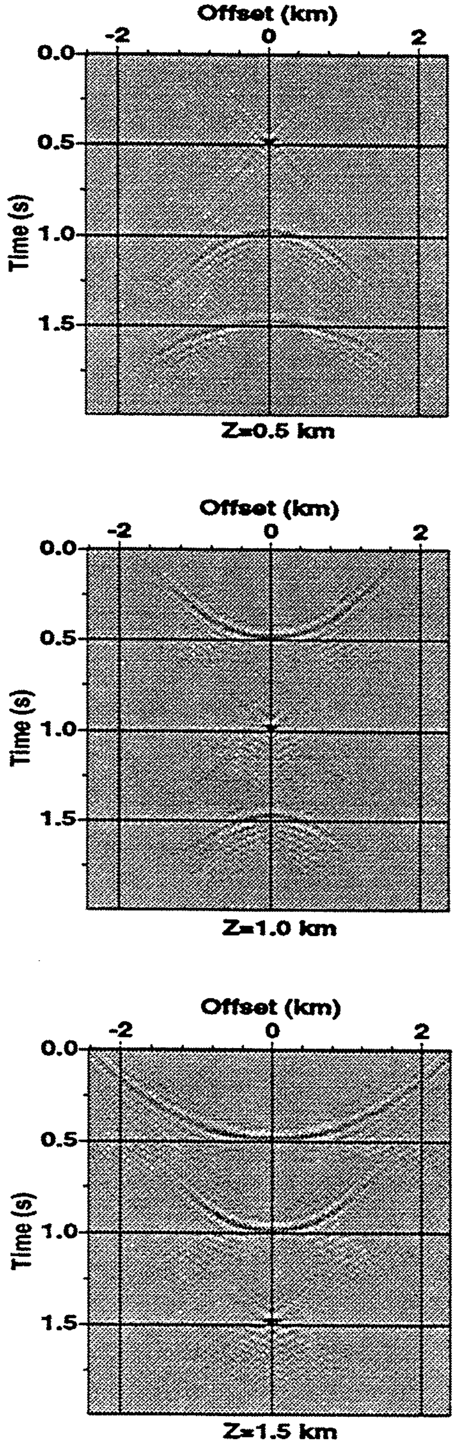

FIG. 5.23. Downward-extrapolated wavefield from CMP data of Figure 5.21 using explicit anisotropic filters calculated using the correct Thomsen parameters.

Chapter 6

CONCLUSIONS

Explicit 2D depth-extrapolation filters for TI media with vertical and tilted axis of symmetry, and for all the propagation modes (*P*, *SV*, and *SH*), can be derived by generalizations of the modified Taylor series, least-squares, and minimax methods, initially developed for isotropic media. Also, just as for isotropic media, these 2D extrapolators for TI media with a vertical axis of symmetry can be used in the McClellan transformation (Hale, 1991b) to do 3D depth migration. However, for TI media with a tilted axis of symmetry, a direct application of McClellan transformations is unfortunately not possible.

For all the implemented methods, the results here show that the accuracy of the extrapolators (for a constant filter length) is a function of the elastic properties in the medium. For the *P* mode, the accuracy of the operators increases with increasing values of δ, and decreases for increasing values of ϵ. In elliptical media ($\epsilon = \delta$), the accuracy of the extrapolators for the *P* mode is relatively insensitive to the degree of anisotropy. In the *SV* mode, the calculation of the operators is basically governed by the σ parameter, but the accuracy does not change much for typical values of σ found in sedimentary basins. Also, because there is no phase-velocity dependence on θ for elliptical media in the *SV* mode, filters for that mode behave identically to those for isotropic media. Explicit filters for the *SH* mode can be obtained using the same computer programs used in the *P* mode by making $V_{p0} = V_{s0}$, and $\epsilon = \delta = \gamma$. Therefore, the accuracy in the *SH* mode is identical to that obtained in the *P* mode for elliptical anisotropy.

The examples presented also show that, from the kinematic point of view, the least-squares and minimax methods produce filters that accomplish accurate extrapolation for a wider range of propagation angles than do those obtained using the modified Taylor series method. However, from the dynamic point of view and for low propagation angles (i.e., less than 30 degrees for most VTI media), the modified Taylor series method produces more accurate amplitudes than those produced by the least-squares and minimax methods. These results suggest two different applications for the methods implemented here: in areas with low dips and in order to get better amplitude estimations, modified Taylor series filters would be preferred over least-squares and minimax filters. In contrast, in areas with relative larger dips, least-squares and minimax filters would be preferred over modified Taylor series filters in order to better delineate the subsurface structures.

Regarding computational cost in obtaining the filters, the minimax method is about five times less expensive than the least-squares method and about half as costly as the modified Taylor series method. For isotropic media, the computational cost of calculating depth-extrapolation filters can be low in relation to the cost of doing depth migration. Only one table of depth-extrapolation filters is needed to handle all the velocity heterogeneities (Holberg, 1988), and we need calculate this table of filters only once. For TI media, velocity heterogeneities can also be handled by calculating one table of extrapolators. However, in TI media with heterogeneities in the anisotropic constants, different filter-tables are needed for each combination of δ and ϵ for the P mode, and for σ in the SV mode. Thus, the computational cost in the filter-calculation phase can be of the same order as that of the depth-migration process itself. In this situation, relative to the least-squares method, the minimax method can reduce considerably the cost of calculating the depth-extrapolation filters (and therefore, the total cost of the migration effort), without loss of accuracy. Thus, from this point of view, we would always prefer to use the minimax method over the LS method.

The depth-extrapolation process as applied to depth migration in TI media is determined mainly by certain Thomsen's parameters (ϵ and δ) for the P propagation mode, or by a combination of these parameters, $\sigma = (V_{p0}/V_{s0})^2(\epsilon - \delta)$, for the SV propagation mode. From the computational point of view, this result implies that for the P mode, we need only calculate tables of depth-extrapolation filters for a range of normalized frequencies ($f\Delta x/V_{p0}$) and for each pair of ϵ and δ values. All these tables can be calculated for a fixed value of the ratio V_{s0}/V_{p0}, e.g., $V_{s0}/V_{p0} = 0.5$. For the SV mode, tables of depth-extrapolation filters for only a range of normalized frequencies ($f\Delta x/V_{s0}$) and for each constant value of σ would be needed.

From the seismic data-processing point of view, to do depth extrapolation for each propagation mode (P or SV), we need to know the vertical velocities (V_{p0} or V_{s0}) to calculate the corresponding normalized frequencies; therefore, we still need to obtain information about V_{p0}, ϵ, and δ for the P mode, and V_{s0}, and σ for the SV mode. Alkhalifah and Tsvankin (1994), show how to estimate Thomsen's parameters by using anisotropic P-wave NMO velocity analysis combined with shear-wave information or well logging data.

The accuracy of the explicit depth-extrapolation process in TI media is also governed by Thomsen's parameters. By first studying isotropic media, we have seen that the accuracy problem is produced mainly by a singularity in the derivative of the imaginary-part DEO. That singularity causes a relatively slow convergence of the Fourier series in the imaginary-part filter. The same behavior was observed in the DEO for TI media and for the P mode, but this time the parameters ϵ and δ determine the derivative behavior, and therefore, the accuracy of the extrapolators. This theoretical analysis was confirmed by studying the accuracy of depth-extrapolation filters calculated using the least-squares method.

For the SV mode, the minimax method was used to calculate depth-extrapolation filters for a wide range of constant values of σ, and the accuracy of the extrapolators calculated was found to be similar, with maximum propagation angles of 70 degrees, for all values of σ despite the widely differing impulse responses. The least-squares method yields a similar accuracy, but it is unable to handle triplications in the impulse response as well as does the minimax method. On the other hand, due to the poor accuracy for high propagation angles, the modified Taylor series filters could not reproduce these triplications at all.

The accuracy results obtained for the different values of Thomsen parameters, and for the P and SV propagation modes in TI media suggest that the depth extrapolation filters can propagate with accuracy up to a maximum *group angle.* For filters of length $N = 39$ coefficients, that maximum group angle is about 70 degrees. For isotropic media, the group angle is equal to the phase angle, so the maximum dip that can be propagated with accuracy will also be 70 degrees. In TI media, the anisotropy in the media changes the relation between phase angle and group angle. Depending on the anisotropy values for a given medium, different phase angles can correspond to a group angle of 70 degrees. Therefore, anisotropy will determine the maximum dip of structures in the subsurface that can be migrated with accuracy.

Results from the field data set show that because of the low estimated valued for η, and for the range of dips (0-50 degrees) present in the area, the influence of anisotropy on both the DMO process and correct location in depth of the reflectors in depth migration was appreciable, but this influence was negligible on the lateral positioning resulting from depth migration. Also, of importance was the use of an anisotropic DMO algorithm (Anderson et. al., 1994) to get not only an estimate of the anisotropic parameter η as a function of time, but also to obtain a DMO-plus-stack section that shows better definition of dipping events than that obtained assuming isotropic media. Thus, it was found essential to consider anisotropy in the DMO process in order to obtain a good mapping of the fault, while the influence of anisotropy on the lateral positioning in poststack migration was negligible. These results suggest the fundamental role that anisotropy corrections can play in prestack seismic data processing.

Here, I wish to recommend several directions along which one might expand the research and practical applications of the results obtained in this thesis. First, the explicit depth-extrapolation method can be extended to depth migration of 2D and 3D prestack data in anisotropic media. The results from the field data set show that the influence of anisotropy on the prestack process (DMO in this case) was stronger than that observed in the poststack migration. Therefore, although evidence presented here and elsewhere suggests that poststack migration via explicit operators has a limited dip range of applicability (i.e., up to about 50 degrees and the approximate 70-degree limit of accuracy for the explicit-operator approach), it is likely that *prestack* migration can benefit greatly from this approach.

The explicit method looks costly for prestack data in comparison with traditional Kirchhoff methods; however, in areas with strong lateral velocity variations, where prestack migration is often needed, the performance of explicit extrapolation must be compared against Kirchhoff methods to see which method can better handle anisotropy and velocity heterogeneities. Furthermore, the easy implementation of the process of depth-extrapolation in parallel and vector computers could make the cost of depth migration via explicit extrapolation competitive with the cost of Kirchhoff migration. In addition, it would be also useful to study the performance of explicit extrapolation in doing focussing analysis in complex areas where anisotropy may be present. As shown in the synthetic prestack results in this thesis, considering anisotropy in depth extrapolation can help to improve the imaging.

Finally, there is room to consider another kinds of anisotropy in the process of depth migration via explicit filtering. Apparently, the methods developed in this thesis can readily be applied to symmetry planes in orthorhombic media. Just by introducing the expressions for phase velocity in that kind of media, extensions of the MTS, LS and minimax methods look readily possible.

REFERENCES

Aki, K., and Richards, P. G., 1980, Quantitative seismology, theory and methods: vol. I, Freeman, San Francisco.

Alkhalifah, T., and Larner, K., 1994, Migration error in transversely isotropic media: Geophysics, **59**, 1405–1418.

Alkhalifah, T., and Tsvankin, I., 1994, Velocity analysis for transversely isotropic media: Center for Wave Phenomena Annual Report, CWP-153, Colorado School of Mines.

Alkhalifah, T., 1995a, Gaussian beam migration for anisotropic media: Geophysics, in press.

Alkhalifah, T., 1995b, Efficient synthetic seismograms for transversely isotropic media with constant velocity gradient: Geophysics, in press.

Anderson, J., and Tsvankin, I., 1994 Dip-moveout processing by Fourier transform in anisotropic media: Center for Wave Phenomena Annual Report, CWP-146, Colorado School of Mines.

Artley, C., 1994 Three-dimensional zero-offset depth migration via Gaussian beams: Center for Wave Phenomena Annual Project Review Meeting, Colorado School of Mines.

Backus, G. E., 1962, Long-wave elastic anisotropy produced by horizontal layering: J. Geophys. Res., **67**, 4427–4440.

Ball, G. J., 1993, Anisotropic 3D prestack depth migration, offshore Zaire: 63th Ann. Internat. Mtg., Soc. Expl. Geophys., Expanded Abstracts, 843–846.

Banik, N. C., 1984, Velocity anisotropy of shales and depth estimation in the North Sea basin: Geophysics, **49**, 1411–1419.

Beguelim, A., Dongarra. J. Geist, A., Weicheng, J., Mancheck, R., Sunderan, V., 1991, A user's guide to PVM (parallel virtual machine): Technical report TM-1126, ORNL (Oak Ridge National Laboratory).

Ben-Menahem, A., Gibson Jr., R.L., and Sena, A.G., 1991, Green's tensor and radiation patterns of point sources in general anisotropic inhomogeneous media: Geophys. J. Int., **107**, 297–308.

Berryman, J. G., 1979, Long-wave elastic anisotropy in transversely isotropic media: Geophysics, **44**, 896–917.

Blacquiére, G., Debeye, H. W. J., Wapenaar, C. P. A., and Berkhout, A. J., 1989, 3D table-driven migration: Geophys. Prosp., **37**, 925–958.

Cheney, E. W., 1966, Introduction to approximation theory: McGraw-Hill book company, New York

Claerbout, J. F., 1985, Imaging the Earth's interior: Blackwell Scientific Publications.

Crampin, S., Chesnokov, E. M., and Hipkin, R. A., 1984, Seismic anisotropy- the state of the art: Geophys. J. Roy. Astr. Soc., **76**, 1–16.

Daley, P. F., and Hron, F., 1977, Reflection and transmission coefficients for transversely isotropic media: Bull. Seis. Soc. Am., **67**, 661–675.

Fei, T., 1993, Seismic modeling in anisotropic media: Center for Wave Phenomena Annual Report, CWP-137, Colorado School of Mines.

Gajewski, D., 1993, Radiation from point sources in general anisotropic media: Geophys. J. Int., **113**, 299–317.

Gazdag, J., 1978, Wave equation migration with the phase shift method: Geophysics, **43**, 1342–1351.

Hale, I. D., 1991a, Stable explicit depth extrapolation of seismic wavefields: Geophysics, **56**, 1770–1777.

Hale, I. D., 1991b, 3-D depth migration via McClellan transformations: Geophysics, **56**, 1778–1785.

Holberg, O., 1988, Toward optimum one-way wave propagation: Geophys. Prosp., **36**, 99–114.

Jones, L. E. A., and Wang, H. F., 1981, Ultrasonic velocities in cretaceous shales from the Williston basin: Geophysics, **46**, 288–297.

Kitchenside, P. W., 1991, Phase shift-based migration for transverse isotropy: 61 th Ann. Internat. Mtg., Soc. Expl. Geophys., Expanded Abstracts, 993–946.

Kitchenside, P. W., 1993, 2D anisotropic migration in the space-frequency domain: Journal of seismic exploration: **2**, 7–22.

Larner, K., and Cohen, J., 1993, Migration error in transversely isotropic media with linear velocity variation in depth: Geophysics, **58**, 1454–1467.

Levin, F. K., 1979, Seismic velocities in transversely isotropic media: Geophysics, **44**, 918–936.

Loewenthal, D., Lu, L., Robertson, R., and Sherwood, J. W. C., 1976, The wave equation applied to migration: Geophys. Prosp., **24**, 380-399.

Martin, D., Ehinger, A., and Rasolofosaon, P. N. J., 1992, Some aspects of seismic modeling and imaging in anisotropic media using laser ultrasonics: 62 th Ann. Internat. Mtg., Soc. Expl. Geophys., Expanded Abstracts, 1373–1376.

McClellan, J. H., Parks, T. W., and Rabiner, L. R., 1973, A computer program for designing optimum FIR linear phase digital filters: IEEE transactions on audio and electroacoustics, **AU-21**, 506–526

Merserau, R. M., Mecklenbrauker, W. G., and Quatieri, T. F., 1976, McClellan transformations for two-dimensional digital filtering: I-Design: IEEE Trans. Circuits Syst., **CAS-23**, 405–414.

Nautiyal, A., Gray, S. H., Whitmore, N. D., and Garing, J. D., 1993, Stability versus accuracy for an explicit wavefield extrapolation operator: Geophysics, **58**, 277–283.

Oppenheim, A., and Schafer, R. W., 1989, Discrete-time signal processing: Prentice Hall signal processing series

Parks, T. W., and Mc Clellan, J. H., 1972, Chebyshev approximation for nonrecursive digital filters with linear phase: IEEE Trans. Circuit Theory, **CT-19**, 189–194

Postma, G. W., 1955, Wave propagation in a stratified medium: Geophysics, **20**, 780–806.

Sena, A. G., 1991, Seismic traveltime equations for azimuthally anisotropic and isotropic media: Estimation of interval elastic properties: Geophysiscs, **56**, 2090–2101.

Sena, A. G., and Toksöz, M. N., 1993, Kirchhoff migration and velocity analysis for converted and non-converted waves in anisotropic media: Geophysics, **58**, 265–276.

Soubaras, R., 1992, Explicit 3D migration using equiripple polynomial expansion and Laplacian synthesis: 62 th Ann. Internat. Mtg., Soc. Expl. Geophys., Expanded Abstracts, 905–908

Thomsen, L., 1986, Weak elastic anisotropy: Geophysics, **51**, 1954–1966.

Tolstov, G. P., 1976, Fourier series: Dover.

Tsvankin, I., and Chesnokov, E., 1990, Synthesis of body-wave seismograms from point sources in anisotropic media: J. Geophys. Res., **95**(B7), 11317–11331.

Tsvankin, I., 1995, Normal moveout from dipping reflectors in anisotropic media: Geophysics in press.

Tsvankin, I., 1994, P-wave signatures and parametrization of transversely isotropic media: Center for Wave Phenomena Annual Report, CWP-152, Colorado School of Mines.

Tsvankin, I., and Thomsen, L., 1994, Nonhyperbolic reflection moveout in anisotropic media: Geophysics, **59**, 1290–1304.

Uren, N., F., Gardner, G., H., F., and McDonald, J., A., 1990, The migrator's equation for anisotropic media: Geophysics, **55**, 1429–1434.

Uzcategui, O., 1994a, Accuracy of depth extrapolation in transversely isotropic media using explicit operators: Center for Wave Phenomena Annual Report, CWP-153, Colorado School of Mines

Uzcategui, O., 1994b, 2D depth migration in transversely isotropic media using explicit operators: Geophysics, submitted.

White, J. E., Martineau-Nicoletis, L., and Monash, C., 1983, Measured anisotropy in Pierre shale: Geophys. Prosp., **31**, 709–725.

Appendix A

RADIATION PATTERN IN ELLIPTICAL *P* AND *SH* WAVES

As I mentioned in Chapter 2, for elliptical anisotropy ($\epsilon = \delta$), Tsvankin (1994) found that the magnitude of the *P*-wave displacement U_P reduces to a simple function of the group angle ψ without application of the weak-anisotropy approximation:

$$U_P(R, \psi) = \frac{F_u}{4\pi\rho V_{p0}^2 R} \frac{1}{\sqrt{(1+2\delta)(1+2\delta\cos^2\psi)}}. \tag{A.1}$$

where $R \equiv \sqrt{z^2 + r^2}$ (z is the receiver depth, r is the horizontal source-receiver offset). Along a given migration impulse response, or along a given wavefront, the distance R changes with the group angle due to the anisotropy in the medium. For isotropic media, the migration impulse response and wavefront are just circles, so R is constant. In elliptical media, migration impulse response and wavefront are ellipses, so changes in R along these ellipses will cause change in amplitudes with direction. However, anisotropy (in particular, $\delta \neq 0$) also introduces the radical term in equation (A.1). As we shall now see, the combined effect of both terms for elliptical media is an amplitude that is independent of direction.

In elliptical media, the expressions for the group velocity and group angle reduce to simple functions of the phase angle. Also, the phase velocity reduces to the exact expression (Thomsen, 1986)

$$V_{ph}(\theta) = V_{p0}\sqrt{1 + 2\delta\sin^2\theta},$$

and differentiating with respect to to θ yields

$$\frac{dV_{ph}(\theta)}{d\theta} = \frac{V_{p0}^2\delta\sin 2\theta}{V_{ph}(\theta)}.$$

Substituting the above equations into the formulas for the group angle and group velocity [equations (2.19) and (2.20)], we obtain

$$\tan\psi(\theta) = (1 + 2\delta)\tan\theta \tag{A.2}$$

$$V_g[\psi(\theta)] = V_{p0}\sqrt{\frac{1 + 4\delta\sin^2\theta + 4\delta^2\sin^2\theta}{1 + 2\delta\sin^2\theta}}. \tag{A.3}$$

Using equation (2.21) for the migration impulse response, we can write R in equation

(A.1) as

$$R \equiv \sqrt{x^2+z^2} = \frac{t_0}{2}V_g(\psi),$$

where t_0 is the observed two-way time in the zero-offset section. With equation (A.3), R can be finally expressed as

$$R = \frac{t_0}{2}V_{p0}\sqrt{\frac{1+4\delta\sin^2\theta+4\delta^2\sin^2\theta}{1+2\delta\sin^2\theta}}. \tag{A.4}$$

From the expression for the group angle [equation (A.2)] we obtain

$$\cos^2\psi(\theta) = \frac{1}{1+(1+2\delta)^2\tan^2\theta} = \frac{\cos^2\theta}{\cos^2\theta+(1+2\delta)^2\sin^2\theta},$$

so the radical term in equation (A.1) can be expressed as

$$\sqrt{(1+2\delta)(1+2\delta\cos^2\psi)} = (1+2\delta)\sqrt{\frac{1+2\delta\sin^2\theta}{1+4\delta\sin^2\theta+4\delta^2\sin^2\theta}}. \tag{A.5}$$

Equations (A.4) and (A.5) then give us

$$\begin{aligned} R\sqrt{(1+2\delta)(1+2\delta\cos^2\psi)} &= \frac{V_{p0}t_0}{2}\sqrt{\frac{1+4\delta\sin^2\theta+4\delta^2\sin^2\theta}{1+2\delta\sin^2\theta}} \\ &\quad (1+2\delta)\sqrt{\frac{1+2\delta\sin\theta^2}{1+4\delta\sin^2\theta+4\delta^2\sin^2\theta}} \\ &= \frac{V_{p0}t_0}{2}(1+2\delta). \end{aligned}$$

Finally, the radiation pattern for the elliptical P-wave can be written simply as a function of the zero-offset time t_0 as

$$U_P(t_0) = \frac{F_u}{4\pi\rho V_{p0}^3}\frac{2}{t_0(1+2\delta)}. \tag{A.6}$$

Following an identical reasoning, we can obtain the radiation pattern for the SH-wave as

$$U_{SH}(t_0) = \frac{F_2}{4\pi\rho V_{s0}^3}\frac{2}{t_0(1+2\gamma)}. \tag{A.7}$$

Equation (A.7) is completely independent of the phase angle θ because the force term F_2 is constant (see Chapter 2), so equation (A.7) tells us that even when the shape of the migration impulse response and wavefront are elliptical, the amplitude along these curves for the SH mode in TI media is constant. On the other hand, for the P-wave mode, equation (A.6) shows that the amplitude depends on θ just through the force term F_u. This result was used in Chapter 2 to calculate the theoretical amplitude in Figure 2.13.

Appendix B

PARKS-MCCLELLAN ALGORITHM TO CALCULATE MINIMAX FILTERS

As discussed in Chapter 3, the design of a finite length filter in the minimax method requires the specification of the parameters N, k_{max}, k_s, and the ratio $L = \delta_2/\delta_1$. The Parks-McClellan (1972) algorithm is based on reformating the filter design problem as a problem in polynomial approximation. The terms $\cos lk$ in equation (3.3) can be expressed as a sum of powers of $\cos k$ in the form

$$\cos lk = T_l(\cos k), \tag{B.1}$$

where $T_l(x)$ is the l^{th}-order Chebyshev polynomial, defined as $T_l(x) = \cos(l \cos^{-1} x)$. Using equation (B.1), we can write the frequency response of the filter in equation (3.3) as a $N_l = (N-1)/2$th-order polynomial in $\cos k$

$$W(k,\omega) = \sum_{l=0}^{N_l} h_l(\omega)(\cos k)^l. \tag{B.2}$$

As shown in Chapter 3, the minimization criterion in the filter design problem is the minimax criterion, in which within the wavenumber bands we seek a frequency response for the filter that minimizes the maximum weighted approximation error [see equation(3.14)]. Parks and McClellan (1972) applied the alternation theorem to this filter design problem

Alternation theorem. Let F_p denotes the closed subset consisting of the disjoint union of closed subsets of the real axis x. P_r denotes an r^{th}-order polynomial, and $D_p(x)$ denotes a given desired function of x that is continuous on F_p; $WEI_p(x)$ is a positive weighting function, continuous on F_p, and $E_p(x)$ denotes the weighted error

$$E_p(x) = WEI_p(x)|D_p(x) - P_r(x)|.$$

The maximum error $\| M \|$ is defined as

$$\| M \| = max_{x \in F_p} |E_p(x)|.$$

A necessary and sufficient condition that P_r is the unique r^{th}-order polynomial that minimizes $\| M \|$ is that $E_p(x)$ exhibit at least $(r+2)$ alternations, i.e., there must exist at least $(r+2)$ values x_i in F_p such that $x_1 < x_2 < \ldots x_{r+2}$ and such that

$$E_p(x_i) = -E_p(x_{i+1}) = \pm \parallel M \parallel \quad for\ i = 1, 2, \ldots (r+1).$$

The demonstration of this theorem is given in Chenney (1966). The alternation theorem states that the optimum filter must have a minimum of $(r+2)$ alternations, but does not exclude the possibility of more than $(r+2)$ alternations. However, Oppenheim and Schafer (1989) show that for a filter of length N_l:

- the maximum possible number of alternations is $N_l + 3$
- alternations will always ocurr at k_{max} and k_s (maximum wavenumber in the propagation region and first wavenumber in the evanescent region, respectively)
- all points of zero slope inside the passband and stopband will correspond to alternations

Returning to our depth-extrapolation filter problem, from the alternation theorem we know that the optimum filter $W(k, \omega)$ will satisfy equation (3.14),

$$E_p(k) = E(k)[D(k,\omega) - W(k,\omega)] = (-1)^{i+1}\delta_1\ for\ i = 1, 2, \ldots N_l + 2, \tag{B.3}$$

where δ_1 is the optimum error. The above set of equations can be solved for the set of coefficients $h_l(\omega)$ and for the optimum error δ_1. However, a more efficient alternative is to use polynomial interpolation. The procedure begins by guessing a set of alternation frequencies k_i, $i = 1, 2, \ldots N_{l+2}$. Parks and McClellan (1972) found that for the given set of extremal frequencies, δ_1 is given by

$$\delta_1 = \frac{\sum_{k=1}^{N_l+2} b_k D(k_x)}{\sum_{k=1}^{N_l+2} b_k (-1)^{k+1} / E_p(k)} \tag{B.4}$$

with

$$b_k = \prod_{i \neq k}^{N_l+2} \frac{1}{(x_k - x_i)}$$

where $x_i = \cos k_i$. That is, if $W(k,\omega)$ is determined by the set of coefficients $h_l(\omega)$ that satisfy equation (B.3), with δ_1 given by equation (B.4), then the error function goes through $\pm\delta_1$ at the $(L+2)$ frequencies k_i. Since $W(k,\omega)$ is known to be an N_lth-order trigonometric polynomial, we can interpolate a trigonometric polynomial through $(L+1)$ of the $(L+2)$ known values $W(k_i,\omega)$. Now, $W(k,\omega)$ is available at any desired wavenumber without the need to solve the set of equations (B.3). Parks and McClellan used Lagrange interpolation to evaluate $W(k,\omega)$ and $E_p(k)$ on a dense set of frequencies in the passband and stopband. If $|E_p(k)| \leq \delta_1$ for all wavenumbers in the bandpass and stopband, then the optimum approximation has been found. Otherwise we must find a new set of extremal frequencies. Adopting the philosophy of the Remez method

(McClellan et al., 1972), the extremal frequencies are exchanged for a completely new set defined by the (N_l+2) largest peaks of the error curve. The complete cycle (computation of δ_1, fitting a polynomial to the assumed error peaks, and then locating the actual error peaks) is repeated until δ_1 does not change from its previous value by more than a prescribed small amount. This value of δ_1 is then the desired minimum maximum weighted approximation error.

In the calculation of depth-extrapolation filters for isotropic media, Soubaras (1992) found that the number of iterations needed to calculate the filters was about 12. I found a similar number of iterations for the filter calculation in TI media.

Appendix C

FILTERS FOR NON-VERTICAL AXIS OF SYMMETRY

In Chapter 3, I pointed out that the computer time to calculate explicit filters for TI media with a non-vertical axis of symmetry is more than twice the time needed to calculate the filters for TI media with a vertical axis of symmetry. I show in this appendix how to avoid this expensive calculation. I obtain the non-symmetrical filters needed for a TI media with a tilted axis of symmetry, by calculating just two symmetrical filters.

Figure C.1 shows two theoretical migration impulse responses calculated for a TI media with a tilted axis of +20 (black curve) and -20 (gray curve) degrees with respect to the vertical ($\epsilon = 0.1$ and $\delta = -0.1$ in both curves). For negative midpoints, the gray curve has exactly the same shape that has the black curve for positive midpoints and vice versa. If we calculate symmetrical depth-extrapolation filters for the same TI media as in Figure C.1 using spatial wavenumbers given by

$$k_x = \frac{\omega \sin\theta}{V_{ph}(\theta - \psi)}, \tag{C.1}$$

where $\psi = 20$ degrees is the tilt of the symmetry axis, the migration impulse response of these filters will reproduce the gray curve for negative midpoints and the black curve for positive midpoints. On the other hand, filters calculated using spatial wavenumbers given by

$$k_x = \frac{\omega \sin\theta}{V_{ph}(\theta + \psi)}, \tag{C.2}$$

will reproduce the black curve for negative midpoints and the gray curve for positive midpoints. Neither of the filters calculated in equations (C.1) or (C.2) give us one of the theoretical migration impulse responses of Figure C.1. So the idea is to combine the symmetrical filters of equations (C.1) and (C.2) to obtain a non-symmetrical filter that reproduces one of the impulse responses in Figure C.1. Let us suppose that we want to calculate filters for a tilted axis of 20 degrees. If we denote by $p(k_x)$ and $n(k_x)$ the frequency responses of the filters calculated in (C.1) and (C.2), respectively, the frequency response $t(k_x)$ of the desired non-symmetrical filter will be given by

$$t(k_x) = S(k_x)p(k_x) + S(-k_x)n(k_x), \tag{C.3}$$

where $S(k_x)$ represents the step function defined as

$$S(k_x) = \begin{cases} 1, & \text{if } k_x \geq 0.0, \\ 0, & \text{if } k_x < 0.0. \end{cases}$$

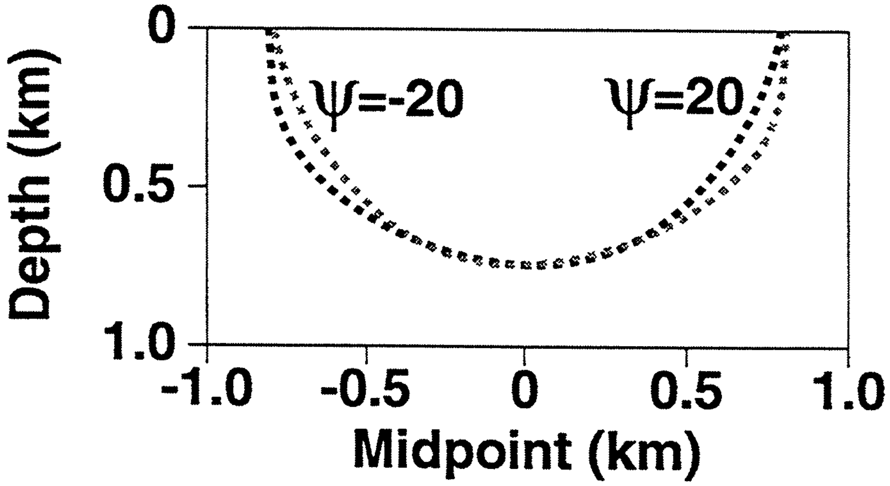

FIG. C.1. Theoretical depth-migration impulse responses for tilted axis of symmetry of 20 and -20 degrees. In both curves, ϵ=0.1, and δ=-0.1.

and $p(k_x)$ is given by

$$p(k_x) = \sum_{n=0}^{(N-1)/2} p_n \cos k_x n,$$

where p_n are the symmetrical filter coefficients for p, and N is the total number of filter coefficients. Similar expressions hold for the frequencies responses $t(k_x)$ and $n(k_x)$. The depth extrapolation process is applied in the (ω, x) domain, so we need to take the inverse spatial Fourier transform of equation (C.3) to obtain

$$t_n = p_n * \tilde{S}(k_x) + n_n * \tilde{S}(-k_x), \tag{C.4}$$

where * denotes convolution in the x domain and the tilde represents the inverse spatial Fourier transform. The step function has Fourier transform given by

$$S(k_x) \Longleftrightarrow \frac{1}{2}(\delta(x) - \frac{1}{\pi i x})$$
$$S(-k_x) \Longleftrightarrow \frac{1}{2}(\delta(x) + \frac{1}{\pi i x}),$$

where $\delta(k_x)$ is the Dirac delta function. Therefore, equation (C.4) is given by

$$t_n = \frac{1}{2}[p_n + n_n] + \frac{1}{2}(\frac{-1}{\pi i x}) * [p_n - n_n].$$

The operator $-1/(\pi i x)$ is the Hilbert transform operator, so the last equation can be rewritten as

$$\begin{aligned} t_n &= \frac{1}{2}(p_n + n_n) + \frac{1}{2}H * (p_n - n_n) \quad n = 0, \dots, N/2 \\ t_n &= \frac{1}{2}(p_n + n_n) + \frac{1}{2}H * (n_n - p_n) \quad n = -N/2, \dots, -1 \end{aligned} \tag{C.5}$$

where H denotes a discrete Hilbert transform operator.